nature portfolio

Peer Review File

Measurement of a strong nonlinear force between superconductors compatible with the Casimir force

Corresponding Author: Dr Laure Mercier de Lépinay

This file contains all reviewer reports in order by version, followed by all author rebuttals in order by version.

Version 0:

Reviewer comments:

Reviewer #1

(Remarks to the Author)
The manuscript by Jong et al reports on measurements of nonlinear behavior of a drum resonator, which can be attributed to the influence of the Casimir force acting between two superconducting plates. The authors use a superconducting capacitive plate oscillator, of which the top plate is mechanically compliant, ie, forming a drum. This capacitor is part of a microwave LC resonator, thus, forming a microwave optomechanical circuit. Such circuits have been widely used to, eg, demonstrate ground state cooling of mechanical motion, strong optomechanical coupling, microwave to optics conversion, or even entanglement between two such drums. The key novelty in the present work is the small gap of the drum oscillator of about 18nm, which has not been achieved so far. Conventionally, the top plate would be harmonically bound through its connection to its support. However, due to the tiny gap, the attractive Casimir potential cannot be neglected and alters the potential of the drum oscillator such that it becomes non-harmonic and shows a spring softening behavior for large amplitudes. This is what the authors show experimentally. All data is described very accurately by the assumed Casimir force magnitude and distance-scaling and the standard optomechanical equations of motion.

The work presents the first experiment observing the influence of the Casimir force between two superconducting plates inferred from its nonlinear position dependence, which renders the potential of a mechanical oscillator slightly nonlinear. The work makes use of the well-developed and high-precision technology of cavity electromechanics, which is advanced by realizing sub-20nm gaps of the utilized drum resonator. This is an impressive technical achievement. Only for this small distance, the Casimir force between superconductors is of relevance, which the authors impressively show.

In general, I am very positive towards publication of the manuscript as it constitutes a clear experimental demonstration of the Casimir force between superconducting plates. The work supports its findings by a well developed theory, which fits the experimental data very well.

However, I would like that the authors address the following points before I would recommend publication of this nice work. In part my comments are aimed to support the claims even more and in part would lead to a clarification of some statements of the present manuscript.

1) I think it would be desirable to run the same measurements using a drum oscillator, whose spacing is much larger, eg, more than 50nm, where the Casimir effect would be of no concern. Such a measurement would support even more the findings of the present work that the Casimir force is causing the observed nonlinear behavior. In such a larger gap drum oscillator, the Casimir force should not result in nonlinear behavior, and, a set of similar measurements should, thus, deliver a null result. I would not insist on adding such measurements to the present manuscript as I am aware of the fact that it may necessitate a new fab run, which is costly in time. However, I would encourage the authors to think about this point and to potentially do such measurements.

2) Along the lines of the previous comment, it would also be supporting, if the authors could check another device with a slightly different drum gap and reproduce their results. I would also not insist on implementing this comment for the present manuscript. However, I would strongly encourage the authors to make such measurements, possible in the future.

3) To increase the amplitude of the mechanical oscillator, a drive close to resonance and another drive on the lower sideband are used.

First, I guess that the resonant drive is slightly red-detuned w.r.t. the cavity resonance to avoid a potential cavity instability. Is this correct? If so, what is the effect of the slight cooling this drive does on the mechanical oscillator? I ask as it is of utmost importance to infer an accurate value for the amplitude of the mechanical oscillator, which is required to make proper estimates of the Casimir force.

Secondly, the two drives interfere to result in an amplitude modulated drive centered close to cavity resonance, which as a result leads to driving of the mechanical amplitude. Could the authors give an intuitive picture of this driving scheme such that the reader can easily grasp why they have chosen to drive the mechanics like that? For example, the authors could also have chosen to center the sideband drive on the blue side of the cavity, which should give similar results.

4) The optomechanical coupling strength is inferred to be 2\pi 150Hz. I wonder how close this value is to the expected value. The latter could be obtained from the gap d, the simulated effective mass, the measured resonance frequency and the knowledge of the capacitances in the circuit. Is the value of g0/2\pi=150Hz close to such an expectation?

5) The SI material shows figure S1, which depicts a deviating behavior in power for higher drive powers. This is attributed to the Casimir force, which at high drive powers influences also the intra-cavity photon number. However, such a behavior could also originate from a weak Kerr-like photon nonlinearity of the microwave cavity itself, which would result in lowering the intra-cavity photon number at higher drive powers due to shifting the cavity resonance frequency. Could the authors argue if such an effect occurs in their device?

6) It is assumed that the Al thin film is of type I. However, I would guess that the film contains small Al grains such that it may be possible that flux lines could penetrate it (at grain boundaries). A recent study showed that the London penetration depth of Al thin films can be as large as the film thickness itself (e.g., arXiv:2311.14119). How would flux penetration (or non-ideal type I behavior) influence the inference of the Casimir force, ie, the exponent of the force-distance relation and the Casimir pressure?

7) Along the lines of point 6), if the film can trap flux, this could result in an additional force acting on the mechanical oscillator. As the magnetic field of a flux line is highly non-uniform, it may also lead to a nonlinear force-distance relation. Could the authors estimate the effect of trapped flux on the motion of the mechanical oscillator, ie, on its potential?

8) The abstract introduces that the Casimir force between superconducting plates is still not fully understood, quoting from the abstract: "...There is significant interest in this contribution as it is suspected to contribute to an unexplained discrepancy between predictions and measurements of the Casimir force". However, the authors use the results of Ref 28 to calculate their expected Casimir force, which seems to contradict the statement from the abstract. Using Ref 28, it seems that the Casimir force can be calculated for the specific situation the authors analyze. Hence, I would suggest to reformulate the statement in the abstract as I find it misleading, or this statement needs to be addressed in the main manuscript by comparing to the said discrepancies between (previous) experiments and theory.

9) Further, the statement "... By contrast, the strong nonlinearity imparted by the Casimir potential can be easily shown without relying on the force-distance scaling." seems to be misleading. The present work makes full use of the nonlinear force-distance relation. Only this nonlinear relation leads to the nonlinear behavior of the mechanical drum oscillator. Hence, I would encourage the authors to rewrite this part. I am aware of the fact that the present work does not statically tune the position of the drum plate. However, the present experiment still makes full use of the nonlinear Casimir force-distance relation, which influences the dynamic behavior of the drum oscillation amplitude.

10) I do not understand the statement of an "imperfect material". What do the authors mean with that statement in relation to using BCS theory to estimate the Casimir force, ie, what does the said "imperfection" refer to?

11) How is the maximal mechanical displacement of 100pm determined?

12) A question motivated by curiosity: could the Casimir force potentially lead to additional mechanical damping/decoherence or even nonlinear damping?

13) The authors simulate the resonance frequency of the drum at room temperature, which is expected to be 5.4MHz. Have the authors measured this frequency at room temperature, eg, using optical interferometry to verify their simulation result?

14) I am a little confused by a statement in the Methods section on "Drum frequency and effective mass". It is said that the small tensile stress leads to sacking of the top plate. Normally, I would expect that compressive stress only leads to sacking, while tensile stress leads to straightening/stiffening. How can I understand this statement?

15) The authors refer to their previous work Ref 62 in SI, where they introduce a formalism of estimating patch potentials. It would be good to give a summary of this work even in the main part of the work, eg, in the Methods section. Patch potentials are of major concern in the experiments the authors perform. Hence, a more elaborate discussion in the main part of their work would be beneficial to convince the reader that the influence of patch potentials can be neglected.

16) The Casimir exponent is obtained from Ref 28. However, would it be possible to obtain it directly from the measurements, ie, via fitting the data?

A few minor comments:

A) Fig S15 is the same as Fig S14, which is probably a mistake.

B) Methods section: Eqn. 12 contains the symbol \omega, should it be \omega_d?

C) The citation for the statement "Notably, resonators were cooled close
to the ground state..." should be J D Teufel et al, Nature 475, 359 (2011) "Sideband cooling of micromechanical motion to the
quantum ground state", instead of Ref. 32, I would suggest.

Reviewer #2

(Remarks to the Author)
In this work, the authors use a superconducting electromechanical circuit to measure the nonlinearity of a mechanical resonator. Through a series of careful measurements and calibrations, the authors demonstrate that this measured nonlinearity is quantitatively consistent with what is expected from the Casimir effect. The Casimir effect is a purely quantum effect in which vacuum fluctuations of the electromagnetic field impart a measurable force on surfaces which are sufficiently close together. By ruling out other potential sources of mechanical nonlinearity, they conclude that their data should be interpreted as the first measurement of the Casimir force between two superconducting electrodes.

I find this work to be thorough, novel and important. The hallmark of the Casimir effect is the strong power law dependence of the force with distance. Instead of measuring how a microelectromechanical system responds to static changes in the plate separation, they observe the how the system responds to large amplitude AC displacements. Specifically, the observed softening nonlinearity of the mechanical response function appears to show excellent agreement with theoretical predictions of the expected Casimir behavior.

However, before fully recommending publication I have several important questions that I would like the authors to address.

1. The abstract and introduction state multiple times that this effect is measured “for the first time.” I find this claim of priority unnecessary and slightly contentious. As the authors reference in their manuscript, other electromechanical circuits have shown behavior that is only consistent with Casimir behavior (reference 29 in the main text). While this prior work did not exhaustively rule out other possible explanations for the data, it also showed excellent quantitative agreement with Casimir theory. In my opinion, this current manuscript is sufficiently interesting and important to be published without making the claim to be first.

2. As the heart of this work is a quantitative measurement of the Casimir nonlinearity, the manuscript should be perfectly clear what the variables “d” and “x” refer to. Is this the displacement at the center of the of the capacitor, or the average plate separation over the capacitor area, or effective displacement averaged over the entire mechanical mode shape? Likewise for the AC displacements are the calibrated and measured displacement powers (in nm^2) the peak-to-peak or the mean-square amplitude?

3. All four figures of the paper show essentially the same type of data…mechanical response functions as a function of drive powers. It is not clear if the data in fig 1c is different from what is shown in fig 2 or just a subset? If so, why is it being shown twice?

4. While it is impressive that the entire data sets in fig’s 1,2,3,4 can be well fit by a single fit parameter for the nonlinearity, that is what one would expect for any single nonlinearity. This clearly demonstrates that the all the data is self-consistent and that the authors faithfully understand how microwave drive powers scale with mechanical displacement over many orders of magnitude. The most crucial part of this entire paper is the calibration to real amplitude units. My understanding is this absolute calibration of the motion in meters comes fundamentally from measuring the thermal motion at a known temperature, and using the equipartition theorem as a primary displacement calibration. Is this correct? If so, the authors should state this more clearly. It is my understanding that without this thermal calibration, there would be an ambiguity in the absolute amplitude of the motion due to the unknown attention of the microwave cables and unknown gain of the microwave amplifiers. It is only with this absolute calibration that these measurements can quantitatively compare with Casimir. Also, if this is the case, does that mean that the uncertainty on g_0 should be the dominant uncertainty in the absolute plate separation determination?

5. As with all weak nonlinearities, to lowest order the Casimir nonlinearity can be cast as a Duffing correction or a Kerr coefficient in which the mechanical frequency shifts as the amplitude of motion is increased. It would be useful for the reader to quantify what this Duffing or Kerr coefficient is for the current device, in both nanometers or phonon number. This would help elucidate how close (or far) the current device is from a full qubit regime in which a single phonon shifts the mechanical resonance frequency by more than a mechanical linewidth.

6. There is very little detail on the microwave resonant circuit. What is the inductance and parasitic capacitance of the resonator? Is there a picture of the geometry or a reference to previous work that uses a similar geometry. Specifically, it is surprising that the extremely close final plate separation shown here (~15 nm) does not have a bigger g_0. Is this because there is a large amount of extraneous capacitance in the circuit? It is important to show that the measured g_0 also self-

consistently agrees with the inferred cold plate separation.

Minor comments and suggestions:

A. Figure 1c. There is a discontinuity in the data at a detuning of 2 kHz. I assume the authors did this to help clearly show that they have good fits over a large range in frequency and power. I had to look at the figure many times to understand that the kink in the data was an artifact of how it was being plotted. I would recommend either plotting all of the data and using insets or zoom-ins to show that all features. Or alternatively, at least showing a clear gap in the data and axes so the reader immediately sees that the plot is over a discontinuous frequency range.

B. On page 2, In the paragraph after equation (1), the text states:
"…where n = −3.193 ± 0.005 is fitted from BCS theory." I believe that n should be a positive number that way it is defined here.

C. On page 8 of the main text, the manuscript says: "When we compute the thermal expansion down to 10mK…" I believe this should read "When we compute the thermal contraction down to 10mk…"

D. The authors determine from their COMSOL modeling that mechanical frequency at room temperature should be approximately 5.4 MHz. Have the authors tried to measure the room temperature mechanical frequency? Obviously, not using the superconducting resonator, but a room temperature vibrometer measurement of the resonance frequency could give additional confidence to the model.

E. The authors measure only the magnitude of the mechanical response function throughout the text. It seems like they should also be able to measure the full vector response function, including phase of the mechanical resonance. Specifically, using a vector network analyzer and a room-temperature mixer (instead of a spectrum analyzer) would give access to this information. While I don't think there would be anything surprising in the phase information, if the authors have measured it, showing it would help demonstrate full understanding of the mechanical mode and the Casimir nonlinearity.

Reviewer #3

(Remarks to the Author)
see attachment

Reviewer #4

(Remarks to the Author)
I co-reviewed this manuscript with one of the reviewers who provided the listed reports. This is part of the Nature Communications initiative to facilitate training in peer review and to provide appropriate recognition for Early Career Researchers who co-review manuscripts.

Version 1:

Reviewer comments:

Reviewer #1

(Remarks to the Author)
The authors have in detail addressed all the points I raised with great care and adapted their manuscript accordingly. I also very much appreciate that the authors included new data for a second device with a similar gap size that corroborates the findings of the work.

There is one important point, however, which I realized after having read the revised version of the manuscript. I kindly ask the authors to address this point as it regards the validity of their model for the optomechanical equations of motion.

Equation (1) of the main text describes the dynamics of the mechanical system including the Casimir nonlinear force. Equations (2) of the main text describe the coupled optomechanical equations of motion, which include the coupling of the mechanical resonator to the optical intracavity field. However, the mechanical evolution in Equation (2) is harmonic and the nonlinear Casimir force term is neglected. This modelling is inconsistent with the assumption of Eqn. (1) and also with the measurements the authors perform as they drive the mechanical resonator to a regime, where clear nonlinear effects of the mechanics are observed (e.g., Fig 1c,d). Even if the authors use the 'perturbed' mechanical frequency \omega_m in these equations, the underlying dynamics of the mechanics must be assumed to be nonlinear, in particular, when driven strongly, as the authors do. Hence, currently there appears to be an inconsistency in the theoretical modelling of the system, which should be alleviated before the manuscript can be recommended for publication.

Further, as a minor remark, I would encourage the authors to clarify the use of the term 'optomechanical' nonlinearity, which is ambiguous as there are different types of 'optomechanical' nonlinearities acting: (i) the intrinsic non-linearized optomechanical Hamiltonian is nonlinear (ie, radiation-pressure interaction), (ii) the coupling strength is assumed to be linear in displacement, but higher order expansions are nonlinear in displacement (see Eq. S24), (iii) the cavity frequency spectral response is nonlinear (see, e.g., https://doi.org/10.1103/PhysRevLett.131.053601). Could the authors explain more clearly to which effect(s) they refer to?

I have read through the criticism of reviewers 2 and 3 and the author's reply to that criticism. In case of Reviewer 2, the authors have addressed all the comments in a sufficient manner - to the best of my knowledge. Also, Reviewer 2 was in general very positive to the work.

The authors have also replied to the comments of Reviewer 3. In that case, I would, however, like to recommend that the authors make an additional change to their manuscript concerning the point of the discussion on "van der Waals and Casimir forces are generally defined as limit cases of the dispersion force". Though this point is discussed in the reply to the reviewer, the discussion is missing in the revised manuscript. However, I believe that this discussion would be necessary to show to the reader. Finally, Reviewer 3 asks the authors to soften their claim from "unambiguous observation of Casimir forces" into "power law attractive forces consistent with Casimir". This request has not been adhered to. Instead, the authors argue that they took all possible other effects into consideration and concluded that the experimental data is only consistent with the Casimir force. This being said could, of course, not rule out an yet unknown other effect.

Version 2:

Reviewer comments:

Reviewer #1

(Remarks to the Author)
The authors did give great care to address the final points that I raised in a convincing manner. Thus, I recommend publication of this revised manuscript including all additional material in Nature Communications.

Dear editor,

We would like to thank the referees for their extensive and detailed comments, and you for handling our manuscript. We have copied the reviewer's reports below (in black) and added our response (in blue). We have made many textual changes in the document to make our claims more precise and address the questions by the referees. We have furthermore added additional information, calculations, and simulations to the supplementary.

On behalf of the authors,
Laure Mercier de Lépinay

Reviewer 1

The manuscript by Jong et al reports on measurements of nonlinear behavior of a drum resonator, which can be attributed to the influence of the Casimir force acting between two superconducting plates. The authors use a superconducting capacitive plate oscillator, of which the top plate is mechanically compliant, ie, forming a drum. This capacitor is part of a microwave LC resonator, thus, forming a microwave optomechanical circuit. Such circuits have been widely used to, eg, demonstrate ground state cooling of mechanical motion, strong optomechanical coupling, microwave to optics conversion, or even entanglement between two such drums. The key novelty in the present work is the small gap of the drum oscillator of about 18nm, which has not been achieved so far. Conventionally, the top plate would be harmonically bound through its connection to its support. However, due to the tiny gap, the attractive Casimir potential cannot be neglected and alters the potential of the drum oscillator such that it becomes non-harmonic and shows a spring softening behavior for large amplitudes. This is what the authors show experimentally. All data is described very accurately by the assumed Casimir force magnitude and distance-scaling and the standard optomechanical equations of motion.

The work presents the first experiment observing the influence of the Casimir force between two superconducting plates inferred from its nonlinear position dependence, which renders the potential of a mechanical oscillator slightly nonlinear. The work makes use of the well-developed and high-precision technology of cavity electromechanics, which is advanced by realizing sub-20nm gaps of the utilized drum resonator. This is an impressive technical achievement. Only for this small distance, the Casimir force between superconductors is of relevance, which the authors impressively show.

In general, I am very positive towards publication of the manuscript as it constitutes a clear experimental demonstration of the Casimir force between superconducting plates. The work supports its findings by a well developed theory, which fits the experimental data very well.

However, I would like that the authors address the following points before I would recommend publication of this nice work. In part my comments are aimed to support the claims even more and in part would lead to a clarification of some statements of the present manuscript.

We thank the reviewer for their positive comments about our work.

1) I think it would be desirable to run the same measurements using a drum oscillator,

whose spacing is much larger, eg, more than 50nm, where the Casimir effect would be of no concern. Such a measurement would support even more the findings of the present work that the Casimir force is causing the observed nonlinear behavior. In such a larger gap drum oscillator, the Casimir force should not result in nonlinear behavior, and, a set of similar measurements should, thus, deliver a null result. I would not insist on adding such measurements to the present manuscript as I am aware of the fact that it may necessitate a new fab run, which is costly in time. However, I would encourage the authors to think about this point and to potentially do such measurements.

We agree with the referee that these are desirable comparisons. In fact, in several earlier works, we have used either blue-sideband drive or strong two-tone drives to bring drums with larger gaps into a high amplitude oscillation regime or even into the self-oscillation regime, and have not specifically observed a nonlinearity compatible with a Casimir potential. For example, in D. Cattiaux et al., Phys. Rev. Research **2**, 033480 (2020), another device with an even larger gap (smaller coupling, $g_0 = 2\pi \times 10$ Hz) was driven into self-oscillation until it reaches the geometric *hardening* nonlinearity.

Since these previous experiments did not show a softening nonlinearity, they can be considered as 'null results' for the Casimir nonlinearity at higher drum gap. As the referee points out, now that we know how to fabricate drums with very small gap as well as larger gaps, we would ideally like to replicate the exact protocols used in this paper on drums with larger gaps for comparison, which is indeed very costly in time.

2) Along the lines of the previous comment, it would also be supporting, if the authors could check another device with a slightly different drum gap and reproduce their results. I would also not insist on implementing this comment for the present manuscript. However, I would strongly encourage the authors to make such measurements, possible in the future.

We have reproduced our results on a second device with a slightly larger gap, as shown in the newly added Supplementary Section F. This device was made in a new fabrication run using the same design and process as the device reported in the main text, but it was characterized, calibrated, and measured in a different dilution refrigerator (due to setup availability). We have fitted a gap of 19.1 ± 0.5 nm to the experimental results using the same procedure as for the device in the main text. The similarity of the gap is due to the same design being used. The observation of the softening nonlinearity in a second device increases our confidence in the results of this work.

3) To increase the amplitude of the mechanical oscillator, a drive close to resonance and another drive on the lower sideband are used.

First, I guess that the resonant drive is slightly red-detuned w.r.t. the cavity resonance to avoid a potential cavity instability. Is this correct? If so, what is the effect of the slight cooling this drive does on the mechanical oscillator? I ask as it is of utmost importance to infer an accurate value for the amplitude of the mechanical oscillator, which is required to make proper estimates of the Casimir force.

The device is well in the sideband-resolved regime: $\omega_m \simeq 18.25\kappa$. That is, even the maximum estimated detuning of the drive would not result in an instability, since dynamical backaction is vanishingly small in this regime. Therefore, since this is not leading to instability, the resonant drive is centered at the cavity frequency, to the best accuracy that we could reach during the experiment. The parameters reported in Table 1 include an estimation of a the maximal possible accidental detuning of this tone Δ (max 1 kHz for a cavity with linewidth ~ 600 kHz).

We have revised the text describing our amplitude calibration procedure, for clarity.

Secondly, the two drives interfere to result in an amplitude modulated drive centered close to cavity resonance, which as a result leads to driving of the mechanical amplitude. Could the authors give an intuitive picture of this driving scheme such that the reader can easily grasp why they have chosen to drive the mechanics like that? For example, the authors could also have chosen to center the sideband drive on the blue side of the cavity, which should give similar results.

An intuitive picture of our drive method would be the following: Because of the nonlinearity of the optomechanical interaction, the two drives interfere such that there is a beat note at the mechanical frequency, $\omega_{\mathrm{mw}} - \omega_{\mathrm{sb}} = \omega_{\mathrm{m}}$. This amplitude modulation of the drive leads to a force modulated at mechanical resonance frequency ω_{m}.

The dynamical backaction from a single blue-detuned drive results in a power-dependent linewidth, and therefore a power-dependent response of the oscillator. Furthermore, any small inaccuracy in the drive power would have led to a dramatic inaccuracy in the mechanical displacement. In comparison, the two-tone actuation that we used allowed to sweep the power of the drive at the cavity frequency, and therefore of the forcing amplitude, over multiple decades without affecting the mechanical linewidth and without reaching the self-oscillation regime (although we also realized red-sideband-drive power sweeps for completeness, over which the dynamical backaction did vary). As the referee states correctly, a nearly-equivalent drive scheme can be obtained by combination of an on-resonant cavity drive with a blue-sideband drive. However, this scheme might reach the self-oscillation regime for some combinations of blue-sideband drive and on-resonant cavity drive.

4) The optomechanical coupling strength is inferred to be 2π 150Hz. I wonder how close this value is to the expected value. The latter could be obtained from the gap d, the simulated effective mass, the measured resonance frequency and the knowledge of the capacitances in the circuit. Is the value of g0/2π=150Hz close to such an expectation?

This comparison of g_0 is a good suggestion in theory. However, we observe that the simulations of the circuit with common finite element simulation tools do not predict the final characteristics of cavities in samples. There is a spread in parameters between devices with identical design and from the same fabrication run, which suggests that some microscopic or fabrication-related details are not captured by our circuit simulations.

We suspect that (1) box resonances are not well represented and have a significant impact and (2) the impedance of bond wires is not well controlled, they actually have a non-negligible inductance and their length and shape depend on details such as the geometry of the sample chip holder.
The single-photon optomechanical coupling is defined as the shift of the cavity frequency under a displacement equivalent to the magnitude of zero-point fluctuations x_{zpf} of the mechanical oscillator: $g_0 = \frac{\partial \omega_c}{\partial x} x_{\mathrm{zpf}}$ where x_{zpf}. In the revised version of our paper, we have added a supplementary section describing our circuit model and find that it predicts a coupling rate $g_0 \simeq 2\pi \times 480$ Hz. The fact that the electromagnetic environment of the drum is difficult to simulate means that the estimate of $\frac{\partial \omega_c}{\partial x}$ from simulations is unreliable. This is why we consider that this estimate of g_0 does not yield accurate results.

5) The SI material shows figure S1, which depicts a deviating behavior in power for higher drive powers. This is attributed to the Casimir force, which at high drive powers influences also the intra-cavity photon number.

We made a mistake in the text in assigning the power deviation in Fig. S1 to the Casimir nonlinearity, as we in fact assign it to the optomechanical nonlinearity which we model numerically in the SI and describe in Fig. 3**c** of the main text. This is corrected in the revised version.

However, such a behavior could also originate from a weak Kerr-like photon nonlinearity of the microwave cavity itself, which would result in lowering the intra-cavity photon number at higher drive powers due to shifting the cavity resonance frequency. Could the authors argue if such an effect occurs in their device?

At large mechanical amplitudes, the cavity frequency is shifted by the mechanical motion. This reduces the efficiency of the drive, and thus decreases the power in the sidebands. In the revised version of the figure, we fixed this error. The optomechanical nonlinearity (which scales with mechanical displacement) can be treated mathematically as a Kerr-like nonlinearity, but we do not see any pure Kerr nonlinearity (which scales with photon number) in our microwave circuit at the powers we use.

6) It is assumed that the Al thin film is of type I. However, I would guess that the film contains small Al grains such that it may be possible that flux lines could penetrate it (at grain boundaries). A recent study showed that the London penetration depth of Al thin films can be as large as the film thickness itself (e.g., arXiv:2311.14119).

The question of the likelihood of vortices threading the drums is very interesting, although, as we argue below, likely quantitatively irrelevant for the present experiment. First, let us note that the sample is here not exposed to significant magnetic fields. The cryostat in which these experiments were performed has a room-temperature mu-metal shield, and no other magnetic field is applied to the sample. Nonetheless, the referee is correct about the penetration depth in thin films, and signatures of single-quantum vortices have been observed in similar (although thinner) aluminium thin films (for example C. Wang et al., Nature Commun., **5**, 5836 (2014) or M. Foltyn et al., PRAppl, **19**, 44073 (2023). The top plate of our drum is 120 nm thick where, in the reference cited by the referee, arXiv:2311.14119, a 100nm film has a penetration depth of $63 - 69$ nm (not too far from the bulk value). Based on these numbers, the top plate alone would already not be in the thin-film limit. While the bottom plate is thinner, and more likely to host vortices, the magnetic behavior of the drum likely resembles that of a single block of superconducting material with a thickness closer to 200 nm due to the close proximity of the two aluminium layers.

While we have not directly measured the penetration depth, we have realized resistivity measurements of films similar to the ones used for drums and having undergone all our fabrication steps that might introduce roughness or impurities. We found the resistivity at the transition temperature 1.2 K to be $1.8 \times 10^{-8}\,\Omega \cdot \mathrm{m}$. Using expressions for the penetration depth close to the thin/thick film transition from e.g. Zmuidzinas, Annu. Rev. Condens. Matter Phys., vol. 3, 169–214 (2012), (equations 8 and 12 of that paper) we estimate the penetration depth to be 80 nm for a 200 nm thick film and 130 nm for a 120 nm thick film like the top plate of the drum. We think that the effective penetration depth relevant in this case must sit between these two numbers, but this still puts the drum stack likely outside of the thin film limit (by a small margin). Therefore, we think it not likely that our drum admits vortices.

How would flux penetration (or non-ideal type I behavior) influence the inference of the Casimir force, ie, the exponent of the force-distance relation and the Casimir pressure?

Notwithstanding our answer to the previous point, it is interesting to consider how flux penetration (or non-ideal type I behavior) would influence the inference of the Casimir force. If the drum accepted single-quantum vortices, then we calculate that the magnetic flux density of the Earth's magnetic field would corresponds to 2 to 3 vortices over the surface of the drum. We have estimated that each vortex would apply a force of the order of some picoNewtons. The total equivalent pressure over the area of the drum would be 0.04 Pa, which is negligible compared to the pressure at equilibrium (12 000 Pa) that we observe in this experiment.

7) Along the lines of point 6), if the film can trap flux, this could result in an additional force acting on the mechanical oscillator. As the magnetic field of a flux line is highly non-uniform, it may also lead to a nonlinear force-distance relation. Could the authors estimate the effect of trapped flux on the motion of the mechanical oscillator, ie, on its potential?

We believe that one vortex would thread the whole stack of the drum, because this is the situation that minimizes the energy cost of bending the magnetic flux lines. We have confirmed this by simulating this situation. This means the vortex applies an attractive force between the two plates of the drum resonator, to minimize the bending of flux lines in the gap between the plates. To estimate the magnitude of this force, we take the model for the magnetic field configuration above a vortex from G. Carneiro et al., PRB **61**, 6370 (2000). They find the flux lines in the vicinity of a superconducting object at the location of a vortex are those of a magnetic monopole that would be buried a distance λ (penetration depth) into the superconductor. We then expect that the force applied on two plates scales as the force between two "magnetic charges" of opposite polarities, that is, as $1/(d+2\lambda)^2$. Therefore, we believe that, if there was a vortex in the drum, it would result in a potential that is nonlinear, softening like the Casimir force, with a scaling exponent $n \simeq 2$ with respect to the separation distance (lower than that of the Casimir force exponent). However, as explained above, we expect the magnitude of this force to be negligible in the present experiment.

8) The abstract introduces that the Casimir force between superconducting plates is still not fully understood, quoting from the abstract: "...There is significant interest in this contribution as it is suspected to contribute to an unexplained discrepancy between predictions and measurements of the Casimir force". However, the authors use the results of Ref 28 to calculate their expected Casimir force, which seems to contradict the statement from the abstract. Using Ref 28, it seems that the Casimir force can be calculated for the specific situation the authors analyze. Hence, I would suggest to reformulate the statement in the abstract as I find it misleading, or this statement needs to be addressed in the main manuscript by comparing to the said discrepancies between (previous) experiments and theory.

The discrepancy we refer to is between the values of the finite temperature Casimir force calculated using the Drude model and the experimentally measured results (as discussed in V. M. Mostepanenko, Universe **7** 84 (2021)). Although unexplained, this discrepancy remains relatively small. The work by G. Bimonte, Phys. Rev. A **99** 052507 (2019) gives a method to calculate the Casimir force using different material models (BCS, Drude), taking account many experimentally relevant details. Since the origin of the discrepancy is not known, this is currently the best model to our knowledge to calculate the Casimir force. We have rephrased the statement in the abstract for clarity, and added an additional sentence in the introduction with references relevant for this topic.

9) Further, the statement "... By contrast, the strong nonlinearity imparted by the Casimir potential can be easily shown without relying on the force-distance scaling." seems to be misleading. The present work makes full use of the nonlinear force-distance relation. Only this nonlinear relation leads to the nonlinear behavior of the mechanical drum oscillator. Hence, I would encourage the authors to rewrite this part. I am aware of the fact that the present work does not statically tune the position of the drum plate. However, the present experiment still makes full use of the nonlinear Casimir force-distance relation, which influences the dynamic behavior of the drum oscillation amplitude.

The referee is right, we have rephrased the sentence. It now refers to cryogenic positioners instead.

10) I do not understand the statement of an "imperfect material". What do the authors mean with that statement in relation to using BCS theory to estimate the Casimir force, ie, what does the said "imperfection" refer to?

This is indeed a wrong choice of words from our part. What we meant is a "real" (realistic) material as opposed to an ideal conductor. Following a relatively standard prescription for Casimir forces in superconductors, the material's optical response is modeled with the conductivity given by Drude model, except for frequencies of the order of or lower than (twice) that of the superconducting gap, where the optical response is modified significantly from the Drude model (and is modeled by the Mattis-Bardeen theory).

11) How is the maximal mechanical displacement of 100pm determined?

We use a calibration procedure that is described in the Supplementary sections A 3 and C 5. Put briefly, we rely on the fact that the relative powers in multiple sidebands (e.g., the first red and the first blue sideband) are described by the optomechanical equations of motion and are not affected by attenuation on the input lines or amplification on the output lines. We use independent calibration methods to obtain all relevant optomechanical parameters (g_0, κ, Δ, ω_m, ω_c) and iteratively refine our model until the powers of all sidebands are predicted correctly for all combinations of drive powers that we use in the experiment. This is shown in Figs. S2-S4. We have made extensive changes to the text in the 'Calibration' section to clarify the calibration procedure by which we obtain the maximum displacement of around 100 pm.

12) A question motivated by curiosity: could the Casimir force potentially lead to additional mechanical damping/decoherence or even nonlinear damping?

To our knowledge, the Casimir force can be considered conservative - in the configuration of this work at least, that is, where the velocity of all parts of the drum is much smaller than the speed of light. That is, the Casimir force does not act as a viscous or damping force, but as a conservative nonlinear potential. That said, a Duffing oscillator coupled to a thermal bath is expected to display nonexponential relaxation that depends on the initial condition (see e.g., M.I. Dykman and M.A. Krivoglaz, Sov. Sci. Rev. A Phys. 5,

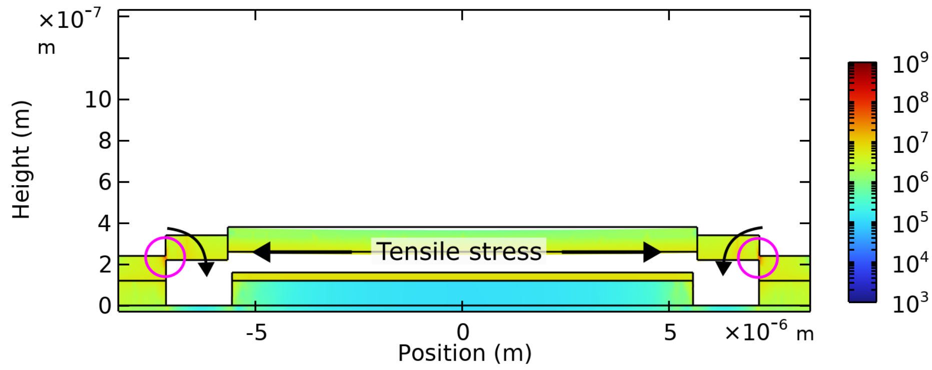

Figure 1: Plot of the von Mises stress in a cut of the drum and direction of the torque on the edges.

265-442 (1984) Sec. 2.3), which can be considered as nonlinear damping. We expect that this is also the case of other nonlinearities, and the expansion of the Casimir force in small oscillations with respect to the vacuum gap contains a Duffing term $\propto x^3$, so we expect that this type of relaxation could be met here too. However, these effects are calculated to be negligible for such low levels of thermal fluctuations as in our experiments.

13) The authors simulate the resonance frequency of the drum at room temperature, which is expected to be 5.4MHz. Have the authors measured this frequency at room temperature, eg, using optical interferometry to verify their simulation result?

This would be a relevant measurement, however, we have not carried it out, and the specific sample used for the experiments in this paper was broken as it was warmed up from cryogenic to room temperature, so we cannot measure its mechanical frequency any longer.

14) I am a little confused by a statement in the Methods section on "Drum frequency and effective mass". It is said that the small tensile stress leads to sacking of the top plate. Normally, I would expect that compressive stress only leads to sacking, while tensile stress leads to straightening/stiffening. How can I understand this statement?

We agree that a buckling of the membrane closer to the substrate, giving a sagging shape to the membrane, might be expected in the presence of compressive stress. However, the deformation we see is not a result of buckling, but of tensile stress. The tensile stress comes from the fact that the metallic membrane contracts more than the quartz substrate when cooling the device down to cryogenic temperatures. Tensile stress is translated as a torque on the weaker points of the drum indicated by the pink circles in Fig. 1 of this reply. Since the drum top plate is pulled from its edges by the tension, the edges "unfold", flatten, and the drum is deformed such that it comes closer to the bottom plate. Our choice of the word "sagging" might have evoked the idea of slackness and oppose the idea of tensioning, so we have replaced this word by less connoted ones in the main text.

15) The authors refer to their previous work Ref 62 in SI, where they introduce a formalism of estimating patch potentials. It would be good to give a summary of this work even in the main part of the work, eg, in the Methods section. Patch potentials are of major concern in the experiments the authors perform. Hence, a more elaborate discussion in the main part of their work would be beneficial to convince the reader that the influence of patch potentials can be neglected.

We have added a brief description of our motivation to exclude potential patches as the main cause of the nonlinearity observed in the 'discussion' section of the main text. We have furthermore expanded our description of the experiments and simulations around potential patches in the supplementary. It now includes the simulated patch pressures from patches of any size and a comparison to the Casimir pressure at various plate separations.

16) The Casimir exponent is obtained from Ref 28. However, would it be possible to obtain it directly from the measurements, ie, via fitting the data?

Obtaining an accurate fit of n without pre-existing knowledge of d and the Casimir pressure is challenging. We have written an extensive answer in reply to Referee 3, who asked a similar question. Put briefly: The exponent of the Casimir force n does not vary significantly for different material parameters, so there is little reason to attempt to extract n from fits to our data.

A few minor comments:

A) Fig S15 is the same as Fig S14, which is probably a mistake.

It was indeed a mistake. We have fixed this in the revised version.

B) Methods section: Eqn. 12 contains the symbol ω, should it be ω_d?

Indeed, it should have been ω_d, we have fixed this in the revised version.

Reviewer 2

In this work, the authors use a superconducting electromechanical circuit to measure the nonlinearity of a mechanical resonator. Through a series of careful measurements and calibrations, the authors demonstrate that this measured nonlinearity is quantitatively consistent with what is expected from the Casimir effect. The Casimir effect is a purely quantum effect in which vacuum fluctuations of the electromagnetic field impart a measurable force on surfaces which are sufficiently close together. By ruling out other potential sources of mechanical nonlinearity, they conclude that their data should be interpreted as the first measurement of the Casimir force between two superconducting electrodes.

I find this work to be thorough, novel and important. The hallmark of the Casimir effect is the strong power law dependence of the force with distance. Instead of measuring how a microelectromechanical system responds to static changes in the plate separation, they observe the how the system responds to large amplitude AC displacements. Specifically, the observed softening nonlinearity of the mechanical response function appears to show excellent agreement with theoretical predictions of the expected Casimir behavior.

We thank the reviewer for their kind statements about the thoroughness, novelty, and impact of our work.

However, before fully recommending publication I have several important questions that I would like the authors to address.

1. The abstract and introduction state multiple times that this effect is measured "for the first time." I find this claim of priority unnecessary and slightly contentious. As the authors reference in their manuscript, other electromechanical circuits have shown behavior that is only consistent with Casimir behavior (reference 29 in the main text). While this prior work did not exhaustively rule out other possible explanations for the data, it also showed excellent quantitative agreement with Casimir theory. In my opinion, this current manuscript is sufficiently interesting and important to be published without making the claim to be first.

We have removed our claim to be the first to measure the Casimir force between superconductors. We agree that the work of R. W. Andrews et al., Nat. Commun. **6** 10021 (2015) showed behavior consistent with the Casimir force, and we were also made aware of the PhD thesis of H. Eerkens (Leiden University (2017)) that shows the Casimir force between superconductors.

2. As the heart of this work is a quantitative measurement of the Casimir nonlinearity, the manuscript should be perfectly clear what the variables d and x refer to. Is this the displacement at the center of the of the capacitor, or the average plate separation over the capacitor area, or effective displacement averaged over the entire mechanical mode shape? Likewise for the AC displacements are the calibrated and measured displacement powers (in nm^2) the peak-to-peak or the mean-square amplitude?

We have improved the terminology in the first part of the Results section and added an annotation of the direction and zero of x to Fig. 1**a**. We realized that we should have been more precise in defining what x represents exactly: In Eq. (1), x denotes the displacement of an 1D oscillator representing the drum. We set x to be zero when the drum top plate would be positioned at a distance d' from the bottom plate, which would be the equilibrium situation in absence of the Casimir force. Due to the Casimir force, the equilibrium value of x is eventually around $-2.9\,\mathrm{nm}$, as shown in Fig. S8. In our experiment we measure the optomechanical response, given by Eq. (2), which contains $\hat{x}$, and the spectra we record do not show the static value of the displacement, but only the power of its vibrations around equilibrium. Our microwave equipment (e.g. spectrum analyzer) defaults to the RMS power when it records the power in these vibrations, so we use that whenever we use units of power across the paper. Note that $\hat{x}$ from Eq. (2) is defined with a different zero than from x of Eq. (1): $\hat{x}$ describes the displacement relevant for the optomechanical framework, which does not contain the static displacement from the Casimir force term of Eq. (1), so that its equilibrium value is zero. Finally, note that the effective mass attributed to the effective oscillator is defined such that the kinetic energy of the effective oscillator x measured through g_0 matches the kinetic energy of the drum's displacement field (and equivalently with this effective mass the effective oscillator's potential energy matches the drum's potential energy and the zero-point fluctuations which serve to define g_0 in the optomechanical framework are also the same).

In Figs. 1 and 2, we show the measured power in the optomechanical response to a drive close to resonance frequency ω_m. This contains the displacement power around the equilibrium position. We compare it to numerical solutions of Eq. (1), where we apply a drive at similar frequencies close to ω_m and extract the amplitude of the limit cycle orbit from MatCont. The theory curves in Figs. 1 and 2 show the amplitude of this orbit, which includes the Casimir nonlinearity at high powers.

d is the rest separation between the two capacitor plates in absence of Casimir force. Since the Casimir force cannot be turned off, it has limited physical significance but it serves as an important calculation intermediate. The Casimir force shifts the equilibrium position of oscillator x away from the rest position it has without the Casimir force, to a position we call d' (so we refer to d' as the 'equilibrium separation' in the revised version of the work).

3. All four figures of the paper show essentially the same type of data... mechanical response functions as a function of drive powers. It is not clear if the data in fig 1c is different from what is shown in fig 2 or just a subset? If so, why is it being shown twice?

The data in Fig. 2b is indeed the same as in Fig. 1c, we had shown it in both places as Fig. 1c is meant to display strong nonlinear responses measured while Fig. 2 was meant to show fits across all power combinations (including for the highest powers already shown in Fig. 1c). We have now removed panel b of Fig 2 to avoid this repeat. Fig. 3 concerns details of the analysis and indeed shows the same type of data, and Fig 4. shows other measured sidebands which are not exactly the same type of data.

4. While it is impressive that the entire data sets in fig's 1,2,3,4 can be well fit by a single fit parameter for the nonlinearity, that is what one would expect for any single nonlinearity. This clearly demonstrates that the all the data is self-consistent and that the authors faithfully understand how microwave drive powers scale with mechanical displacement over many orders of magnitude. The most crucial part of this entire paper is the calibration to real amplitude units. My understanding is this absolute calibration of the motion in meters comes fundamentally from measuring the thermal motion at a known temperature, and using the equipartition theorem as a primary displacement calibration. Is this correct? If so, the authors should state this more clearly. It is my understanding that without this thermal calibration, there would be an ambiguity in the absolute amplitude of the motion due to the unknown attention of the microwave cables

and unknown gain of the microwave amplifiers. It is only with this absolute calibration that these measurements can quantitatively compare with Casimir. Also, if this is the case, does that mean that the uncertainty on g_0 should be the dominant uncertainty in the absolute plate separation determination?

We have expanded the description of our calibration method in the revised version. We perform a calibration based on the thermal motion (Suppl. Sec. C5) to infer several parameters of the sample (g_0, G, ω_m, γ_m and a measurement gain). However, this calibration based on noise measurement cannot be directly used to interpret optomechanical *responses* of our device and in particular extract a mechanical displacement. The response signal comes from interfering terms from the input power reflected on the cavity and power transduced from the mechanical oscillator, and the interference's amplitude does not depend only on the mechanical signal's amplitude. Therefore, we rely on a different method for the amplitude calibration (Suppl. Sec. A3). We make use of the fact that we have multiple sidebands, since our mechanical amplitude is large. The relative power of the two sidebands is described fully by the optomechanical equations of motion. We can calibrate the optomechanical parameters κ, g_0, Δ, and ω_m independently. Since this method only looks at the relative power in the sidebands, it is unaffected by cable loss and amplifier gain. We solve the optomechanical equations of motion for various combinations of (absolute) powers of the cavity drive (at ω_mw) and red-sideband drive (at ω_sb), and compare the powers in the sidebands of the output spectra to the observed powers. Our calibration results (Figs. S2-S4) show that the calculated sideband powers agree very well with the observed sideband powers for all combinations of drive powers. The uncertainty on g_0 is indeed the dominant uncertainty in this calibration, because all other parameters (κ, Δ, and ω_m) can be determined very accurately by independent measurements.

5. As with all weak nonlinearities, to lowest order the Casimir nonlinearity can be cast as a Duffing correction or a Kerr coefficient in which the mechanical frequency shifts as the amplitude of motion is increased. It would be useful for the reader to quantify what this Duffing or Kerr coefficient is for the current device, in both nanometers or phonon number. This would help elucidate how close (or far) the current device is from a full qubit regime in which a single phonon shifts the mechanical resonance frequency by more than a mechanical linewidth.

The lowest order of the nonlinearity from the Casimir force is not a Duffing correction proportional to x^3 but a x^2 term. Furthermore, the truncation of the series expansion of the force is not a very good approximation here. Expanding the term from Eq. (1), $\frac{P}{(x+d)^n}\frac{\pi r^2}{m_\mathrm{eff}}$, yields

$$\frac{P\pi r^2}{m_\mathrm{eff} d^n}\left(1+\frac{x}{d}\right)^{-n} = \frac{P\pi r^2}{m_\mathrm{eff} d^n}\left\{1 - n\frac{x}{d} + \frac{n(n+1)}{2!}\left(\frac{x}{d}\right)^2 - \frac{n(n+1)(n+2)}{3!}\left(\frac{x}{d}\right)^3 + \ldots\right\}. \tag{1}$$

The odd terms are negative and the even terms are positive. One can extract the first four coefficients (c_0, $c_1 x$, $c_2 x^2$, $c_3 x^3$), they are $c_0 = 1.7\cdot 10^7\ \mathrm{m\,s^{-2}}$, $c_1 = -3.0\cdot 10^{15}\ \mathrm{s^{-2}}$, $c_2 = 3.6\cdot 10^{23}\ \mathrm{m^{-1}\,s^{-2}}$, and $c_3 = -3.4\cdot 10^{31}\ \mathrm{m^{-2}\,s^{-2}}$. Evaluating the above expression for different values of x shows that the lowest terms are not necessarily the largest. An earlier work on the Casimir nonlinearity (H. B. Chan et al., Phys. Rev. Lett. **87**(21) 211801 (2001)) used this series expansion truncated after the third term, but found that it caused a discrepancy at high drive amplitudes. To avoid this, we chose to fit with the original force expression rather than to truncate the expansion.

Our current device is quite far from the qubit regime, as the nonlinearity becomes visible in the mechanical response only when the resonator is strongly driven to the order of 10^4 phonons. However, the nonlinearity should be tunable by applying an electrostatic force like in R. W. Andrews et al., Nat. Commun. **6** 10021 (2015).

6. There is very little detail on the microwave resonant circuit. What is the inductance and parasitic capacitance of the resonator? Is there a picture of the geometry or a reference to previous work that uses a similar geometry. Specifically, it is surprising that the extremely close final plate separation shown here (15 nm) does not have a bigger g_0. Is this because there is a large amount of extraneous capacitance in the circuit? It is important to show that the measured g_0 also self-consistently agrees with the inferred cold plate separation.

We have added several paragraphs to the supplementary C1 where we describe the microwave circuit. The geometry of the circuit is shown in a figure which we have also added to the revised version (Fig. S8). We have replied in point 4 of referee 1 that our simulations predict a coupling rate $g_0 \simeq 2\pi \times 480$ Hz, but that this is an overestimation due to the shape of our mechanical mode. Our experimentally calibrated coupling rate, $g_0 = 2\pi \times 150 \pm 9.2$ Hz, is larger than is typical in these devices, because the plate separation is smaller. Typically we measure coupling rates on the order of $10 - 40$ Hz.

Minor comments and suggestions:

A. Figure 1c. There is a discontinuity in the data at a detuning of 2 kHz. I assume the authors did this to help clearly show that they have good fits over a large range in frequency and power. I had to look at the figure many times to understand that the kink in the data was an artifact of how it was being plotted. I would recommend either plotting all of the data and using insets or zoom-ins to show that all features. Or alternatively, at least showing a clear gap in the data and axes so the reader immediately sees that the plot is over a discontinuous frequency range.

We apologize for any confusion caused by lack of clarity in the figure. We have significantly revised Fig. 1: We have made Fig. 1c contain two panels, where one is a zoom on a small region of the other panel.

B. On page 2, In the paragraph after equation (1), the text states: "...where $n = -3.193 \pm 0.005$ is fitted from BCS theory." I believe that n should be a positive number that way it is defined here.

The referee is correct, we have fixed this error.

C. On page 8 of the main text, the manuscript says: "When we compute the thermal expansion down to 10mK..." I believe this should read "When we compute the thermal contraction down to 10mk..."

The referee is right, we have replaced the instances of 'thermal expansion' by 'thermal contraction'.

D. The authors determine from their COMSOL modeling that mechanical frequency at room temperature should be approximately 5.4 MHz. Have the authors tried to measure the room temperature mechanical frequency? Obviously, not using the superconducting resonator, but a room temperature vibrometer measurement of the resonance frequency could give additional confidence to the model.

Unfortunately, the device that we studied in this work collapsed as the cryostat in which it was mounted was warmed up, so we cannot measure its frequency anymore.

E. The authors measure only the magnitude of the mechanical response function throughout the text. It seems like they should also be able to measure the full vector response function, including phase of the mechanical resonance. Specifically, using a vector network analyzer and a room-temperature mixer (instead of a spectrum analyzer) would give access to this information. While I don't think there would be anything surprising in the phase information, if the authors have measured it, showing it would help demonstrate full understanding of the mechanical mode and the Casimir nonlinearity.

We appreciate the referee's suggestion regarding the phase information, but we do not expect to be able to gain additional accuracy/precision on the Casimir nonlinearity from the phase. In the work by Perez-Morelo et al., Microsyst. Nanoeng. **6**, 115 (2020), the phase response behaves as expected for a nonlinear mechanical resonator. We cannot reach the unstable branch of the nonlinearity, and we are limited by the decay of the high-amplitude branch, so the range of phase information we can extract is limited. However, we plan to explore both the amplitude and phase of a drum with a strong Casimir nonlinearity in future experiments.

Reviewer 3

In the manuscript, the authors study the nonlinear mechanical response of a capacitive microwave optomechanical device. The gap in their device is found to be very small, on the order of 18 nm, allowing them to explore possible corrections to the usual electrostatic forces between the capacitor plates at small distances through the nonlinear mechanical response. The idea is that by employing calibrations that are possible with optomechanics, the nonlinear mechanical response can reveal quantitative information about distance scaling of the forces between the plates. Their observations and analysis suggest the observation of a inverse power law scaling of the forces between the plates, which they argue is in quantitative agreement with predictions of Casimir forces.

This is, naturally, not the first work studying forces between metal objects at small distances in an attempt to observe Casimir forces. And, of course, at these distance scales, in which retardation effects of light propagation between the plates is not relevant, there is a natural alternative interpretation of the Casimir force as a distributed equivalent of the van der Waals force, well known and established in chemistry and also the MEMS community as the underlying origin of stiction and snap-in.

We would like to note that experimental work by G. Palasantzas et al., Appl. Phys. Lett. **93** 121912 (2008) showed that the effective threshold of distance between realistic surfaces (e.g., with non-negligible roughness) that separate the van der Waals and the Casimir regimes is of the order of 10% of the plasma wavelength. For aluminium, this crossover is expected around 9.5 nm, which is below our equilibrium spacing of 15.1 nm, and we therefore consider that our device is sensitive to the Casimir force rather than the van der Waals force. While these numbers look close to each other, let us also note that the van der Waals and Casimir forces are generally defined as *limit* cases of the dispersion force (see e.g., E. M. Lifshitz, JETP **2**(1) 73-83 (1956)). The van der Waals regime is defined as the regime in which retardation effects become negligible, so the inter-object distance would need to be much smaller than the threshold. In the Casimir regime, the retardation effects dominate when the inter-object distance is larger than the threshold.

The Lifshitz model for the estimation of Casimir forces predicts the transition from the Casimir limit to the van der Waals regime at short distances, as illustrated in the figure below. In our equation of motion for the mechanics (Eq. (1)), we use the fitted strength and scaling of the Casimir force that is shown by the dotted line in the figure. The van der Waals regime appears at separations of 1-3 nanometers.

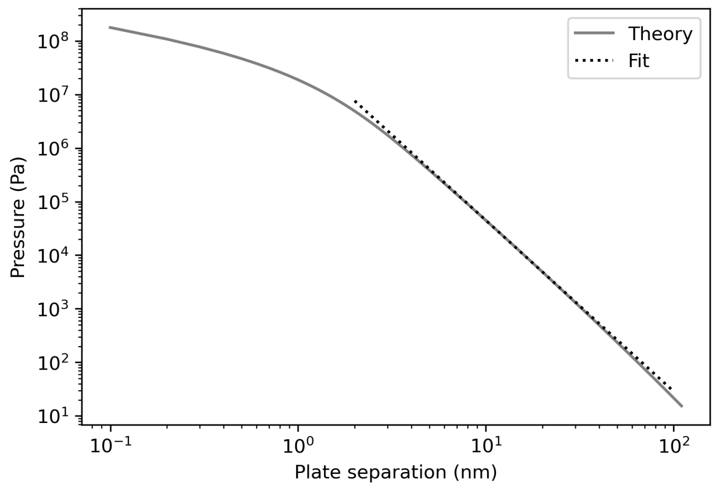

Figure 2: Calculation of the pressure across a large range of distances in the Casimir theory formalism. The dotted line shows the Casimir force expression used in the main text.

This is also not the first work to employ microwave optomechanical devices to imply the existence of attractive power law forces between the plates in a capacitive electromechanics device, and in particular, one could argue that the existence of these forces was already clearly established in the 2015 work from the NIST group (https://www.nature.com/articles/ncomms10021) in the tuning response of the microwave cavity and mechanical resonator frequencies as a function of static voltage (figure 1). This submitted manuscript supplements this earlier work by pointing out, and quantitatively explore, the fact that attractive force power laws will also modify the effective high amplitude dynamical response of the mechanical resonator even at *fixed* capacitor spacings, which I feel is a nice result that clearly warrants publication and which is a significant advance over the current state of the art in the field. In this sense, we are very positive about the work!

We thank the referee for their positive comments, and have rectified our claims of being the first to observe the attractive power law. Indeed, the work by R. W. Andrews et al., Nat. Commun. 6 10021 (2015) shows the Casimir force, although they phrased their claim carefully and did not exclude the possibility that the observed signature came from patch forces. Retrospectively, we believe that also in their configuration, which is very close to ours, the Casimir force must have strongly dominated over the patch force. However, this signature was mentioned in passing in that article and was not the focus of that work. In the PhD thesis of H. Eerkens (Leiden University (2017)), there is experimental evidence of the Casimir force between superconductors, and for that instance at least we are particularly apologetic about our oversight. In the revised manuscript, we refer to both these earlier works.

That said, we found the work to be very difficult to read and extract what exactly was done, and what are the underlying assumptions, which observations represent true independent measurements, and exactly on what basis the conclusions are drawn. For this, we include below a list of detailed questions that we believe should be addressed by changes to the manuscript should it proceed further towards publication.

In the revised version, we have made adjustments to the text regarding the calibrations and observations we have done, and hope that it is more easily legible. Most of the technical details have been moved to the supplementary, however our calibration process is complicated and the text is somewhat lengthy as a result of that.

In addition to the very nice work explaining how to observe the power law attractive forces between the plates, the manuscript makes an explicit claim in the abstract and throughout that they have unambiguously been able to prove that the power law forces they observe are from a Casimir origin, going further than any other work in the long list of experimental Casimir literature, somehow excluding the possibility of surface charges and patch potentials in their observations. We do not believe that the authors can make this claim: the additional checks that have been done ex-situ in our eyes do not satisfy the burden of proof that is required to distinguish them from all of the other experiments performed in the Casimir literature. On the other hand, we also do not believe that this claim is required for the manuscript to satisfy the impact ambitions of the Nature Communications journal, and would be happy to accept it for publication if this claim of unambiguous observation of Casimir forces is reduced to a claim of power law attractive forces consistent with Casimir, but which cannot completely exclude the possibility of patch potentials playing a role (as was done by the NIST group in the Nature Communications work linked above). If the authors refuse to soften this claim, then we are unable to accept this work in any form for publication.

We thank the referee(s) for their thorough reading of our work. We have significantly expanded the description of our checks on patch potentials in the revised version (Supplementary Section E2). We show that due to our small vacuum gap at equilibrium, $d' = 15$ nm, the Casimir pressure is orders of magnitude larger than the pressure exerted by patch potentials (of any size). We have furthermore added a description of our extensive KPFM measurements during the various stages of fabrication, on multiple samples, and from that we show that the patch potentials do not vary much between samples or during the fabrication. Based on this, we feel confident that our work sufficiently strongly excludes potential patches as a possible explanation for the strength of the nonlinear effects that we observed. We have given a more detailed answer on this matter in the detailed questions of the referee(s), below.

Major Discussion Points

Calculation of the Casimir pressure.

Figure 5 shows the Casimir pressure calculated using the Lifshitz formula and the BCS model. The Casimir pressure is evaluated for distances between 20nm and 120nm and subsequently fitted with $P = (69.6)\mathrm{MPa}/(d^{3.193})$. Throughout the paper, the unperturbed distance is determined at 18nm. Please show that this relation also holds in the d = 15 nm - 20 nm range, since this is the actual range of the determined gap distance. Furthermore, the inset in the figure reports a different value for n than is used throughout the rest of the main text.

We apologize to the referees, as an older version of this figure has been accidentally put in the submitted version. The correct version of Figure 5 should have been the one below.

The correct version of this figure shows the value of n stated in the paper, and shows that it fits to the calculated Casimir force in the distance range which our system operates. In the revised version, we have furthermore clarified the expression of the Casimir force by distinguishing the Casimir pressure calculated by the Lifshitz formula (now P_c in the main text) from the fit parameters, Casimir pressure amplitude (P) and scaling (n).

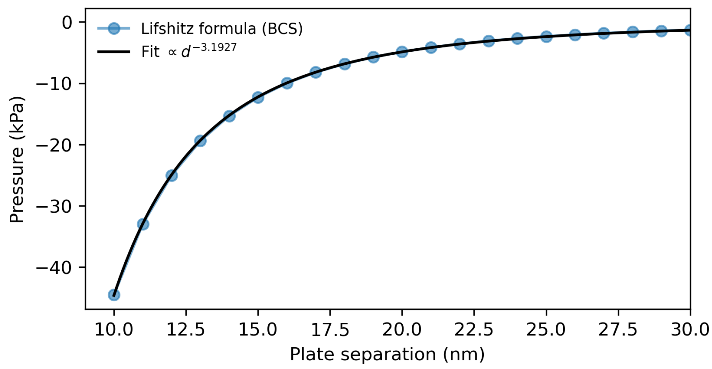

Figure 3: The correct version of Fig. 5.

Fitting the Measurement Data

Looking at the device and experiments, the most logical calibration process we see is the following:

- Calibrate the unperturbed gap distance d from the microwave cavity frequency.
- Use an optomechanical thermal calibration to calibrate sideband power into oscillation amplitude in nm, or in your case displacement power in nm^2.
- suspicious that they seem to equilibrate to 10 mK? but OK, literature has shown 20 mK (Tuefel 2010) for similar devices
- The optomechanical calibration also gives a calibration of the optomechanical forces by doing a power sweep, which increases the oscillating actuation force. From the response, you can get access to the type and amplitude of the dynamic nonlinearity (x^3, x^4, x^5, x^6, etc).
- From that, you can compare the theory for different values of n, which you compare to the predictions from the Casimir force nonlinearity.

We agree that the calibration process suggested by the referee(s) would be preferable, but we estimate that the knowledge of the microwave cavity frequency does not give an accurate estimate of the distance d. Indeed, it depends quite crucially on fabrication and experimental details. These details are of no qualitative consequence for the experiments, however, we do not trust the accuracy of fabrication designs to the extent that we use them as a foundation for our calibrations. Instead, we developed a calibration scheme based on the relative powers of two sidebands, as described in the (revised version of the) main text, and in Suppl. Sec. C3.

Also, we have systematically realized thermalization measurements of all devices of this type used across the years. Such samples are all thermalized down to $10-15$ mK depending on samples. A thermalization down to 10 mK is in the bottom of this range but not exceptional for this type of samples. The cryostat used for this experiment has a base temperature of 7 mK according to two different thermometers, one of which was freshly recalibrated.

However, we see a different approach here and in the main text where the power law dependence (n = 3.193) is predicted from theory. That raises a few matters:

1. d and n seem to have very strong correlations (Figure S7) In Figure S7, parameters d and n seem to have strong correlations, since they shape the response in a similar way.

Yet in this work, it seems that n is fixed beforehand through theory calculations, under the assumption that the Casimir force is at work. If they are uncorrelated, we would understand this choice in procedure but otherwise not. Therefore, we would like to see the error surface of your fits that explain to us how (un)correlated d and n are and what the implications are for the conclusions of this paper.

The referees are right to note that n and d are strongly correlated. Indeed we chose to show these correlations in Fig. S9 (formerly Fig. S7 in the previous version of the paper). However, we are not letting freedom on n in fits. One obvious reason for this is that precisely n and d are correlated so fits would not be of very good quality. The *justification* for allowing ourselves to fix n comes from the fact that (1) we are not using the value of n to propose that the force at play is a Casimir force, instead we are fitting the data with a Casimir force model and (2) n is rather well known from theory. The Casimir scaling n is minimally affected by variations in the material parameters, especially compared to the Casimir pressure amplitude P, which is much more sensitive: A 25% variation in plasma frequency Ω_p yields about a 25% variation in pressure amplitude P, but less than a 1% variation in scaling n. Since the optical parameters of aluminium have been studied extensively, their uncertainty is much lower than 25%, and so that neglecting variations in n does not affect our conclusions. Furthermore, we show in Fig. S6 that large variations in the Casimir parameters change our fit of d only marginally. This motivated our choice to only consider the error from the amplitude calibration, and neglect errors from uncertainty in the Casimir/material parameters. For completeness, we report in Table 1 our estimate on the uncertainty on d, but we also translate this uncertainty back into an uncertainty on the Casimir pressure and reported that as well.

2. Single Fit Parameter

In your main text and Figures, the term “single fit parameter” is often mentioned. In Figure 2, it is referring to the right y-axis, implying that the only “fitting” is a scale factor between the measured power and the displacement power of the mechanical resonator. However, if you properly calibrated the sideband power with the average phonon number in your mechanical resonator, this would not be a fit parameter but a well-calibrated number.

The referee(s) are correct, we should have been more clear about this. The fit parameter is d and the relative offset between the left and right axes of Fig 1c and 2 follows from our calibration. We have reworded several parts of the main text to clarify this point.

Then, you mention in the Methods under “Drum Frequency and Effective Mass”, that “While we consider that the simulation method to estimate d is much less reliable than the fit to experimental data, the fact that these simulations independently yield the same value gives some confidence in this estimate.” This sentence implies that you fit d to the experimental results, which is also implied in Figure 3a: Please explicitly state the order of the individual calibrations and what exactly you mean with the "single fit parameter".

We have made significant changes in the text of the calibration section. We now explicitly state the order in which the calibrations follow each other. The amplitude calibration is based on the solution of optomechanical equations of motion, where we compare the relative powers in two sidebands (the first red and first blue sideband), and the directly-reflected power from when the sideband-drive is detuned from $\omega_{\mathrm{c}} - \omega_{\mathrm{m}}$. We obtained the parameters κ, Δ, ω_{m}, and g_0 from earlier, independent measurements. We solve the optomechanical equations of motion for all combinations of drive powers that we use, and compare the relative sideband power and off-resonant reflected power to the measured values in Figs. S2-S3. We find a good match for all combinations of drive powers using a single set of parameters, and then extract the mechanical amplitude from the optomechanical equations of motion.

3. Underlying assumption that the source is Casimir during the fitting procedure As we have stated before, you calculate the power law dependence (n) from the appropriate theory, from which d is calibrated with measurements. This seems like backwards logic, since it already assumed the force at play is the Casimir force. If your conclusion is that the nonlinear behaviour you observe is the Casimir force, then it should first be shown independently that d = 18 nm (or d' = 15.07 nm) through optomechanical measurements. Then, when you find n = 3.193 from measurements, you can start to argue that the Casimir force is at play. But strictly speaking, what you have shown is that when you assume that n = 3.193, the unperturbed gap distance d = 18nm will correspond to the nonlinear behaviour. You have therefore not excluded any other combination of d and n, which could possibly lead to the same result. This refers back to our first point, where we ask whether d and n are correlated parameters in the nonlinear measurements.

Here we first want to clarify the point and logic of this work. Our claim that the signatures we observe can be attributed to a Casimir force does not hinge on the value of d that we have fitted (or the value of n we have assumed). In this work, we measure a very strong nonlinearity and consider the following facts and assumptions:

1. We indeed assume that the Casimir force exists between closely spaced surfaces, which seems like a safe assumption given the wealth of experimental evidence of the Casimir force obtained in the last two decades. We also consider that its expression is fairly well known, and shows good agreement with a large part of the Casimir force experiments. The uncertainty on the optical response has very little impact on the exponent $n = 3.193$ that we have computed, and limited impact on the overall amplitude of the force (see Fig. S5).
2. We observe a strong mechanical nonlinearity in our superconducting optomechanical devices where the Casimir force should exist.We then set out to decide whether this nonlinearity can be attributed to the Casimir force or whether there are other significant contributions. To do this we determine whether the nonlinear signature is compatible with the relatively well-known expression of the Casimir force. Our experimental platform unfortunately lacks a convenient way to accurately measure d in situ. However, we can crudely estimate the cryogenic gap from the room-temperature gap and knowledge of the design and thermal contraction of the materials. But more importantly, we can evaluate the well-known expression of the Casimir force for all gaps d in a very safe range, $d \in [3 - 100\,\mathrm{nm}]$. With the ex-

cellent agreement between theory and experiments shown in our work, we conclude that the known expression of the Casimir force plausibly explains the signatures observed for $d = 18$ nm.

3. We furthermore consider all other sources of nonlinearity that we can think of, to determine if they could also explain the observed signatures. Of course, the evaluation of the impact of other attractive forces between the two plates of the drum depends on the knowledge of gap d (or d'), and we should not rely exclusively on the fitted value. So we estimate the other forces for a very safe range of gaps $d \in [3 - 100\,\mathrm{nm}]$. We find that the Casimir force is much larger than the patch pressure force (see our answer to the question concerning patch potentials below for more details) and the residual electrostatic force for gaps in this range. In the case of electrostatic force, the residual voltage would have to be in the range of 10 V, which is not compatible with the residual potential difference that one can expect between two surfaces made of the same material and galvanically connected. That is, an initial determination of the exact gap distance d is not required to suggest that the Casimir force dominates over the other forces that we mention in our configuration: with good certainty, the Casimir force is expected to dominate here. We describe in the supplementary section E that we can exclude geometric mechanical nonlinearity and the nonlinearity of the optomechanical coupling based on their relative strengths in more detail.

4. Having shown that the Casimir force is compatible with signatures with a plausible vacuum gap and that no other nonlinearity is in fact intense enough to produce these signatures, we conclude that the force at play is likely the Casimir force.

Ruling out patch potentials as source of the nonlinearity

Patch potentials result in a dipole-dipole-like attractive force that scales with $1/d^4$ when the separation distance is larger than the size of the effective dipole. This origin for a nonlinear force is very hard to rule out, and we appreciate the efforts taken by the authors by performing the ex-situ characterisation of the surfaces using Kelvin probe force microscopy.

However, the presence of smaller patch potentials in the aluminum or aluminum oxide, is not ruled out by the KPFM if the resolution is higher than the drum separation distance. Unlink AFM and STM, which are highly local probes due to the very strong decay of the tip interaction with distance, the capacitive nature of the Kelvin probe signal is inherently far less local, even if the tip is atomically sharp. For the reason, we do not believe that the KPFM can exclude patch potentials to a degree to make the strong claim of the authors of ruling out patch potential contributions to their observation. And, of course, the KPFM measurements are performed ex-situ, and not on the top and bottom interfaces of the actual device in the fridge: one cannot make the assumption that the nanometer scale surface characteristics are the same in our eyes.

We acknowledge that patch pressure should be considered in any proximity force experiment, and maybe the care that we brought to this question was still underrepresented in the article. As the referee notes, we have done what we could to measure patches in surfaces as similar as possible to the plates of the drum, by measuring surfaces that had undergone the same fabrication steps. To reflect this, we have now significantly expanded this description of the measurements of potential patches in the paper.

The referee(s) are correct to point out that the KPFM measurements cannot be realized in-situ in our device, but this is the case in most traditional Casimir-force-measurement platforms. However, we have found little difference in the patch distribution before and after any of the fabrication steps. Only the pre-release heat-treatment step seems to affect the patch distribution: it was found to reduce the standard deviation of the patch potential distribution from $\sigma = 63$ mV to $\sigma = 36$ mV. As the referee(s) point out, KPFM has a limited resolution. We adapt the work from G. Lévêque et al., Phys. Rev. B 71, 205419 (2005) to our situation, which yields an estimate of 16 nm, much smaller than the characteristic patch size of $\ell \simeq 160$ nm. Besides that, the limited resolution should *overestimate* the patch size, and therefore the patch contribution. Our device operates in the large-patch limit, $d' \ll \ell$, where the patch force scales $1/d^2$ but the Casimir force scales more strongly ($1/d^{3.193}$ in our device). As a consequence, the ratio of the patch pressure to Casimir pressure decreases as separation gaps decrease.

Furthermore, we have simulated the patch pressure for a variety of randomly generated patch textures with various potential and patch size distributions in another work (Arxiv 2408.16323). The main conclusion we draw from that work is that for experiments with separations $d' < 100$ nm, pressure from patches with $\sigma = 100$ mV normal voltage distribution is at least an order of magnitude smaller than the Casimir pressure (regardless of patch size). At separation gaps of some 10 nm, no realistic configuration of patches results in a patch pressure that is within orders of magnitude of the Casimir pressure (Figure S17). This conclusion is consistent with other estimates of the patch pressure: The seminal work on patch pressure in Casimir force experiments [Speake and Trenkel, PRL **90**, 160403 (2003)] estimates a conservative (large patch size) correction < 4% to the Casimir force. Carefully conducted later experiments such as [Decca et al. Annals of Phys. **318**, 37 (2005)] found much smaller patch pressures, a correction of the order of some 0.01% of the Casimir pressure even at much larger gaps (200 − 700 nm) than our experiment.

In conclusion, even without relying entirely on KPFM measurement of patches in our structures - which we still carried out to the extent possible - we believe that it is very unlikely that the patch pressure dominates or even contributes significantly to the observed force. That said, we have significantly expanded our discussion on the patch pressure in the revised supplementary.

Again, we reiterate that this is a nice addition to the work, but in our eyes does not provide the smoking-gun evidence the authors suggest in their claims. These claims should be softened for the manuscript to be publishable.

Minor Discussion Points

- In the introduction it is stated that resonators have been cooled close to the ground state. However, ground state cooling has been achieved multiple times, this should be mentioned and referenced accordingly.
  The referee is correct, we have removed the word 'close' from that sentence in the introduction. We have focused our references on earlier works studying superconducting drum resonators (our experimental platform) for brevity. Such drums have been cooled down to thermal occupations lower than 1 phonon, which is not exactly the ground state, but is usually considered close to be called this way.
- It is specified that d = 18 nm, but d' = d - 2.93 nm. Please be consistent with

significant numbers.
We have adjusted the number of significant figures to be consistent.

- The Casimir force in Equation (1) and in the main text right below scales with $d^n/(x+d)^n$. Could you explain why this is not $1/(x+d)^n$ like the Casimir pressure?
The referee(s) are correct, it should have been $1/(x+d)^n$. The d^n was mistakenly added from an earlier version of this equation, we have fixed it in the revised version.

- In Figure 3, please specify the drive powers of the microwave drives.
The data in Fig. 3a is identical to the green curve of Fig. 1c, measured at −20 dBm cavity drive and −30 dBm sideband drive. The data in Fig. 3c was measured at −20 dBm cavity drive and −10 dBm sideband drive. We have added these numbers to the manuscript.

- Based on Figure 7 in methods, the thickness of the aluminum is $\sim$ 120nm. Is this a sufficient thickness for aluminum to be a good Type 1 superconductor? If it is not, is the aluminum thickness considered in evaluating the Lifshitz equation?

  We have discussed the type I/type II character of aluminum thin films and drums in detail in our answer to referee 1's question about the potential presence of vortices in the drum. Essentially: the drum top plate is 120 nm thick and with the residual resistivity ratio (RRR) we measure, we are close to the limit between type-I and type-II behaviors. The presence of the 40 nm thick bottom electrode, pushes the drum to the type-I regime due to the small size of the gap. Notwithstanding that, the pressure exerted by any vortex or magnetic flux penetrating the drums is negligible compared to the Casimir pressure.

  Furthermore, to estimate the Fresnel coefficients, we have neglected the skin depth here. In other words, the film thickness is not a parameter that enters in the calculation of the Fresnel coefficients used in the Lifshitz formula. We expect this approximation to be reasonable in this case as the Casimir force is dominantly contributed by high frequencies for which the skin depth is negligible, i.e. for which the Fresnel coefficients are expected to be well estimated in this approximation.

- Can you clarify the scaling between measured power in dBm around the blue sideband, and the displacement power in nm^2 in the main text?

  The measured power (in dBm) can be converted to a photon number with a fixed scale (which we describe in Suppl. Sec. C5). However, the conversion from photon number to phonon number (or displacement power in nm^2) depends on the power in the cavity drive tone. This is perhaps not easy to see, but it follows from the optomechanical equations of motion. That is why we show the curves of Figs. 1**c** and 2**abc** at the same cavity drive power, and why the mapping from 'Measured power (dBm)' to 'Displacement power (nm^2)' is somewhat different for each of these panels.

- Quotation marks are oftentimes facing in the same direction, this LaTeX typesetting error should be corrected.
We have fixed these errors wherever we found them.

- Figure S15 in the SI "Potential patch statistics", is identical to S14 in the SI "Potential patches". This makes it impossible for the reviewer to verify the statistics mentioned in the text. Consequently, the reasoning to change the statistics of the

patch potentials in your simulations of the pressure is unclear. This seems to be an oversight.
We apologize to the reviewer(s), it was indeed an oversight (a typo in the figure file name). We have fixed it in the revised version.

Measurement of the Casimir force between superconductors

Matthijs H. J. de Jong,[1] Evren Korkmazgil,[1] Louise Banniard,[1] Mika A. Sillanpää,[1] and Laure Mercier de Lépinay[1,*]

[1]*Department of Applied Physics, Aalto University, FI-00076 Aalto, Finland*

(Dated: January 31, 2026)

The Casimir force follows from quantum fluctuations of the electromagnetic field and yields a nonlinear attractive force between closely spaced conductive objects. Its magnitude depends on the conductivity of the objects up to optical frequencies. Measuring the Casimir force in superconductors should allow to isolate frequency-specific contributions to the Casimir effect, as frequencies below the superconducting gap energy are expected to contribute differently than those above it. There is significant interest in this contribution as it is suspected to contribute to an unexplained discrepancy between predictions and measurements of the Casimir force between normal metals, which questions the basic principles on which estimates of the magnitude are based. Here, we observe the Casimir force between superconducting objects through the nonlinear dynamics it imparts to a superconducting drum resonator in a microwave optomechanical system. There is excellent agreement between the experiment and the Casimir force magnitude computed for this device across three orders of magnitude of displacement. Furthermore, the Casimir nonlinearity is intense enough that, with a modified design, this device type should operate in the single-phonon nonlinear regime. Accessing this regime has been a long-standing goal that would greatly facilitate quantum operations of mechanical resonators.

INTRODUCTION

A significant body of theoretical and experimental works over the last 20 years has focused on understanding the Casimir force[1–7]. This is motivated in part by the Casimir effect's practical applications in MEMS[8–13], but to a larger extent by its intimate connection to heat and energy transfer[14,15], especially at finite conductivity and temperature[16–19]. Furthermore, Casimir force experiments have also put bounds on Yukawa corrections to short-distance Newtonian gravity[20,21] and the Casimir effect has been proposed as a candidate to account for dark energy in cosmology[22]. Recently, the interplay between the Casimir force and superconductivity has garnered interest, either manifesting as a correction to the superconducting condensation energy[23,24], or as a correction to the electric permittivity of the material[25–28]. Studies of this interplay could shed light on the discrepancy between the calculated and experimentally observed Casimir force between real metals at finite temperature[19,28,29]. While most room-temperature experiments rely on a variation of the distance between objects to observe the expected force-distance scaling[3,4,11,12,30], it is challenging to perform this type of experiment with superconductors due to the difficulty of precise positioning in cryogenic environments. By contrast, the strong nonlinearity imparted by the Casimir potential can be easily shown through the dynamical behavior of an oscillator without relying on precise positioners. Only few works have studied the Casimir force through the nonlinear dynamics[31,32].

Strong nonlinearities in oscillators at cryogenic temperatures are especially interesting in the context of resonators in the quantum regime. Cavity optomechanics, where the motion of an object couples to the electromagnetic field of a cavity, has allowed to engineer Gaussian quantum mechanical states in cryogenic mechanical oscillators. Notably, resonators were cooled to the ground state[33], their uncertainty was squeezed below the magnitude of quantum fluctuations[34–36], entangled states of two oscillators were prepared[37,38], and mechanical states were measured avoiding quantum backaction[39]. However, linear optomechanical systems cannot realize non-Gaussian quantum states such as Fock states, cat states, and entangled combinations thereof, which are desirable for quantum algorithms. To realize these states nonetheless, mechanical oscillators have been addressed with non-Gaussian photonic states[40,41], or coupled to superconducting qubits[42–45] or quantum dots[46] to inherit their nonlinearity. In contrast, the nonlinearity imparted by the Casimir force to a superconducting drum resonator is intrinsic to the construction of the system and does not rely on coupling to another system.

In this work, we have observed a nonlinear potential that we show to be quantitatively compatible with the Casimir potential acting between the plates of a type-I superconducting drum. This force force yields a strong softening nonlinearity, where the resonating frequency decreases with increasing amplitude[9,31,32]. The optomechanical coupling to a microwave cavity allows us to calibrate all properties of the system and compare its response to that obtained within a model of Casimir potential with only a single fit parameter. We qualitatively and quantitatively exclude other (nonlinear) effects that have hindered earlier works[26,30,47]. This system requires no cryogenic positioners, and it shows a strong, tunable mechanical nonlinearity that is fully compatible with a mechanical system where quantum operations have been achieved.

RESULTS

The Casimir nonlinearity

Here, we detail the experimental system: for clarity, we already present here conclusions and interpretations whose determination is explained further below. The drum resonator consists of two plates made of evaporated aluminium. The top plate is suspended and forms a harmonic oscillator: the minimum of the harmonic mechanical potential would corre-

* laure.mercierdelepinay@aalto.fi

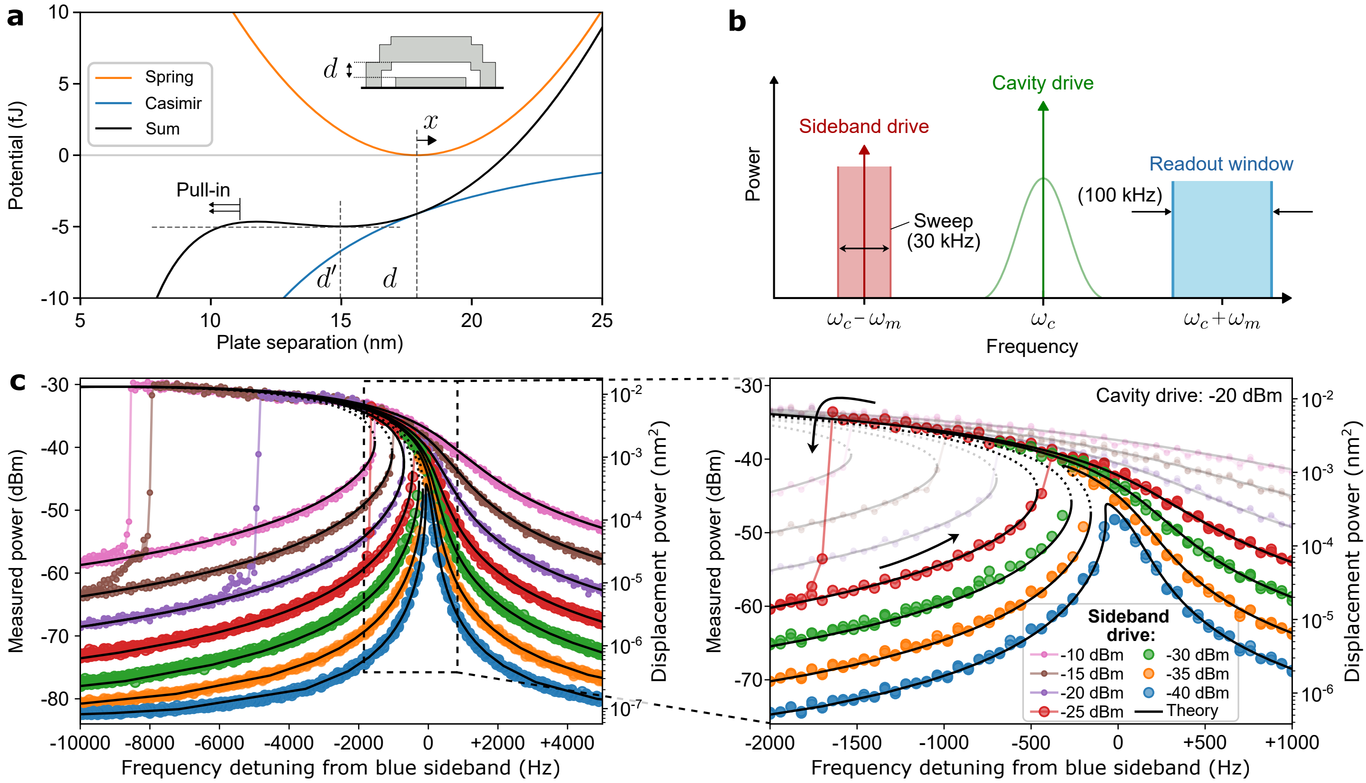

Fig. 1 | Effects of a Casimir force on a superconducting drum resonator. **a**: Our device consists of two plates separated by a vacuum gap. The top plate is mechanically compliant and experiences a mechanical restoring potential (orange line) which is minimum for a separation d between plates (see inset). The Casimir potential (blue) adds to this restoring potential, and the sum (black) has a local minimum at separation d' shifted from d. The total potential is not harmonic around d' for large amplitudes which causes nonlinear behavior. **b**: Schematic of the microwave optomechanical measurement scheme. We strongly drive the microwave cavity at its center frequency, with an additional strong drive tone at ω_{sb} which is close to $\omega_{\mathrm{c}} - \omega_{\mathrm{m}}$. The sideband drive is swept in frequency, and we read out the emitted signal in a window around $\omega_{\mathrm{c}} + \omega_{\mathrm{m}}$. **c**: Measured displacement response for various nominal sideband drive powers (labels) at −20 dBm cavity drive, showing the expected Lorentzian behavior at low drive power that transitions to a strong softening nonlinearity at high drive power. The Casimir force solution (black line) becomes multi-valued, with two stable branches (solid black) and an unstable solution (dotted black/semitransparent). Our measurements follow the stable solutions, leading to a hysteresis depending on the sweep direction. The theory matches well to all curves using only a single fit parameter, d, common to all curves. The right panel highlights details of the center region indicated by the dashed box, and the hysteresis depending on the sweep direction is indicated by arrows. The data points at the highest powers are made transparent for visual clarity.

spond to a vacuum gap of $d = 18.00 \pm 0.25$ nm at cryogenic temperatures. This very narrow vacuum gap implies a strong Casimir effect, so the Casimir force draws the mechanically compliant top plate closer to the bottom plate that is fixed to a rigid substrate. The shift of the rest position of the top plate is significant: The equilibrium position with the Casimir force taken into account – which is the real physical situation – corresponds to a vacuum gap $d' = d - 2.9$ nm $= 15.1$ nm, which we schematically show in Fig. **1a**. These gaps are not known a priori: the method of their determination is explained further below. Without the Casimir effect, the top plate would oscillate with unperturbed frequency ω_{r} (see Table **1**) around the minimum of elastic potential energy at a distance d from the bottom plate's top surface. But due to the Casimir force, it oscillates with frequency ω_{m} around the local minimum of the total potential at separation d' (the equilibrium position). It can stably oscillate around this local minimum with a small amplitude, but at larger amplitudes the frequency decreases (spring softening) until it reaches the pull-in point, beyond which the top plate will collapse onto the bottom plate[8,27]. As explained further below, a model for the dynamics of the oscillator in presence of the Casimir force is

$$\ddot{x} + \gamma_{\mathrm{r}}\dot{x} + \omega_{\mathrm{r}}^2 x + \frac{P}{(x+d)^n}\frac{\pi r^2}{m_{\mathrm{eff}}} = \frac{F_0}{m_{\mathrm{eff}}}, \tag{1}$$

which describes the evolution of a point-like harmonic oscillator in one dimension with displacement coordinate x, resonance frequency ω_{r}, effective mass m_{eff}, and decay rate γ_{r} driven by a force F_0. We note that this model reducing the distributed motion of the membrane to a scalar coordinate with an effective mass stays roughly valid in presence of a nonlinear potential. It is additionally subject to a force derived from the Casimir pressure, the last term on the left-hand side, that works on the area of the drum, πr^2. We compute the Casimir pressure for the real material based on the Mattis-Bardeen conductivity for (BCS) superconductors[28], see Meth-

Quantity	Symbol	Value
Unperturbed frequency	ω_r	$2\pi \times 16.247$ MHz
Mechanical frequency	ω_m	$2\pi \times 10.001$ MHz
Mechanical linewidth	$\gamma_r \simeq \gamma_m$	$2\pi \times 168.9 \pm 9.5$ Hz
Cavity frequency	ω_c	$2\pi \times 5.461831$ GHz
External linewidth	κ_e	$2\pi \times 250.8 \pm 2.1$ kHz
Internal linewidth	κ_i	$2\pi \times 297.2 \pm 2.8$ kHz
Drive frequency	ω_{mw}	$\simeq \omega_c$
Sideband frequency	ω_{sb}	$\simeq \omega_{mw} - \omega_m$
Detuning $\omega_c - \omega_{mw}$	Δ	$< \lvert 2\pi \times 1 \rvert$ kHz
Optomechanical coupling	g_0	$2\pi \times 150 \pm 9$ Hz
Effective mass	m_{eff}	3.96×10^{-14} kg
Rest separation without Cas. f.	d	18.00 ± 0.25 nm
Rest separation	d'	15.10 ± 0.25 nm
Bottom plate diameter	$2r$	11.3 µm
Moving plate diameter	-	14.5 µm
Casimir pressure at equilibrium	P_c	12.0 ± 0.6 kPa
Casimir amplitude	P	$(1275 \pm 7) \cdot 10^{-24}$ Pa m^n
Casimir force scaling exponent	n	3.193

Table 1 | The parameters of our system. The parameters are either fitted (with 95% confidence interval) and from theory or design.

ods. From these computation, the Casimir force would have an expression of the form $P_c = \frac{P}{(x+d)^n}$ where $P \simeq 1275 \cdot 10^{-24}$ Pa $\cdot$ m^n and pressure-distance scaling $n = 3.193$. Within this model, the Casimir pressure experienced by the drum at its equilibrium position $d' = 15.10 \pm 0.25$ nm (corresponding to the value $x \simeq -2.9$ nm) would be $P_c \simeq 12.0 \pm 0.6$ kPa.

The drum resonator is mounted in a dilution cryostat and stabilized at 10 mK (see Methods), so the aluminium is deep in the superconducting regime. The drum forms the variable capacitance of a microwave cavity, which we drive with two strong drives, one at the resonance frequency of the microwave cavity, ω_c (cavity drive), and the other at the red sideband $\omega_c - \omega_m$ (sideband drive) as shown schematically in Fig. **1b**. This combination of tones generates a driving force on the mechanical resonator such that the mechanical amplitude scales linearly with either drive power (see Supplementary Sec. A). All drive powers are reported as their nominal values at room temperature, they are divided by attenuators before reaching the sample as shown in Methods. The cavity drive power is much larger than the sideband drive, and we sweep the frequency of the weaker sideband drive within a range of 30 kHz both upwards and downwards in frequency. We record the output signal of the cavity with a spectrum analyzer over a window centered around $\omega_c + \omega_m$ (blue sideband).

The signal we observe at the readout sideband is proportional to the displacement of the resonator. At low drive powers, we see a Lorentzian response, but increasing the cavity drive power in Fig. **1c** shows the strong softening nonlinearity expected of the Casimir force[9]. At high drive powers, this nonlinearity creates two stable solutions to Eq. (1) over a limited range of frequencies (a low-amplitude and a high-amplitude branch) with an unstable solution in between. The sweep direction determines which branch is followed as indicated by arrows in Fig. **1c**. The resonator amplitude jumps up at the end of the low-amplitude branch (bifurcation point), but it jumps down from the high-amplitude branch at a point before the end of the branch. This occurs due to our stepped sweep protocol (see Methods).

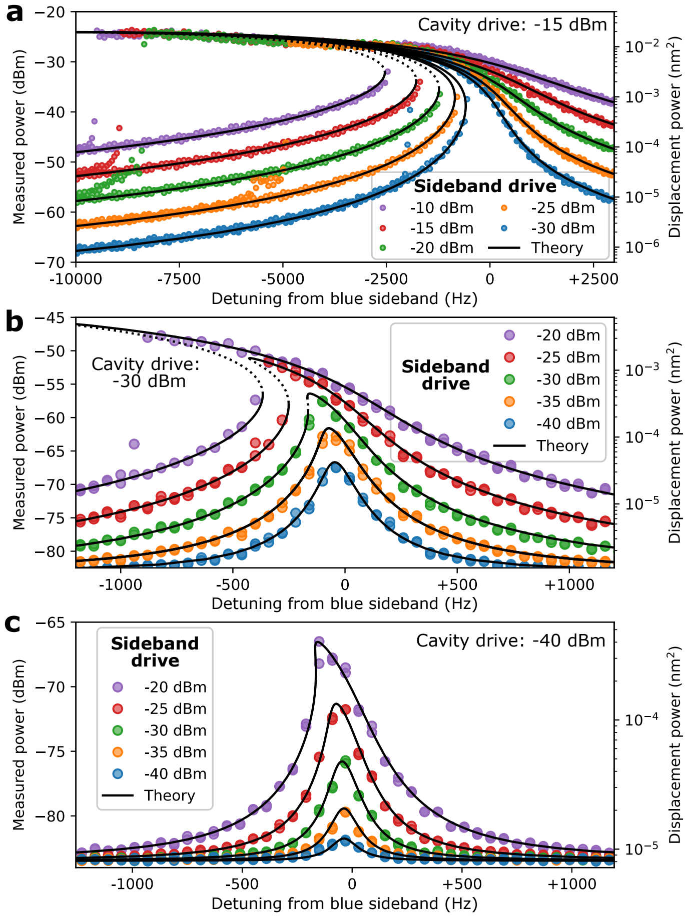

Fig. 2 | Responses measured for all combinations of drive parameters for cavity drive powers (**a**: −15 dBm, **b**: −30 dBm, **c**: −40 dBm) and sideband drive powers (colors). All theory curves (black lines) across all panels share only a single fit parameter d.

We compute the expected displacement of the oscillator of Eq. (1) for a frequency-swept drive (see Methods and Supplementary Information) using the parameters of Table **1**. The resulting curves are plotted as black lines in Fig. **1c**, with the unstable part of the solution as a dotted line. All curves collectively fitted with a single fit parameter d whose value is found to be 18.0 nm show excellent agreement with the measured signal. We repeat the experiment at different combinations of cavity and sideband drive powers, shown in Fig. **2**. Our theory model accurately describes the shape of the signal across more than three orders of magnitude in displacement, up to a maximum measured amplitude of $\simeq 100$ pm. This provides strong indication of a successful measurement of the Casimir force between superconducting plates.

Calibration of displacement amplitude

To make d (the vacuum gap at the minimum of the harmonic mechanical potential) the only fit parameter, we cali-

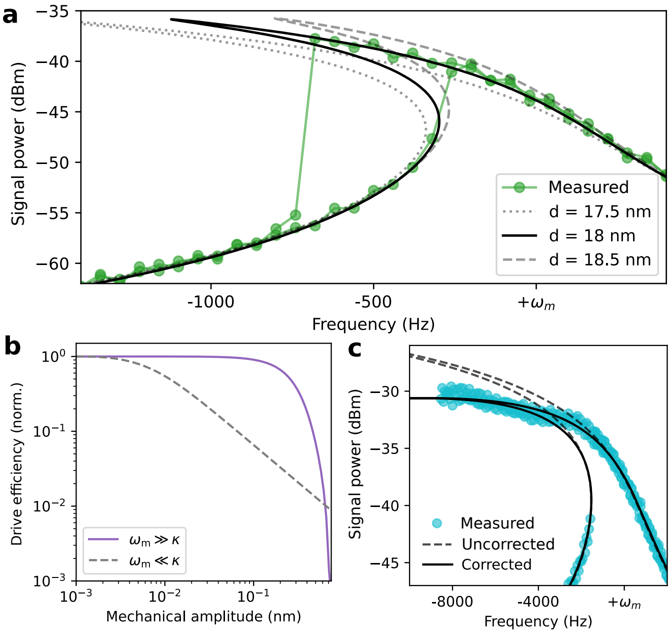

Fig. 3 | Optomechanical calibration. **a**: Theory curves generated with equal maximum mechanical amplitude for various values of d (black & grey lines). For smaller d, the Casimir force is stronger and leads to a larger softening nonlinearity. For d = 18 nm there is excellent agreement with the measured data (green). **b**: The drive efficiency decreases sharply from 1 at high amplitude, as most of the time the instantaneous cavity frequency $\omega_c(t)$ is far away from the drive frequency. This effect is stronger, comparatively, in the bad cavity limit ($\omega_m \ll \kappa$), but it is noticeable in our experiments at the largest amplitudes. **c**: The drive efficiency leads to a correction in the Casimir curves at large amplitudes.

brate all other parameters listed in Table **1** to accurately infer the displacement amplitude of the resonator. The drum resonator is embedded in an optomechanical cavity such that its position couples to the radiation pressure, resulting in the equations of motion[48],

$$\begin{aligned}\dot{\hat{x}}(t) &= \omega_m \hat{p},\\ \dot{\hat{p}}(t) &= -\omega_m \hat{x} - \gamma_m \hat{p} - g_0 \hat{a}^\dagger \hat{a} + \sqrt{\gamma_m}\hat{\xi}(t), \\ \dot{\hat{a}}(t) &= -(i\Delta + \kappa/2)\hat{a} + i g_0 \hat{x}\hat{a} + \sqrt{\kappa_e}\hat{s}_{in}(t) + \sqrt{\kappa}\hat{a}_{noise}(t).\end{aligned} \tag{2}$$

Here, we use operators $\hat{x}$ and $\hat{p}$ for position and momentum, and $\hat{a}$ for the cavity field. We work in a frame rotating at the frequency of the cavity drive, which is detuned by Δ from the cavity resonance frequency. The cavity linewidth $\kappa = \kappa_e + \kappa_i$ is the sum of the external and internal decay rates (see Table **1**). The optomechanical single-photon coupling is g_0. Bath operators for the mechanical noise $\hat{\xi}(t)$ and cavity noise $\hat{a}_{noise}$, and an operator for the input signal $\hat{s}_{in}$ complete the standard dispersive single-mode optomechanical system.

The equations of motion, Eq. (2), depend on parameters ω_m, γ_m, g_0, κ, and Δ. We calibrate cavity parameters κ_e and κ_i from the microwave response, and get the single-photon coupling g_0 and the power at our detector from a given displacement power from the amplitude of thermal motion of the drum resonator at 10 mK (see the Supplementary Information). With the calibrated optomechanical parameters, we obtain the large-amplitude classical response from Eq. (2) for all combinations of power in the cavity drive and red sideband drive. We compare the predicted relative powers in two sidebands (red and blue), and the off-resonant (directly reflected) red sideband drive with our experimentally observed powers. The relative powers in the sidebands are unaffected by attenuation or amplification on the input and output lines. We get excellent agreement for all combinations of drive powers using the calibrated optomechanical parameters, as shown in the Supplementary Information. The value of the drive force F_0 in the model of Eq. (1) is then inferred as the value that generates the experimentally measured displacement.

Parameters P and n are related to material parameters for Aluminium for which we can obtain a high accuracy (see Methods). This makes d the sole fit parameter to compare the solution of Eq. (2) to our experimental observations. In Fig. **3a**, we show that d = 18 nm generates the best-fitting solution. Also solutions with d = 17.5, 18, and 18.5 nm are overlaid on experimental data obtained at −20 dBm cavity drive and −30 dBm sideband drive. The fit procedure is applied to all measured response signals (see Fig. **2**). From this collective fit, we estimate the uncertainty of d as the upper bound of the uncertainty propagated from the amplitude calibration and the standard error of the fitted response signal. The uncertainty we find this way is larger than the uncertainty in d we would have found from variations in parameters P and n, which motivates our choice to treat them as fixed values.

Drive efficiency

At the core of Eq. (2) is the notion that the cavity frequency depends on the mechanical position, $\omega_c(x)$. For a large enough displacement amplitude x, the cavity frequency shifts by more than the cavity linewidth κ such that the cavity drive tone is mostly reflected. This reduces the amount of circulating power in the cavity, and it reduces the effectiveness of the drive on the mechanical resonator. We estimate this loss of efficiency and compensate for it in the following way. We define the 'drive efficiency' as the circulating power in the cavity at some mechanical amplitude normalized to the power at low displacement. It is straightforward to calculate by solving Eq. (2) for fixed amplitude of mechanical motion, and the results are plotted in Fig. **3b**. In the experiment $\omega_m \gg \kappa$ so the drive efficiency is close to 1 up to ~ 100 pm and strongly decreases beyond that.

The effect of the drive efficiency on our Casimir theory is shown in Fig. **3c**. For the frequencies where the mechanical amplitude is small, the uncorrected and corrected curves overlap since the drive efficiency is 1. At large amplitudes the uncorrected prediction overestimates the measured response (−20 dBm cavity drive and −10 dBm sideband drive). The correction from the drive efficiency also gives a sanity check on the amplitude calibration, since it originates completely from Eq. (2), which is independent of the Casimir effect.

The optomechanical nonlinearity

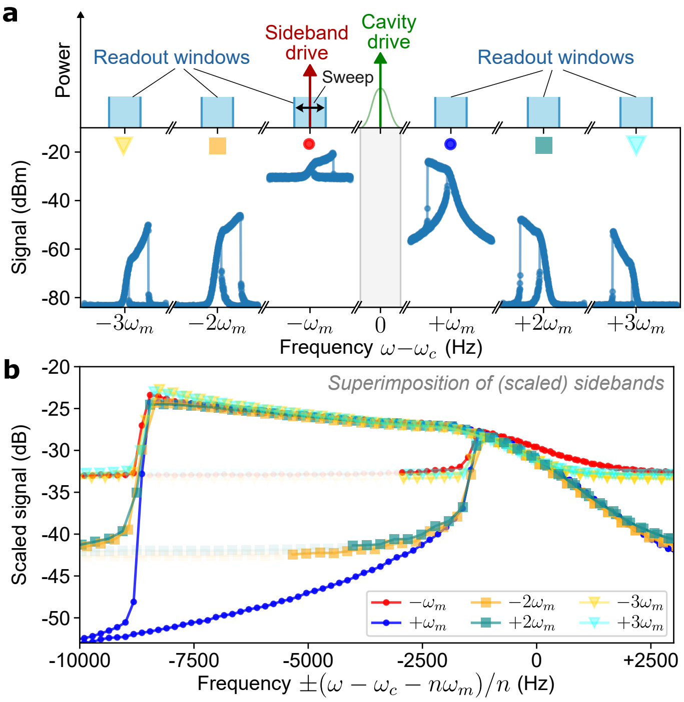

Fig. 4 | Response observed at higher-order sidebands. **a**: The full optomechanical measurement consists of six sidebands that are read out sequentially. The first red sideband ($-\omega_m$) is at the same frequency as our swept sideband drive, so its signal is superposed on a pedestal from the directly reflected sideband drive signal. **b**: Superimposition of sidebands. All sidebands encode the mechanical displacement with a known proportionality (see main text), so they collapse on top one another when overlaid. The frequency axis of each sideband has been shifted to align the sideband frequencies $\omega_c + n\omega_m$, and the frequency axis of the red sidebands (below the cavity frequency) has been flipped about the sideband frequency. Furthermore the frequency range has been divided by two for second sidebands and three for third sidebands. The vertical axis of 2nd and 3rd order sidebands has been squared and cubed respectively, as expected from theory.

The optomechanical interaction, Eq. (2), is nonlinear. As a result, at large amplitude the higher-order scattering terms yield multiple equally-spaced peaks in the observed response. We read out six of these sidebands, at $\omega_c \pm n \times \omega_m$ (n = 1, 2, 3), as shown in Fig. 4a. The higher-order sidebands can be viewed as repeated scattering events. We extend classical scattered mode theory[49] to cover all six sidebands. We write the system of linear coupled equations for the classical field amplitudes a_n at the corresponding frequency components in matrix form,

$$\begin{bmatrix} 1 & d_{+3} & 0 & 0 & 0 & 0 & 0 \\ d_{+2} & 1 & d_{+2} & 0 & 0 & 0 & 0 \\ 0 & d_{+1} & 1 & d_{+1} & 0 & 0 & 0 \\ 0 & 0 & d_0 & 1 & d_0 & 0 & 0 \\ 0 & 0 & 0 & d_{-1} & 1 & d_{-1} & 0 \\ 0 & 0 & 0 & 0 & d_{-2} & 1 & d_{-2} \\ 0 & 0 & 0 & 0 & 0 & d_{-3} & 1 \end{bmatrix} \begin{bmatrix} a_{+3} \\ a_{+2} \\ a_{+1} \\ a_0 \\ a_{-1} \\ a_{-2} \\ a_{-3} \end{bmatrix} = \begin{bmatrix} 0 \\ 0 \\ 0 \\ \frac{a_{\mathrm{mw}}\sqrt{\kappa_e}}{-i\Delta+\kappa/2} \\ 0 \\ 0 \\ 0 \end{bmatrix} \quad (3)$$

with

$$d_{\pm n} = \frac{g_0 x_{\mathrm{amp}}}{2x_{\mathrm{zpf}}} \frac{1}{-i(\Delta \pm n\omega_{\mathrm{m}}) + \kappa/2}. \quad (4)$$

Here a_{mw} is the input power of the microwave drive at the cavity frequency, a_{sb} is the input power of the microwave drive at the red sideband. We cut off the scattering processes above order $|n| = 3$, retaining 7 frequency ranges in Eq. (3). This is a valid approximation when $g_0 \ll \kappa/2$, since each individual photon is much more likely to exit the cavity than to scatter from the mechanical resonator. For more details, see the Supplementary Information. The power in the first-order sidebands ($\pm\omega_{\mathrm{m}}$) scales linearly with the amplitude of mechanical displacement x_{amp}, while the second order sidebands ($\pm 2\omega_{\mathrm{m}}$) scale quadratically and the third order sidebands ($\pm 3\omega_{\mathrm{m}}$) scale cubically. The span of the sweep is doubled and tripled for the second and third mode. When we combine these known behaviors and flip the frequency of the $-1, -2, -3 \times \omega_{\mathrm{m}}$ sidebands, we can perfectly overlay all sidebands in the high-amplitude regime (Fig. **4b**). This shows that although the higher-order peaks arise from a nonlinear optomechanical effect, the profile of the response is unaffected by the optomechanical nonlinearity. Thus, even at large mechanical amplitudes the cavity output signal gives an accurate account of the mechanical displacement.

DISCUSSION

There are many other effects that could result in an apparent nonlinearity, such as the electrostatic force between the drum plates, potential patches in the aluminium, the geometric nonlinearity, the nonlinear optomechanical coupling, and superconducting vortices. We can rule out these effects as an alternative explanation for our observations, as described in detail in the Supplementary Information. Put briefly, we estimate the pressure contributed by e.g., potential patches, based on Kelvin probe force measurements of the electrostatic potential. We simulate the effect of patches in our geometry[50], and find that the patch pressure is several orders of magnitude smaller than the Casimir pressure at our plate separation. Based on this, we rule out the effect of potential patches (and similar for the other effects described in the Supplementary Information). To the best of our knowledge, there are no other sources of nonlinearity that could mimic the Casimir force in both amplitude and scaling.

Our future experiments will involve a gate electrode patterned around the drum plate to allow electrostatic tuning of the separation[30] and, by extension, the Casimir force. A modest 100 Pa electrostatic pressure is achievable, and sufficient to merge the locally stable solution used in this work with the pull-in point. This should allow the Casimir effect to create nonlinear mechanics on the single-phonon level, a long-standing goal previously only achieved by coupling to external systems[45,46]. The gate electrode will also allow us to improve the accuracy of the amplitude calibration to improve our bounds on d and P_c, to shed light on the Casimir puzzle[19] of materials with finite conductivity.

In summary, we have shown the effect of a likely Casimir force between superconducting plates, through its nonlinear nature. We developed a calibration method to translate the power spectrum of a multi-frequency microwave signal into a mechanical amplitude, which leads to an estimate of the Casimir force. With this method we find excellent agreement between our experiment and the computed Casimir force, across three orders of magnitude of mechanical displacement. Due to the exceptionally small spacing, a vacuum gap of 15 nm, the Casimir force in this configuration is much larger than in conventional Casimir experiments, including those at room temperature: for comparison, it equals a tenth of the atmospheric pressure. This makes our system well-suited to accurately probe the remaining uncertainties around the Casimir effect. By adding a gate electrode, we could improve the precision of our nonlinear-dynamics-based Casimir measurements beyond the small predicted change at the superconducting transition[28]. More fundamentally, the strength of the Casimir effect in our experimental setup gives unique access to an extremely strong, tuneable nonlinearity that is intrinsic to the mechanical system. This means that we could obtain well-separated mechanical energy levels without resorting to the nonlinearity of another system, i.e., bring the mechanical resonator into quantum regime without interactions with non-Gaussian photon states or coupling to an external nonlinear system. Furthermore, the competition between the Casimir potential and the elastic potential can be tuned electrostatically, in situ, to be locally flat, which could be used to probe macroscopic mechanical quantum tunneling[51] or make a mechanical qubit[45,52].

METHODS

Calculation of the Casimir force

To compute the Casimir force between the superconducting plates of our drum, we follow exactly the method of Bimonte[28]. It is based on the Lifshitz formula[2] for the pressure $P(d,T)$ between two plates as a function of their separation d and temperature T,

$$P(d,T) = \frac{-k_BT}{\pi}\sum_0^{\infty}\int_0^{\infty} dk_\perp k_\perp q_\ell \left(\left[\frac{e^{2dq_\ell}}{r_{\mathrm{TE},1}(i\xi_\ell,k_\perp) r_{\mathrm{TE},2}(i\xi_\ell,k_\perp)} - 1\right]^{-1} + \left[\frac{e^{2dq_\ell}}{r_{\mathrm{TM},1}(i\xi_\ell,k_\perp) r_{\mathrm{TM},2}(i\xi_\ell,k_\perp)} - 1\right]^{-1}\right), \tag{5}$$

where $k_\perp$ is the in-plane momentum, the $\ell = 0$ term in the sum has a weight of one half, $\xi_\ell = 2\pi\ell k_BT/\hbar$ are the imaginary Matsubara frequencies, $q_\ell = \sqrt{\xi_\ell^2/c^2 + k_\perp^2}$, and TE and TM indicate the two independent polarizations of the electromagnetic field. The Fresnel reflection coefficients for the polarizations (TE,TM) and plates (1,2) are[28]

$$\begin{aligned} r_{\mathrm{TE}}(i\xi_\ell,k_\perp) &= \frac{q_\ell - s_\ell}{q_\ell + s_\ell},\\ r_{\mathrm{TM}}(i\xi_\ell,k_\perp) &= \frac{\epsilon_\ell q_\ell - s_\ell}{\epsilon_\ell q_\ell + s_\ell}, \end{aligned} \tag{6}$$

where $s_\ell = \sqrt{\epsilon_\ell \xi_\ell^2/c^2 + k_\perp^2}$ and electric permittivity $\epsilon_\ell = \epsilon(i\xi_\ell)$ for the materials of each of the plates 1 and 2. For normal-state materials, we use the Drude model dielectric function $\epsilon_{\mathrm{Drude}}$. For superconductors, the Mattis-Bardeen fomula gives a corrected function ϵ_{BCS}. The analytic continuation of both functions has been derived as[25,28]

$$\begin{aligned} \epsilon_{\mathrm{Drude}}(i\xi) &= \epsilon_0 + \frac{\Omega_p^2}{\xi(\xi+\gamma_{\mathrm{p}})},\\ \epsilon_{\mathrm{BCS}}(i\xi) &= \epsilon_0 + \frac{\Omega_p^2}{\xi}\left(\frac{1}{\xi+\gamma_{\mathrm{p}}} + \frac{g(\xi,T)}{\xi}\right). \end{aligned} \tag{7}$$

Here, Ω_{p} represents the plasma frequency for intraband transitions, γ_{p} is the relaxation frequency. The contribution from BCS theory is in the form of the factor $g(\xi,T)$, given as[28]

$$g(\xi,T) = \int_{-\infty}^{\infty} \frac{d\epsilon}{E}\tanh\left(\frac{E}{2k_BT}\right)\mathrm{Re}\left[G_+(i\xi,\epsilon)\right]. \tag{8}$$

This expression is valid for temperatures below the superconducting transition temperature, $T < T_{\mathrm{c}}$. The function G_+ is defined as

$$\begin{aligned} G_+(z,\epsilon) &= \frac{\epsilon^2 Q_+(z,E) + \left[Q_+(z,E) + i\hbar\gamma\right]A_+(z,E)}{Q_+(z,E)\left(\epsilon^2 - \left[Q_+(z,E)+i\hbar\gamma\right]\right)},\\ E &= \sqrt{\epsilon^2+\Delta^2},\\ Q_+(z,E) &= \sqrt{(E+\hbar z)^2 - \Delta^2},\\ A_+(z,E) &= E(E+\hbar z) + \Delta^2, \end{aligned} \tag{9}$$

and the superconducting gap $\Delta(T)$ is temperature dependent,

$$\Delta = c_1 k_B T_{\mathrm{c}} \sqrt{1 - \frac{T}{T_{\mathrm{c}}}\left(c_2 + c_3\frac{T}{T_{\mathrm{c}}}\right)}, \tag{10}$$

where we take $c_1 = 1.764$, $c_2 = 0.9963$, and $c_3 = 0.7735$ from BCS theory[53].

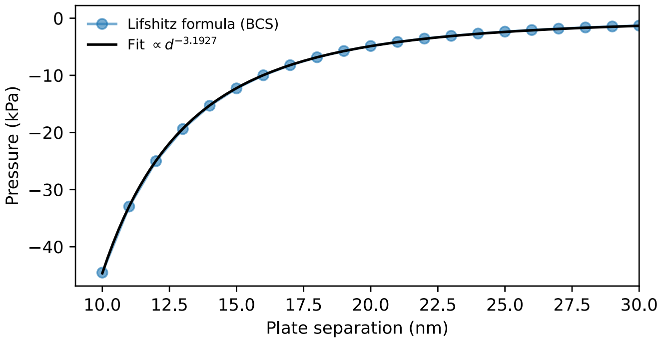

Fig. 5 | The Casimir pressure. The Casimir pressure for various distances as calculated via the Lifshitz formula and the BCS model, and a fit proportional to $d^{-3.193}$.

To evaluate the expression of Eq. (5), we need the material parameters for aluminium, which are tabulated[54]. We use $\Omega_p = 13$ eV$/\hbar$, $\gamma_p = \gamma_0/\mathrm{RRR}$ where RRR $= 2$ denotes the residual resistance ratio of our thin-film aluminium, and $\gamma_0 = 0.1$ eV$/\hbar$ is a phenomenological relaxation rate (dissipation of current). Finally, setting $\epsilon_0 = 1.03$ as the relative permittivity of aluminium takes into account the core interband transitions[54].

To numerically compute the Casimir pressure in a reasonable amount of time, we take the Matsubara frequencies up to $\ell = 200,000$. We determine that this is sufficient by increasing the range of the sum until the final pressure changes by less than 10^{-5} of the value for the previous range. Conversely, to compute the difference between $\epsilon_{\mathrm{Drude}}$ and ϵ_{BCS} it is sufficient to take[28] $\ell \lesssim 600$. Nonetheless, we must also integrate over $k_\perp$. The integrand of Eq. (5) is sharply peaked[25], and heuristic bounds of $\pm 300\sqrt{\xi_\ell \Delta}$ seem to have sufficiently small error.

In Fig. 5, we plot the results of our evaluation of Eq. (5) for our system. While the Casimir pressure scales as $P \propto d^{-4}$ for ideal conductors[1], for real conductors the scaling exponent is different. Using the material parameters for aluminium, the pressure is best described by a fit $P_c = -\frac{1275\pm 7\cdot 10^{-24}}{d^{3.193}}$ Pa, with the 95% confidence intervals extracted from the fit to the calculation results. We have plotted the dependence $P \propto d^{-3.193}$ as a black line in Fig. 5.

Drum design and fabrication

The drum fabrication process starts with a 2-inch quartz wafer. For each patterning step, we spin-coat three resist layers (MMA(8.5)MAA EL7 at 4000 RPM (rotations per minute) for 60 s with a 90 s bake at 150 °C, PMMA 950 A3 at 4000 RPM for 60 s with a 90 s bake at 180 °C, and then Espacer 300Z at 4000 RPM for 60 s with a 60 s bake at 90 °C) and pattern the design by electron beam lithography. Our development recipe is a 30 s bath in a 1:3 mixture of MIBK:IPA, followed by a brief bath and rinse in pure IPA. The first pattern step consists of markers for alignment, so we evaporate 5 nm Ti and 40 nm Au. Then we perform lift-off using a hot acetone bath ($\simeq 55$ °C for 20 minutes followed by 2 minutes in a sonicator bath).

The bottom layer pattern consists of the microwave cavity, bonding pads, waveguides and the bottom plate of the drum resonator. We evaporate a 40 nm Al layer in an electron beam evaporator, and realise the liftoff as described before. Then, we grow a 80 nm layer of amorphous silicon (α-Si) by PECVD, which forms the sacrificial layer between the drum plates. This layer is patterned with a single layer of PMMA 950 A9, and etched by reactive ion etching using a mixture of SF_6/O_2.

The top layer consists only of the top drum plate. We evaporate a 120 nm Al layer after patterning. Until now, all steps have been performed on a full 2-inch wafer, but after the final Al evaporation we dice the chips to their final 4×4 mm^2 size. We perform a heat treatment (15 minutes on a hot plate set to between 240 and 280 °C) to redistribute the stress in the top-layer Al and ensure the drums are flat (i.e., not bulging upwards). The final step is the release etch, where we etch the α-Si sacrificial layer away with a reactive ion etch mixture of SF_6/O_2 and get a drum resonator with a suspended top layer.

Measurement setup

Our setup consists of a sample mounted on the base plate of a Bluefors dilution refrigerator, as schematically shown in Fig. 6. To drive our sample, we source the drive a_{mw} at the cavity frequency from a microwave generator, and the drive at the red sideband, a_{sb}, from a vector network analyzer. The drive a_{sb} is attenuated by a directional coupler that merges it to the main drive a_{mw}. Both drives make their way through a suitably attenuated input line to the sample at the base plate of the refrigerator.

The sample is measured in reflection, and the reflected signal is routed through a stack of two circulators and a band-pass filter. A copy of a_{mw} split off from the same source is used to interferometrically cancel the drive component reflected from the sample. This is done to avoid saturating the cryogenic amplifier. The cancellation line has a tunable phase delay and attenuation, which we manually set to maximally cancel the output before starting any measurement. On the output line from the sample, after the directional coupler, there is a low-temperature low-noise amplifier, followed by another amplifier at room temperature. Finally, half of the signal is sent back to the network analyzer for measurement, while the other half is routed through a third amplifier to the spectrum analyzer.

Our measurement protocol starts by generating a set of frequencies around the sideband that we will drive. This gives us control over the direction of the frequency sweep. The cavity drive is turned on, then the sideband drive is initialized to the first frequency. We record the signal on the spectrum analyzer while the sideband frequency is swept. We repeat this sequentially for each of the six readout windows, then reverse the frequency sweep direction, and repeat it again for all six readout windows. This stepped protocol means that the sideband drive is briefly turned off to switch to the next frequency,

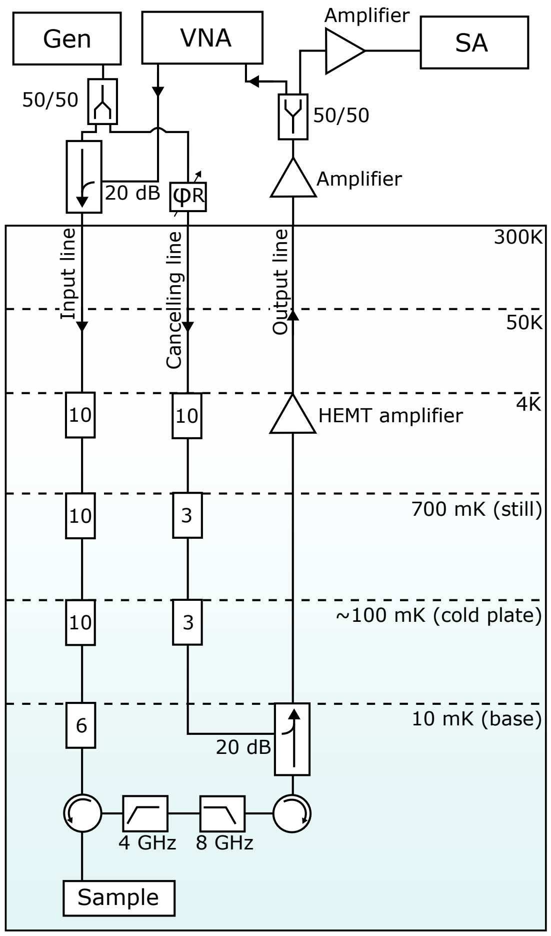

Fig. 6 | Setup. Schematic of the setup used in the experiments. The two drives a_{mw} and a_{sb} are sourced from a microwave generator (Gen) and a vector network analyzer (VNA) respectively. The output signal is split between the vector network analyzer and a spectrum analyzer (SA). The attenuator values are given in dB.

which can cause the oscillator to decay to the low-amplitude branch. The point on the high-amplitude branch at which this happens is not random, it is reproducible between measurements, as evidenced by the overlap of the curves in Fig. **4b**. The stepped drive frequencies do not overlap perfectly with the frequency bins of the spectrum analyzer, and we apply a data filtering scheme detailed in the Supplementary Information.

Drum frequency and effective mass

The released drums are measured in an atomic force microscope (AFM) to estimate the gap at room temperature. In Fig. **7** the device measured in this work is shown. By comparing the heights at various points on the geometry of the drum, we can estimate the layer thicknesses and gap size. The connector to the right in Fig. **7** is deposited in the first evaporation step, so it provides a height reference for the bottom plate of the drum (purple dotted linecut). The top layer shows three distinct heights (along the pink dotted linecut): In the drum center the total thickness is contributed by the thickness of the bottom aluminium plate, the thickness of the sacrificial α-Si layer, and the thickness of the top layer. Closer to the drum edge, the bottom plate stops and only the α-Si layer and the top layer thicknesses contribute. At the edge of the drum, the top plate contacts the substrate and accounts for the whole thickness. Finally, beyond the drum we measure only the substrate, although the exposed substrate is etched by $\simeq$120 nm in the drum release step.

We smooth the measurement of the top drum layer and extrapolate it using the known layer thickness to calculate the average gap. The extrapolated gap is shown by dashed black lines in Fig. **7**, and it is approximately 100 nm. There is a slight concavity in the middle of the drum of 15 nm. This can be explained by a small tensile stress that remains in the aluminium layer due to fabrication. We model the geometry of the drum in COMSOL and show a cut plane through the center of the drum in Fig. **8a**. At room temperature, a 15 MPa tensile stress in the aluminium domain yields a 15 nm concavity that matches the AFM measurement.

When the drum is cooled down, the materials thermally contract, but the contraction of the aluminium is much stronger than that of the quartz. To estimate the relative contractions, we use the temperature dependent material parameters included in COMSOL's basic library, for thin-film aluminium and c-axis quartz (corresponding to our z-cut wafers). We extrapolate the dilation coefficient of quartz below 73 K based on literature values[55]. As a result of the larger relative contraction of the aluminium drum with respect to its substrate, it is subject to an increased tensile stress upon cooling it down to 10 mK. The side walls of the drum unfold and the membrane is brought downwards, which has been previously noted by other groups working with drum resonators[30]. The gap is reduced from 100 nm to 18 nm. Note that this estimate of the drum's separation $d = 18$ nm (unperturbed by the Casimir force) is found from an entirely independent estimation method from the value of the same parameter $d = 18.00 \pm 0.25$ nm found by fitting experimental data. While we consider that this simulation method to estimate d is much less reliable than the fit to experimental data, the fact that these methods independently yield the same value gives confidence in this estimate.

The shape of the fundamental drum mode (Fig. **8b**) is negligibly affected by the thermal contraction, but the frequency of the mode is simulated to vary from 5.4 MHz at room temperature to 16.2 MHz at 10 mK. This frequency is the 'unperturbed' frequency in Table **1** that we use as input for the Casimir oscillator simulations.

The mechanical mode shape $\mathbf{u}(\mathbf{r})$ computed using COMSOL is shown in Fig. **8b**. Here, the displacement detection and actuation profiles coincide and are commonly denoted $\mathbf{w}(\mathbf{r})$. In this case the effective mass is computed as[56]

$$m_{\mathrm{eff}} = m \frac{\int_V \|\mathbf{u}(\mathbf{r})\|^2 \, d^3\mathbf{r}/V}{\left(\int_V \mathbf{w}(\mathbf{r}) \cdot \mathbf{u}(\mathbf{r}) \, d^3\mathbf{r}/V\right)^2}, \tag{11}$$

where m is the physical mass, V is the volume of the oscillator.

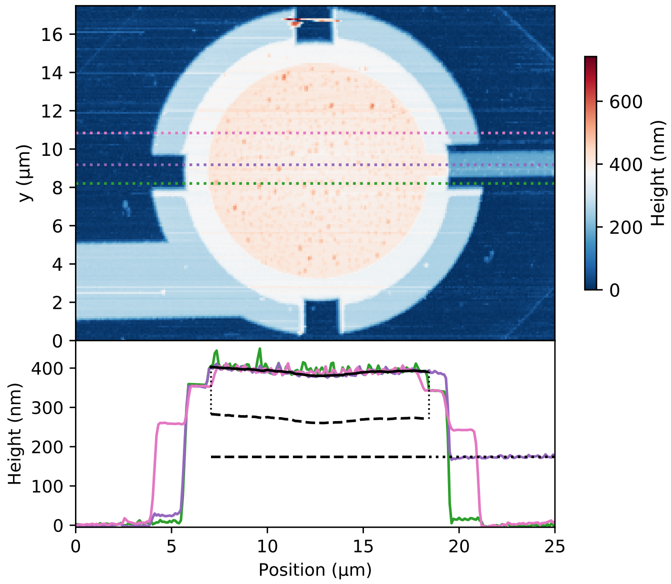

Fig. 7 | AFM measurement of the superconducting drum. The room-temperature gap between the superconducting plates can be estimated from an AFM measurement by comparing the heights along different linecuts (colored dotted lines). The purple line provides a height reference for the bottom plate via the exposed connector on the right side; the green line provides a height reference for the (etched) substrate and the pink line provides a height reference to the thickness of the top layer. We extrapolate the gap (dashed black lines) by subtracting the top layer thickness, 120 nm from the smoothed top linecut. There is a slight concavity of the suspended part, approximately 15 nm on an average gap of 100 nm.

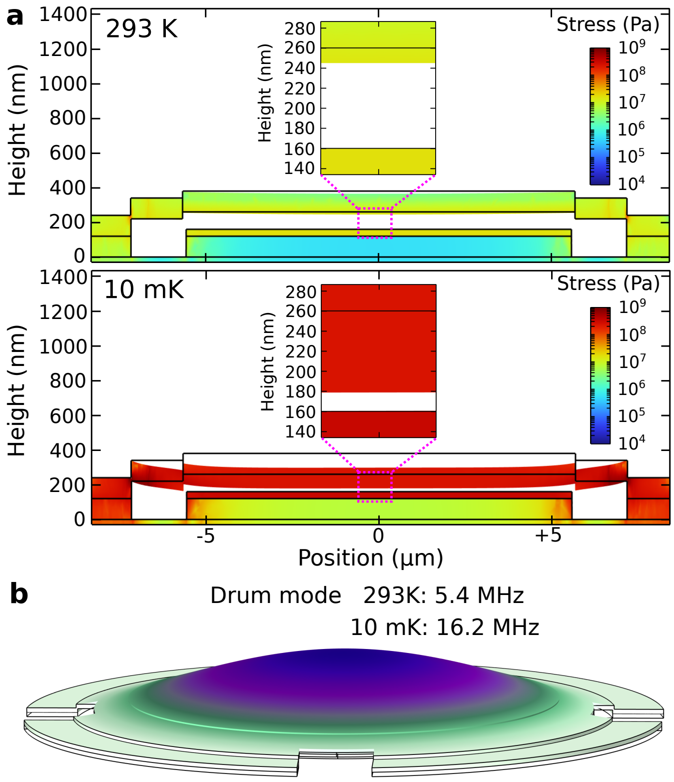

Fig. 8 | Simulated drum mechanics. a: A plane cut through the center of the simulated drum geometry shows a 15 nm concavity if a 15 MPa tensile pre-stress is included in the aluminium domain. By cooling down to 10 mK, the aluminium contracts more than the quartz substrate, which greatly increases the tensile stress in the drum. Under this tensile stress, the torque applied on the edges of the drum brings it downwards which reduces the vacuum gap from 100 nm to very low values consistent with the experimentally determined 18 nm according to simulations. **b**: Simulated mode shape and frequencies of the drum. The fundamental drum mode greatly increases in frequency due to the added tensile stress.

The amplitude given to $\mathbf{u}(\mathbf{r})$ for the computation is irrelevant. In a good approximation, the actuation/detection profile $\mathbf{w}(\mathbf{r})$ is assumed to be oriented along z-axis, and to be homogeneous across the bottom plate. The physical mass is calculated to be $m = 5.4 \cdot 10^{-14}$ kg and the effective mass $m_{\mathrm{eff}} = 3.9 \cdot 10^{-14}$ kg.

The Casimir oscillator

In Eq. (1) we have added a strongly nonlinear term to the equation of motion of a harmonic oscillator. It is typical to perform a Taylor expansion of this term for small motions and truncate the resulting series[9,32], but that approximation fails to describe the higher-amplitude motion seen in our measurements. Instead, we use a the MATLAB-based continuation library MatCont[57,58] for our numerical computations, which can handle Eq. (1) without approximations. This toolbox employs different methods for an extensive study of nonlinear dynamics of a system, such as tracking equilibrium points, detecting bifurcations, and continuing branches of periodic solutions. The continuation method involves two steps: iterative prediction of a point on the solution curve and correction of the predicted point through a Newton-like procedure. This procedure is based on linearizing the function at the current guess and finding where the linear approximation intersects with the x-axis, which becomes the next approximation.

For MatCont, the system of equations must be of the first-order and autonomous (no explicit time dependence). The drive term of Eq. (1), $F_0 = F_{\mathrm{d}} \sin(\omega_{\mathrm{d}} t)$, is the only term explicitly dependent on time. We can make it autonomous by using the Hopf normal form which allows us to express the dynamics in terms of two real variables in amplitude-phase form. Hopf normal form in Cartesian coordinates reads

$$\begin{aligned} \dot{u} &= (\mu - x^2 - y^2)x - \omega_{\mathrm{d}} y \\ \dot{v} &= (\mu - x^2 - y^2)y + \omega_{\mathrm{d}} x \end{aligned} \tag{12}$$

Assuming $\mu = 1$, we choose u to substitute the drive term.

We non-dimensionalize and scale Eq. (1), and split it into two first-order equations. We define,

$$x' = \frac{x}{x_0}, \quad t' = \frac{t}{t_0}, \quad \text{and} \quad y = \dot{x} \tag{13}$$

where $x_0 = 10^{-9}$ m and $t_0 = 2\pi/\omega_{\mathrm{r}}$.

Substituting all, our system of equations become:

$$\begin{aligned} \dot{x} &= y, \\ \dot{y} &= -Ay - Bx - C(x+d)^n + Du, \\ \dot{u} &= u(1 - u^2 - v^2) - \Omega u, \\ \dot{v} &= v(1 - u^2 - v^2) + \Omega v, \end{aligned} \tag{14}$$

with $A = t_0\gamma_\mathrm{r}$, $B = t_0^2\omega_\mathrm{r}^2$, and

$$C = \frac{t_0^2 P_\mathrm{c}\pi r^2 d^n}{m_\mathrm{eff}(x_0)^{n+1}}, \quad \text{and} \quad D = \frac{t_0^2 F_\mathrm{d}}{m_\mathrm{eff} x_0}. \tag{15}$$

We apply a periodic forcing to the system by arbitrarily choosing $u = 1$, $v = 0$. First, we perform an extended simulation until the system converges to a limit cycle. The last orbit provides the initial conditions for the continuation simulation. By varying certain parameters such as the drive force amplitude F_d, damping coefficient γ_r, separation distance d and the Casimir exponent n, we study how the system's response is affected.

We have become aware of a recent work studying the Casimir force across a superconducting transition[59].

Data and code availability
All data, simulations, measurement and analysis scripts in this work are available at https://doi.org/10.5281/zenodo.14700381.

Acknowledgments
We would like to acknowledge Gongchang Lin for help with the AFM and Eddy Collin for help with the geometric nonlinearity. We acknowledge the facilities and technical support of Otaniemi research infrastructure for Micro and Nanotechnologies (OtaNano), and the Aalto Scientific Computing team for their support. We also acknowledge the financial support of the Finnish Ministry of Education and Culture through the Quantum Doctoral Education Pilot Program (QDOC VN/3137/2024-OKM-4) and the Research Council of Finland through the Finnish Quantum Flagship project (project number 358877, Aalto University). L.M.d.L. acknowledges funding from the Strategic Research Council at the Academy of Finland (Grant No. 338565).

Author contributions
M.d.J., E.K., L.B., and L.M.d.L. designed, developed, and performed the experiments. L.B. developed and fabricated the device, L.M.d.L, M.d.J. and E.K. developed the theoretical and numerical analysis. L.M.d.L. conceptualized the project and L.M.d.L. and M.A.S oversaw it. All authors contributed to writing and editing the manuscript

Competing interest declaration
The authors declare no competing interests.

SUPPLEMENTARY INFORMATION

This part of the document contains the supplementary information.

A. Optomechanical description

1. Equations of motion

The optomechanical equations of motion for a single mechanical mode coupled to a single cavity mode are[48]:

$$\begin{aligned} \dot{\hat{x}}(t) &= \omega_\mathrm{m}\hat{p}, \\ \dot{\hat{p}}(t) &= -\omega_\mathrm{m}\hat{x} - \gamma_\mathrm{m}\hat{p} - g_0\hat{a}^\dagger\hat{a} + \sqrt{\gamma_\mathrm{m}}\hat{\xi}(t), \\ \dot{\hat{a}}(t) &= -(i\Delta + \kappa/2)\hat{a} + ig_0\hat{x}\hat{a} - \sqrt{\kappa_\mathrm{e}}\hat{s}_\mathrm{in}(t) - \sqrt{\kappa}\hat{a}_\mathrm{noise}(t). \end{aligned} \tag{S1}$$

We use operators $\hat{x}$ and $\hat{p}$ to refer to the position and momentum of the mechanical resonator respectively, and $\hat{a}$ denotes the cavity mode field amplitude. The mechanical parameters ω_m, γ_m, the cavity parameters κ, Δ, and the coupling strength g_0 are the same as in the main text and their values are listed in Table I. Note that we use the mechanical parameters ω_m and γ_m which are the 'dressed' parameters from the Casimir force rather than the 'unperturbed' parameters ω_r and γ_r. We operate in a frame rotating at the frequency of the microwave drive, and have noise terms $\hat{\xi}(t)$ and $\hat{a}_\mathrm{noise}(t)$. Out system is strongly driven, so we can safely neglect the noise terms in the majority of numerical simulations. The input field is a combination of the (strong) drive at the microwave cavity frequency, and a weaker sideband drive. It can be expressed as

$$\hat{s}_\mathrm{in}(t) = \sqrt{P_\mathrm{mw}/\hbar\omega_\mathrm{c}} + \sqrt{P_\mathrm{sb}/\hbar\omega_\mathrm{c}}e^{-i\omega_\mathrm{m}t}. \tag{S2}$$

This is enough to solve the system of equations of motion for some initial conditions $\hat{x}(0)$, $\hat{p}(0)$, and $\hat{a}(0)$. However, to translate the motion of the resonator into the signal we detect, we have to model our detection scheme as well. We use input-output theory to compute the output fields

$$\hat{a}_\mathrm{out} = \sqrt{\kappa_\mathrm{e}}\hat{a} - \hat{s}_\mathrm{in}. \tag{S3}$$

We finally compute the spectrum of the output field that we measure by using the Fourier transform $\mathcal{F}$,

$$S_\mathrm{out}(\omega) = \left|\mathcal{F}\left\{(\hat{a}_\mathrm{out} + \hat{a}_\mathrm{out}^\dagger)/2\right\}\right|^2. \tag{S4}$$

This spectrum $S_\mathrm{out}(\omega)$ is what we record on the spectrum analyzer.

We can independently calibrate the parameters ω_m, γ_m, κ, Δ, and g_0 as reported in Sec. C. We also accurately know the powers of the cavity and sideband drive tones we send in, but between the output of the generators and the cavity are attenuators and cable losses (see Methods). To calibrate the amplitudes of our drives at the cavity entrance, we first make a crude estimation based on the relative sideband powers (next section), and then refine that using the full optomechanical equations of motion (section after that).

2. Relative sideband powers

We have recorded the powers of six sidebands ($\pm\omega_m$, $\pm2\omega_\mathrm{m}$, and $\pm3\omega_\mathrm{m}$) for the measurements reported in the main text. We can compare the relative powers of each of the sidebands, and compare the powers with the sideband drive, to show how our detected signal is proportional to the mechanical displacement. We use the perturbative treatment of the classical coupled mode equations[48,49]. Our starting point is a simplified version of Eqs. (60) and (61) of Ref.[48], where the steady state cavity field amplitude a_0 is defined by the input power of the microwave drive at the cavity frequency, a_mw, and cavity parameters κ_e, Δ and κ.

$$\begin{aligned} a_0 &= a_\mathrm{mw}\frac{\sqrt{\kappa_\mathrm{e}}}{-i\Delta + \kappa/2} \\ a_{+1} &= \frac{g_0 x_\mathrm{amp}}{2x_\mathrm{zpf}}\frac{a_0}{-i(\Delta + \omega_\mathrm{m}) + \kappa/2} \\ a_{-1} &= \frac{g_0 x_\mathrm{amp}}{2x_\mathrm{zpf}}\frac{a_0}{-i(\Delta - \omega_\mathrm{m}) + \kappa/2}. \end{aligned} \tag{S5}$$

Here, the amplitude of the anti-Stokes- and Stokes-scattered sidebands are denoted with a_{+1} and a_{-1} respectively. These exist in the spectrum at $\pm\omega_\mathrm{m}$ away from the frequency of a_0, and they are related to the mechanical amplitude x_amp.

Our six-sideband treatment is based on repeating the treatment of Eq. (S5), but considering $a_{\pm1,2,3}$ as the source term instead of a_0. That is, from a_{+1} we recognize two scattering processes, which end up at a_0 and a_{+2} respectively.

$$\begin{aligned} a_0 &= +\frac{g_0 x_\mathrm{amp}}{2x_\mathrm{zpf}}\frac{a_{+1}}{-i\Delta + \kappa/2} \\ a_{+2} &= \frac{g_0 x_\mathrm{amp}}{2x_\mathrm{zpf}}\frac{a_{+1}}{-i(\Delta + 2\omega_\mathrm{m}) + \kappa/2} \end{aligned} \tag{S6}$$

By repeating this treatment for all orders of sidebands that we measure, we gain a set of linear coupled equations. This resulting system can be written in matrix form as

$$\begin{bmatrix} 1 & d_{+3} & 0 & 0 & 0 & 0 & 0 \\ d_{+2} & 1 & d_{+2} & 0 & 0 & 0 & 0 \\ 0 & d_{+1} & 1 & d_{+1} & 0 & 0 & 0 \\ 0 & 0 & d_0 & 1 & d_0 & 0 & 0 \\ 0 & 0 & 0 & d_{-1} & 1 & d_{-1} & 0 \\ 0 & 0 & 0 & 0 & d_{-2} & 1 & d_{-2} \\ 0 & 0 & 0 & 0 & 0 & d_{-3} & 1 \end{bmatrix}\begin{bmatrix} a_{+3} \\ a_{+2} \\ a_{+1} \\ a_0 \\ a_{-1} \\ a_{-2} \\ a_{-3} \end{bmatrix} = \begin{bmatrix} 0 \\ 0 \\ 0 \\ \frac{a_\mathrm{mw}\sqrt{\kappa_\mathrm{e}}}{-i\Delta+\kappa/2} \\ 0 \\ 0 \\ 0 \end{bmatrix} \tag{S7}$$

with

$$d_{\pm n} = \frac{g_0 x_\mathrm{amp}}{2x_\mathrm{zpf}}\frac{1}{-i(\Delta \pm n\omega_\mathrm{m}) + \kappa/2}. \tag{S8}$$

We have made the simplifying assumption that repeated interactions ending up at lower-order sideband are negligible in power compared to the (original) lower-order sideband power. This is a valid assumption when $g_0 \ll \kappa/2$, since each individual photon is much more likely to exit the cavity than to scatter from the mechanical resonator.

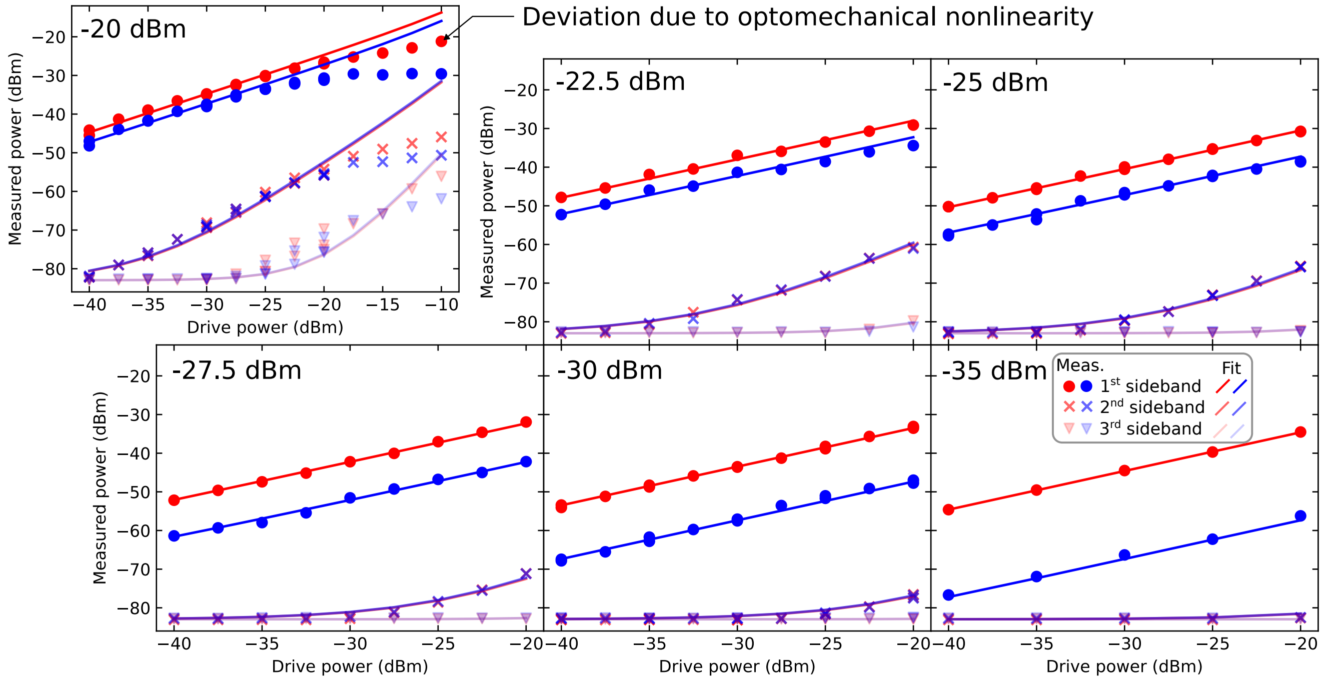

Fig. S1 | Relative sideband powers. Comparison of the maximum powers in all 6 sidebands for different powers of cavity drive $a_{\rm mw}$ (panel labels) and sideband drive $a_{\rm sb}$ (x-axis). The colors indicate whether the sideband is on the red side of the cavity ($a_{-1,-2,-3}$) or on the blue side ($a_{+1,+2,+3}$). The markers are measurements, solid lines are fits to the model of Eq. (S10). Only at the highest powers does our model deviate from the data, which is due to the optomechanical nonlinearity. The asymmetry of the first-order sidebands provides a power reference between the applied drives. The higher order sidebands are symmetric, so they overlap and appear purple in the plot. This symmetry motivates neglecting the scattering processes of $a_{\rm sb}$ which we have done in constructing Eq. (3).

It is fairly straightforward to numerically solve Eq. (S7) using e.g., Python. This model is valid when the optomechanical interaction is dominated by a single drive tone, which in our case is $a_{\rm mw}$. However, we have a weaker second drive, $a_{\rm sb}$, at $-\omega_{\rm m}$. Since it is much weaker than $a_{\rm mw}$, we neglect the effect of any scattering interactions from $a_{\rm sb}$ on the sideband amplitudes. The result of this is that there is an asymmetry only between the first-order red (a_{-1}) and blue (a_{+1}) sidebands. If we had included the scattering interactions of the weaker drive, the red and blue sidebands of all orders would have the same asymmetry. However, from the measurements we will see that this is not the case (only the first order sidebands are asymmetric), and therefore we neglect the scattering interactions of $a_{\rm sb}$ in our sideband amplitude calculation. Thus the resulting amplitude(s) due to this drive are

$$\vec{a}_{\rm sb} = \begin{bmatrix} 0 \\ 0 \\ 0 \\ 0 \\ \frac{a_{\rm sb}\sqrt{\kappa_{\rm e}}}{(-i(\Delta-\omega_{\rm m})+\kappa/2)} \\ 0 \\ 0 \end{bmatrix}. \tag{S9}$$

To fit this model to our data, we solve Eq. (S7) for $\vec{a}$ and compute the output field using the input-output formalism. Here we also add the solution for the weaker drive field $a_{\rm sb}$. The output field is described by

$$a_{\rm out} = \sqrt{\kappa_{\rm e}}(\vec{a}+\vec{a}_{\rm sb}) - \begin{bmatrix} 0 \\ 0 \\ 0 \\ \frac{a_{\rm mw}}{-i\Delta+\kappa/2} \\ \frac{a_{\rm sb}}{-i(\Delta-\omega_{\rm m})+\kappa/2} \\ 0 \\ 0 \end{bmatrix} \tag{S10}$$

In Fig. S1 we have plotted the maximum observed powers of each of our measured sidebands (markers) for different drive powers, and compared those to our fitted model (solid lines). There is an excellent agreement at all but the highest powers. For the highest powers, the optomechanical nonlinearity reduces the drive efficiency, which reduces the maximum powers seen in the sidebands.

The measurements record the sideband powers, and from our model we extract $|a_{\rm out}|^2$, but we need two conversion factors to link the theory to our experiments (one for each axis of Fig. S1). There is also attenuation from the room-temperature source to the cavity at 10 mK (see Methods), which gives us an additional conversion factor. The simplifications of the model of Eq. (S7) are not ideal to use it as an accurate calibration tool between mechanical amplitude and measured power, but it serves as a quick estimation of these conversion factors. We use these as an initial guess for the simulation-based calibration method using the optomechanical equations of motion described in the next section.

3. Absolute amplitude calibration

The optomechanical equations of motion, Eq. (S1), provide us with a method to calibrate the mechanical amplitude, since they do not depend on the distance d or the Casimir parameters, pressure P_c and scaling n. At small amplitudes, our resonator behaves like a harmonic oscillator since the Casimir effect does not perturb small dynamical motion. To calibrate the mechanical amplitude, we need to know the optomechanical parameters of the system, which we characterize in Sec. C, and the total attenuation between microwave source/vector network analyzer and the cavity entrance. We know the attenuator values on our input line (see Fig. 6), but we do not accurately know the cable loss.

To model our system, we extract the peak power observed on the first red and first blue sideband ($\omega_c \pm \omega_m$) and the power in the drive pedestal on the red sideband. Then we let Eq. (S1) evolve numerically until it has settled into a steady state, and simulate the steady state for 10 ms. We compute the Fourier transform of the output field, as in Eq. (S4), which gives us the observed power, while we obtain the mechanical oscillation amplitude from the size of the orbit of $\hat{x}, \hat{p}$ of Eq. (S1). We repeat this for all combinations of the cavity drive and sideband drive power (P_{mw} and P_{sb} respectively). The final observed spectrum of Eq. (S4) is multiplied with the scale factor (W/phonon) S_c found in Sec. C, compensated for the measurement bandwidth in the experiment and the finite simulation time.

We find good agreement between the experimentally observed powers and the simulations for a cable loss of 47.4 dB (of which 36 dB comes from the installed attenuators), and a 22.2 dB reduction of P_{sb} with respect to P_{mw}, which we attribute to the directional coupler. At these values, the simulated powers of the resonance peaks match the measured powers, as shown in Fig. S2 for the red (**A**) and blue (**B**) sidebands. At low power, the agreement between the simulations and measurements is good, but at high powers the Casimir effect starts to play a large role in the experiments, and the simulations overestimate the power. The simulated curves become less steep, but this is due to the optomechanical drive efficiency discussed in the main text and in the next section. The grey shaded area indicates the detection noise floor.

We repeat the numerical simulation for a 3 kHz detuned sideband drive, to simulate the sideband drive pedestal on the red sideband. All simulations fall on a perfect straight line that matches the experimental observations, as shown in Fig. S3. The combination of the off-resonant drive and the relative on-resonant powers in the red and blue sidebands provide an absolute reference of power that is independent of our detection efficiency or any amplifiers between resonator and detector.

The simulated amplitudes achieved by the mechanical resonator for all combinations of cavity and sideband drive powers are shown in Fig. S4. At small amplitudes, the maximum amplitude scales linearly with both cavity and sideband drive powers, but at some point this relation breaks down due to the drive efficiency. This drive efficiency deforms the Casimir curves we simulate, but it only flattens the top as shown in Fig. 3, and it does not affect the parts of the curve where the mechanical amplitude is small. To accurately choose a maximum amplitude of the Casimir curve we simulate in MatCont, we thus extrapolate the amplitude that the curve should have

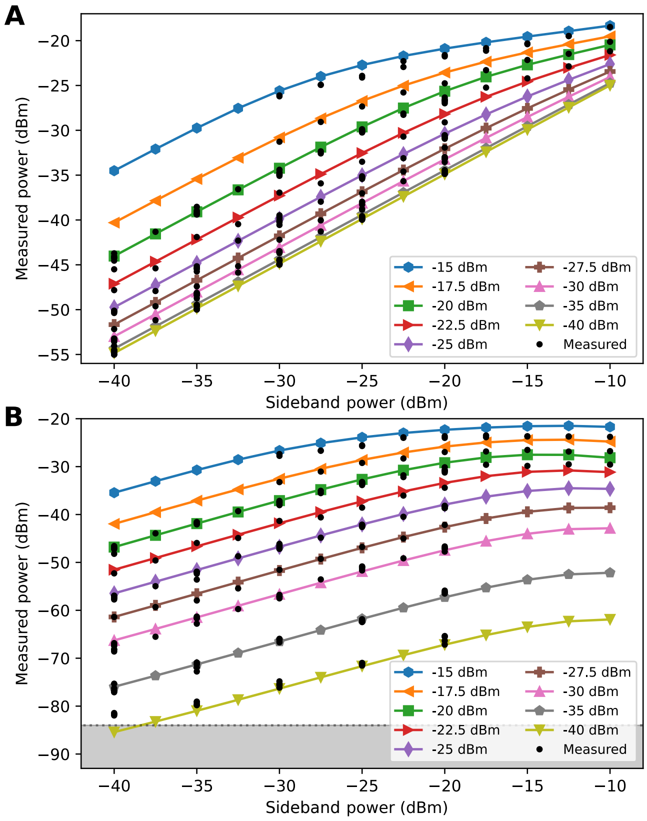

Fig. S2 | Sideband calibration. A Simulated powers (colored lines with various markers) and observed peak powers (black dots) for the red sideband. The legend indicates P_{mw}, the x-axis is P_{sb}. The agreement between the simulations and the measurements at low power serves as a calibration for the numerical simulations. **B** Idem, but for the blue sideband. The grey shaded area shows the noise floor for the measurements.

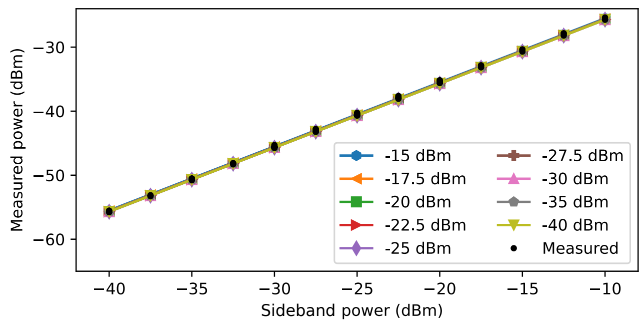

Fig. S3 | Input power calibration. The 3 kHz off-resonant drive simulations show a perfect overlap between all simulated (colored markers) and measured powers (black dots).

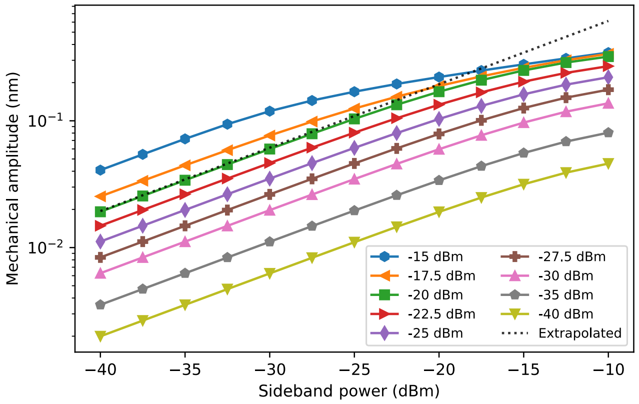

Fig. S4 | Calibrated mechanical amplitude. Calibrated amplitude achieved by the mechanical resonator for different combinations of cavity and sideband drive powers.

gotten without the drive efficiency. For this, we follow the linear parts of the curve at low power and extrapolate as indicated by the dotted line in Fig. S4 for the −20 dBm data set.

4. *Calculation of the drive efficiency*

The tenet of (dispersive) cavity optomechanics is that the cavity frequency ω_c shifts as a result of the mechanical position x[48]. In this work, the amplitude of x is significant, and the cavity frequency shift $\frac{\partial\omega_c}{\partial x}$ causes a mismatch between the cavity frequency and the drive frequencies, $\omega_{mw} \simeq \omega_c$ and $\omega_{sb} \simeq \omega_c - \omega_m$. The cavity frequency $\omega_c(t)$ is thus a function of time, it oscillates at ω_m depending on the exact trajectory of the drum.

To put it simply, for larger oscillations of x, the frequency mismatch between cavity and drive is greater and the power in the cavity decreases. The oscillation is fast with respect to the cavity linewidth, as we are in the resolved sideband limit $\kappa \ll \omega_m$, which means that the cavity amplitude changes slowly with respect to the oscillation of ω_m. Furthermore, we also have two drives separated in frequency. So while the power resulting from the drive at ω_c is maximal for small motions of x, the power resulting from the drive at $\omega_c - \omega_m$ peaks for some specific oscillation amplitude of x.

We calculate the drive efficiency by solving Eq. (S1) for $\gamma_m = 0$ such that the mechanical amplitude is fixed at the initial value we set for $x(t = 0)$. We let the system simulate only for a brief time, such that the cavity amplitude a has had time to stabilize but not enough time that the driving force affects the amplitude x. A good time span for this is $1600(\omega_m)^{-1} \simeq 80(\kappa)^{-1}$. From the last 20 mechanical periods, we extract the power in the cavity. This brief simulation is repeated for 101 values of x logarithmically spaced between 1 pm and 1 nm for all different cavity drive powers used in the experiments.

In the regime that is relevant for our experiment, the drive efficiency is 1 for small mechanical amplitudes (< 100 pm), and decreases quickly towards zero beyond that. However, at even larger mechanical amplitudes, beyond what we achieve in this work, the drive efficiency recovers to a non-negligible number in a series of bands that represent stable orbits as described in Ref.[60].

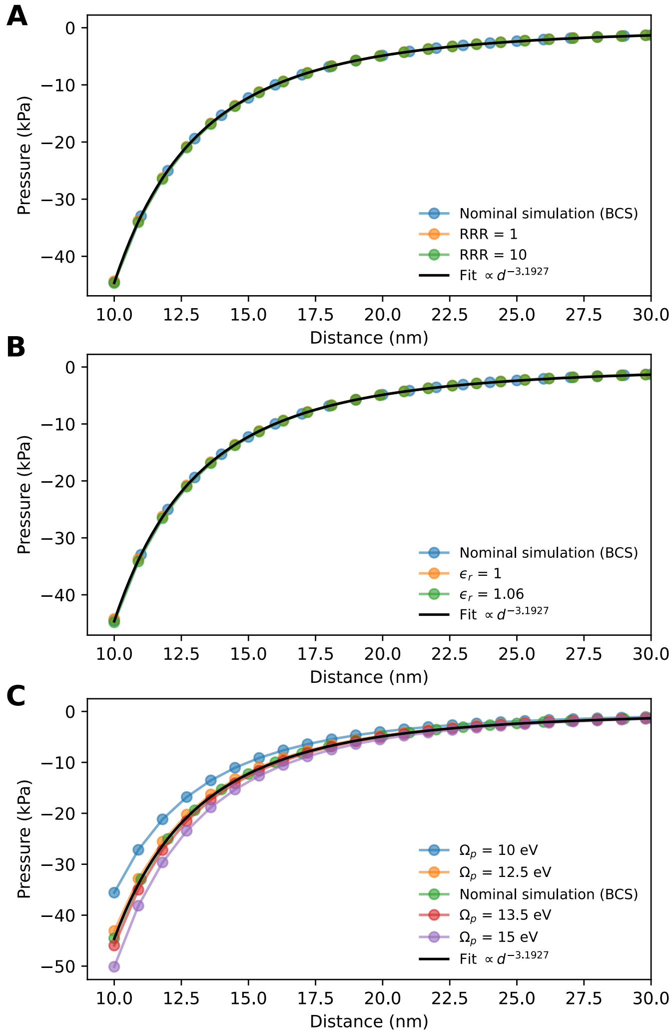

Fig. S5 | Effect of material parameters. A: The residual resistance ratio (RRR) rescales the dissipation rate $\gamma_p = \gamma_0/\mathrm{RRR}$, but varying it from the nominal value RRR = 2 does not significantly affect the Casimir pressure. **B:** Varying the relative permittivity of aluminium from the the nominal value $\epsilon_r = 1.03$ does not significantly affect the Casimir pressure. **C:** Varying the plasma frequency from the nominal value $\Omega_p = 13$ eV affect the Casimir pressure amplitude P more strongly than the Casimir scaling n.

B. Simulating the Casimir nonlinearity

1. *Role of Casimir parameters*

We perform the fit of distance d without considering variations in the calculated Casimir pressure, i.e., we consider the Casimir pressure amplitude P and scaling n to be fixed. To motivate this choice, we show that the Casimir pressure does not vary much with the material parameters γ_0 (or RRR), ϵ_0, and Ω_p. We repeat the Casimir pressure calculations for different material parameters, as shown in Fig. S5, and we fit curves of the form $P_c = P/d^n$ to distinguish changes in the amplitude of the Casimir pressure (P) from changes in the Casimir scaling (n).

The residual resistivity ratio, RRR, can vary depending on the material source and deposition method. We have previously measured that our aluminium has RRR = 2 using a four-point probe method. Variations in the RRR affect the phenomenological dissipation rate, $\gamma_p = \gamma_0/\mathrm{RRR}$, so Fig. S5**A** shows the effect of varying either RRR or γ_0. From the overlap between the curves, we conclude that RRR or γ_0 affect neither the Casimir pressure amplitude P nor the Casimir scaling n.

The relative permittivity of aluminium, $\epsilon_r = 1.03$ was experimentally determined and follows from the core-interband transitions of the aluminium atoms[54]. We show in Fig. S5 that variations in this parameter do not lead to significant changes in the Casimir pressure.

The plasma frequency of aluminium provides the upper frequency cutoff above which the material becomes transparent to the electromagnetic fluctuations that yield the Casimir effect. We take Ω_p = 13 eV from Ref.[54]. In Fig. S5 we show that varying Ω_p changes the Casimir pressure, but its effect on the Casimir scaling is marginal. A 25% variation in Ω_p corresponds to a 25% variation in P, but less than 1% variation in n.

To further motivate our choice to consider the calculated Casimir parameters as fixed values, we fit our experimental data to the Casimir force calculated with Ω_p = 10 and 15 eV. The results are shown in Fig. S6, where we have taken the optomechanical calibration of mechanical amplitude to be fixed. Taking Ω_p = 10 eV (Fig. S6**A**), the Casimir force is weaker, which means that to experience the same nonlinearity at fixed mechanical amplitude, the plate separation d must be reduced. Vice versa, taking Ω_p = 15 eV (Fig. S6**B**) leads to a better fit at larger d. The variations in Ω_p are significant (25% of the total value), and well beyond the uncertainty of which the plasma frequency is established in aluminium, yet the effect on the fitted parameter d is limited (~1 nm). Thus, we conclude that our choice to take the Casimir pressure amplitude and scaling to be fixed values leads to a smaller error than the optomechanical amplitude calibration does.

2. *Static shift of frequency and position*

As we illustrated in Fig. **1A**, we start with a harmonic oscillator centered at distance d from the other plate with unperturbed resonance frequency ω_r. The Casimir force pulls the top plate closer to the bottom plate, such that it oscillates around some value $d' < d$, and softens the spring so the mechanical frequency is decreased, $\omega_m < \omega_r$. We do not know d or ω_r a priori, but we can measure ω_m with great accuracy, leaving us to consider d (or somewhat equivalently the Casimir pressure P_c) as a parameter to be fitted. That means that for every value d, we have to find the value of the

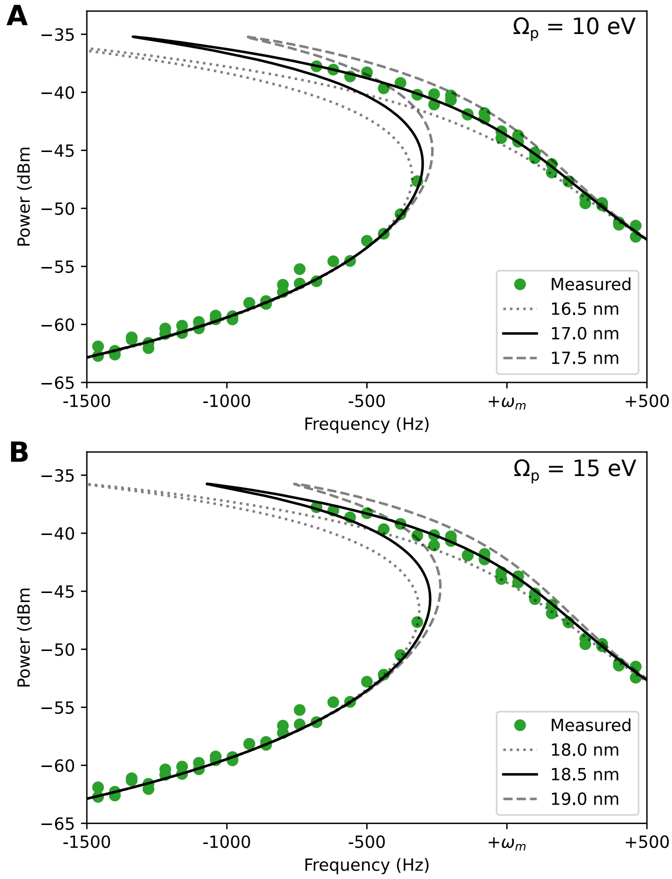

Fig. S6 | Fits for Casimir force variations. A: The Casimir force for a material with plasma frequency ω_p = 10 eV is weaker than the nominal Casimir force used in this work. The Casimir nonlinearity fits to a plate separation of d = 17.00 ± 0.25 nm. **B:** The Casimir force for a material with plasma frequency ω_p = 15 eV fits to a plate separation of d = 18.50 ± 0.25 nm.

unperturbed frequency ω_r such that the perturbed frequency $\omega_m = 2\pi \times 10.001$ MHz. Rather than finding a clever algorithm to compute the correct values of ω_r, we numerically evaluate the problem for a selection of d-values and interpolate. In Fig. S7 we show the frequencies ω_r that result in the correct value of ω_m for different values of d.

The numerical simulations of the Casimir oscillator in MatCont start with the drive frequency far detuned. To start the continuation, we need this step to converge to a solution. However, the total potential sketched in Fig. **1A** has a local minimum (where our resonator is) and a global minimum beyond the pull-in point. We need to feed MatCont the correct initial values such that it converges to the local minimum instead of showing us the pull-in collapse. To find these, we compute the position of the local minimum of the total potential for various values of d, while using the values of ω_r from Fig. S7. The unperturbed frequency ω_r is related to the mechanical stiffness needed to compute the potential, not ω_m. We plot the stable position of the local minimum for different values of d in Fig. S8. As with the unperturbed frequencies, we interpolate linearly between the calculated values for the

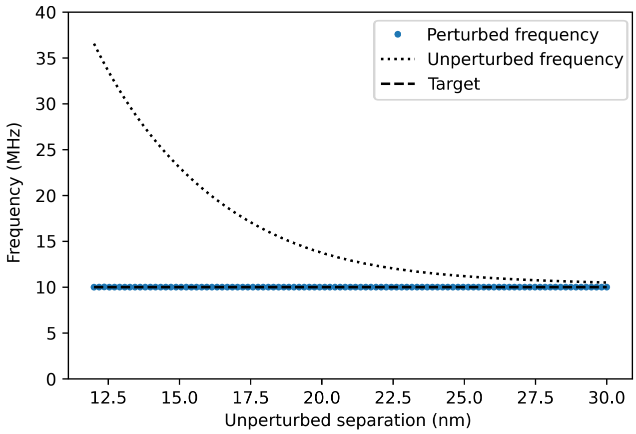

Fig. S7 | Casimir frequency shift. Plot of the unperturbed frequencies ω_r for various values of spacing d that result in the correct value for ω_m when the Casimir force is included.

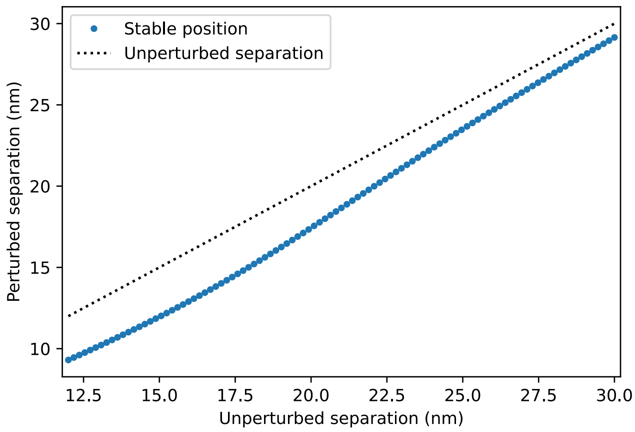

Fig. S8 | Shift of the local potential minimum due to the Casimir force. Distance between the local minimum (stable position) and the bottom plate for various values of the unperturbed separation d. The dotted line indicates where the initial separation would be the stable position. For d = 18.0 nm, the difference between the unperturbed separation and the local minimum is 2.9 nm.

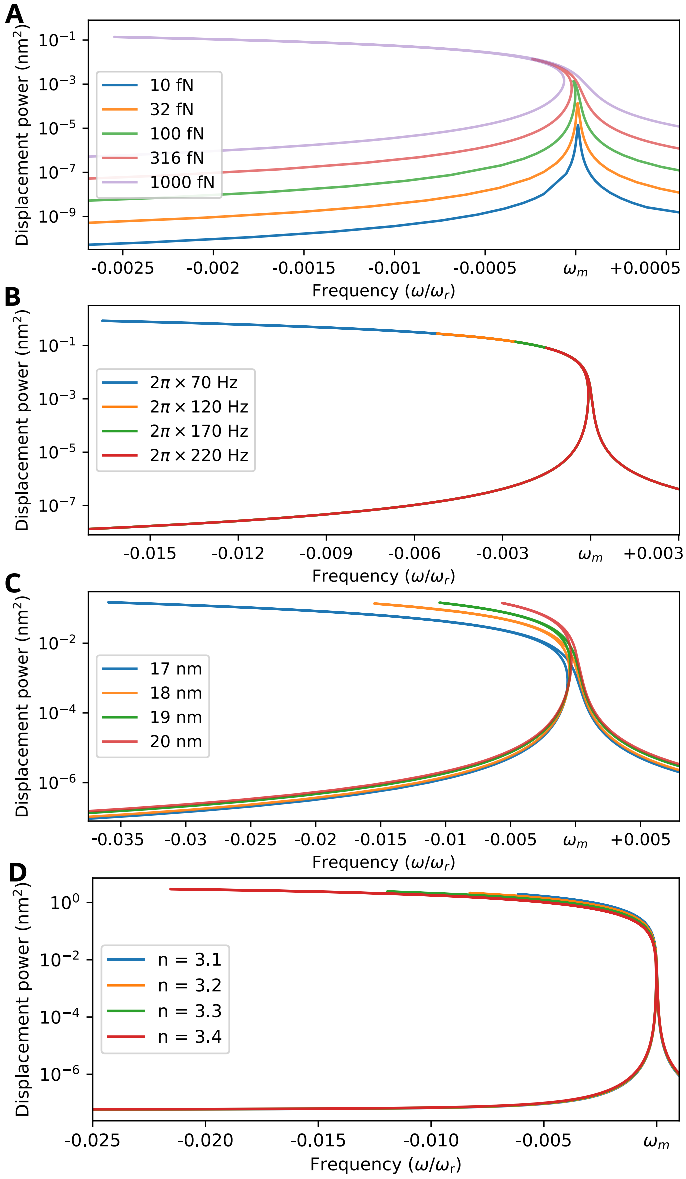

Fig. S9 | Effect of the Casimir force parameters. **A**: Effect of different drive force amplitudes F_d. **B**: Effect of varying the damping coefficient γ_r. **C**: Effect of varying the distance between the plates at mechanical zero. d. The frequencies of the curves have been shifted to align on ω_m. **D**: Effect of varying the Casimir scaling n, where the amplitude of the Casimir pressure has been fixed at the equilibrium position d'.

numerical simulations and fits of the main text.

3. *Role of mechanical parameters*

We study the effect of variations of the parameters of the Casimir effect through numerical simulations. We vary the drive force amplitude F_d, damping coefficient γ_r, separation distance d, and the Casimir exponent n. The results are shown in Figure S9.

We show how the system response transforms from linear behavior at small amplitude to nonlinear behavior at large amplitude in Fig. S9**A**. When the drive force amplitude is small, F_d = 10 fN, the frequency response of the system is Lorentzian, as expected. For larger amplitudes, the resonance peak broadens and becomes asymmetrical, indicative of nonlinear resonance where the response of the system is no longer linearly proportional to the drive force. The resonance frequency decreases with increasing amplitude, which indicates that the Casimir force is a strong softening nonlinearity.

In Fig. S9**B**, we study the effect of the mechanical damping rate γ_r. Lower damping allows for greater energy accumulation within the system at equal drive amplitudes, leading to larger oscillations and a more pronounced nonlinearity. However, all the backbones of the curves for different damping rates align, meaning the damping coefficient does not have a significant effect on the nonlinearity we observe.

The most important parameter for Casimir experiments is the separation distance d, which is the distance between the plates in the absence of the Casimir force. Since the Casimir effect strongly scales with the distance d, the Casimir force between drums spaced $d = 17$ nm apart (blue curve in Fig. S9**C**) causes a much stronger nonlinear behavior than for drums spaced $d = 18$ nm apart. The region where there are multiple solutions is much more extended, even if the amplitude of the mechanical oscillations remains the same. All curves were generated using the same drive force, which indicates that the separation distance d does not affect the mechanical amplitude significantly.

Finally, we show the effect of the Casimir force exponent n in Fig. S9**D**. The The Casimir pressure was adjusted for each n such that the value at the equilibrium position (d') was kept constant. While the trend from the change in n somewhat resembles the trend from the change in d, it is noticeable that the peaks curve more sharply with increasing n, while they start curving at lower amplitude for lower d.

C. Characterization of optomechanical system

1. *Calibration of the microwave cavity*

Our microwave cavity design was optimized to allow coupling to two separate drum resonators with two cavity modes, as shown in Fig. S10**A**, and described in more detail in the Supplementary of Ref.[39]. In our device, one of the drum resonators inadvertently collapsed and shorted one half of the cavity, though this cannot be seen in the microscope image. Instead, we deduce this by the number of microwave modes we see (one), its frequency ($\omega_c = 2\pi \times 5.46180$ GHz), and the number of mechanical signals we can observe in a wide-band frequency sweep at high red-sideband drive power (one).

We simulate our cavity using Sonnet, where we have replaced the collapsed drum by a short (Fig. S10**B**. At first, we replace the suspended drum by a numerical capacitance. An initial guess for the capacitance of this drum based on the diameter $2r = 11.3$ µm and a gap of 15.1 nm is 0.059 pF. To provide an initial estimate of the optomechanical coupling, we vary the spacing of the vacuum layer in our Sonnet model, and re-compute the cavity resonance frequency. We find $\frac{\Delta\omega_c}{\Delta x} \simeq 2\pi \times 104\ \mathrm{MHz\,nm^{-1}}$. We use the zero point motion $x_{zpf} = \sqrt{\frac{\hbar}{2 m_{eff}\omega_m}} = 4.6$ fm and estimate the coupling rate $g_0 \simeq x_{xpf}\frac{\Delta\omega_c}{\Delta x} \simeq 2\pi \times 480$ Hz. This is larger than the coupling rate that we find when we calibrate our system by about a factor 3, which we attribute to details not captured by our simulation: microscopic defects or fabrication imperfections, wire bonds, and box resonances. The simulated microwave cavity mode is not qualitatively affected by these limitations, but the we should treat the optomechanical coupling it yields as an optimistic estimate.

We characterize our microwave resonator by recording its reflected response (both amplitude and phase) and fitting this

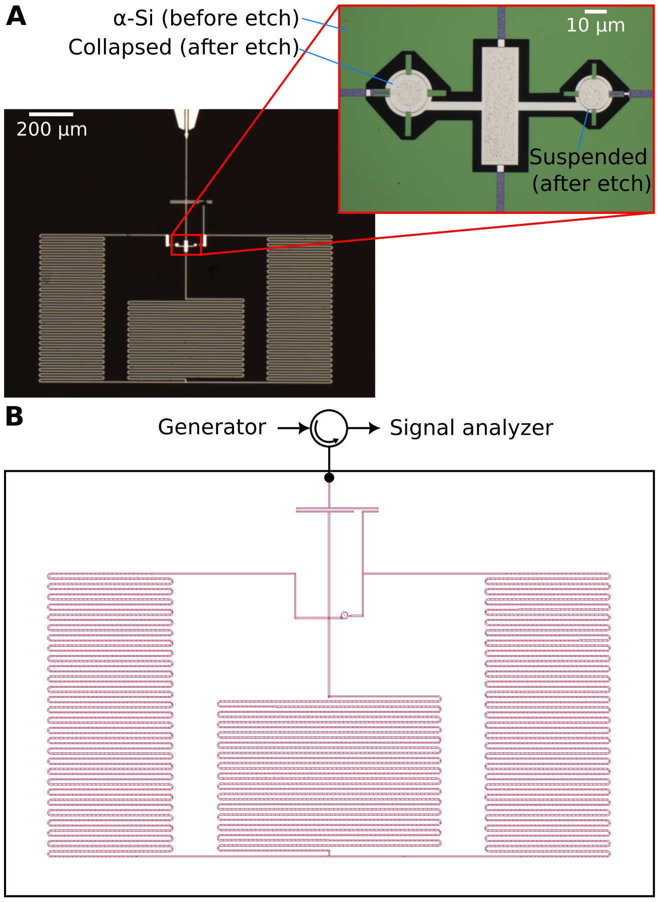

Fig. S10 | **Microwave cavity. A:** Microscope image of our microwave cavity (after the experiment), with the inset showing the drums (during fabrication). The larger (left) drum collapsed before the experiment, while the smaller (right) drum survived. **B:** Sonnet simulation of our cavity, with the collapsed drum replaced by a short.

with the equation[48]

$$R = \frac{(\kappa_i - \kappa_e)/2 - i(\Delta - \omega_c)}{(\kappa_i + \kappa_e)/2 - i(\Delta - \omega_c)}. \tag{S11}$$

Here, the square of the reflection coefficient, $|R|^2$, describes the probability that a photon reflects off our cavity. Furthermore, the internal and external linewidths, κ_i and κ_e, sum up to the total linewidth $\kappa = \kappa_i + \kappa_e$, and the detuning $\Delta = \omega_d - \omega_c$ describes the difference between the drive frequency ω_d and the cavity center frequency ω_c.

We use a three-step fit process. First, we de-trend the cavity signal by fitting a polynomial of order 2 to the first and last 10% of the amplitude signal, and a polynomial of order 1 to the same parts of the phase signal. This assumes the cavity resonance is approximately at the center of our measurement span, and that the background is reasonably flat within this span. Then we fit an ellipse to the response R on a Smith chart, from which we compute the cavity parameters and use those as initial guesses for the third and final step. By using scipy's `curve_fit` function[61], we fit our data to Eq. (S11). The response, fit and extracted parameters are shown in Fig. S11.

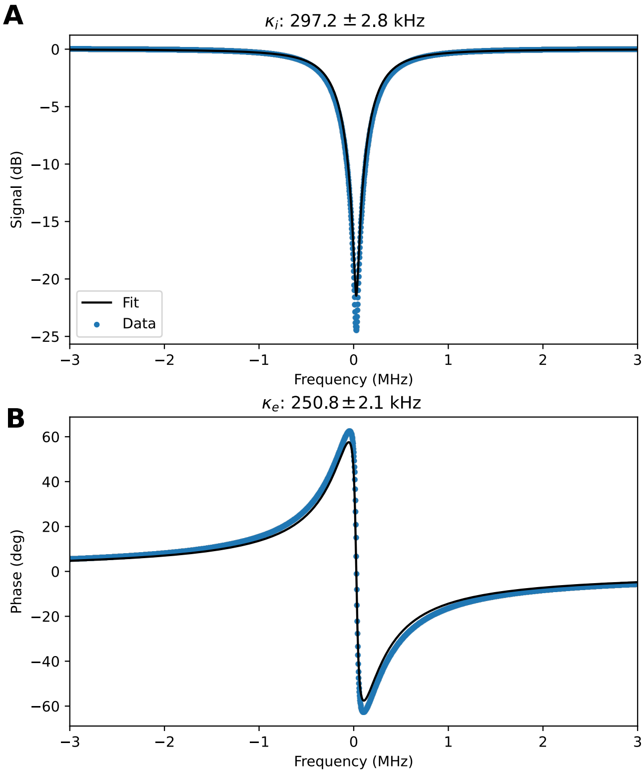

Fig. S11 | Microwave cavity calibration. **A**: Amplitude response of the microwave cavity (blue) and the fitted linewidth (black). **B**: Phase response of the microwave cavity (blue) and the fitted response (black). The internal and external linewidths, $\kappa_{\mathrm{i}} = 297.2 \pm 2.8$ kHz and $\kappa_{\mathrm{e}} = 250.8 \pm 2.1$ kHz respectively, are fitted as described in the text.

We fit the amplitude in logarithmic scale to enhance the accuracy around the cavity center, while the phase is fitted in linear scale.

Our cavity resonance frequency $\omega_{\mathrm{c}} = 2\pi \times 5.46180$ GHz, and the internal and external linewidths are $\kappa_{\mathrm{i}} = 2\pi \times 297.2 \pm 2.8$ kHz and $\kappa_{\mathrm{e}} = 2\pi \times 250.8 \pm 2.1$ kHz respectively.

2. *Thermalization of drum motion*

We calibrate the temperature to which the mode of our mechanical resonator thermalizes by sweeping the temperature of the dilution refrigerator. At each temperature, we measure the mechanical spectrum and fit a Lorentzian to the data. This way, we can extract the frequency ω_{m}, linewidth γ_{m}, and the area of the mechanical peak.

The amplitude of the thermal motion peak is shown in Fig.S12. It increases linearly with temperature below 200 mK. At higher temperatures the quasiparticles in the Al superconducting cavity shift and damp the cavity mode which reduce the readout efficiency. The peak amplitude stays proportional to the temperature all the way to the base temperature of 10 mK: we conclude that the drum thermalizes down to 10 mK and we use this assumption to extract g_0 in the next section.

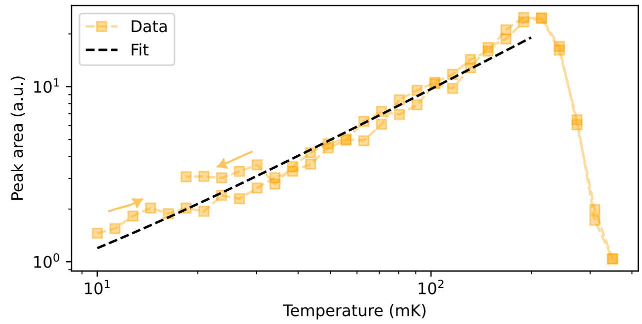

Fig. S12 | Thermalization of the drum mode. Area of the fitted mechanical peaks, indicating the thermal energy of the oscillator mode. The dashed curve is a linear fit offset by only about 3 mK, well below the base temperature of 10 mK, showing the good thermalization of the mode with the cryostat at the base temperature. At higher temperatures, the microwave cavity response disappears, likely due to quasiparticles in the superconductor (Aluminium), which shifts the microwave cavity frequency.

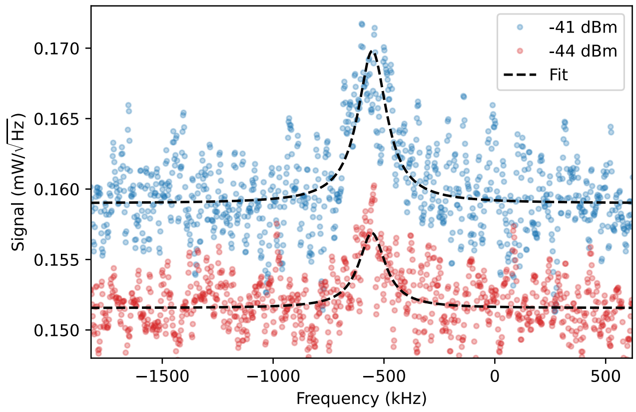

Fig. S13 | Calibration of the optomechanical coupling rate. The amplitude of the scattered peak is compared to a signal of known power (not shown). The area under the peak is calculated from a Lorentzian fit, and the ratio of the fitted peak with the signal of known power yields the optomechanical coupling rate g_0.

3. *Calibration of single-photon coupling*

The optomechanical coupling g_0 is calibrated by sending in a tone at the red sideband, $\omega_{\mathrm{c}} - \omega_{\mathrm{m}}$, and comparing the amplitude of the scattered peak with the amplitude of the drive. The resulting signal is shown in Fig. S13, and we fit a Lorentzian curve to the peak. We extract the area A under the curve, which is proportional to the number of scattered photons, and we compare it to the number of photons in the drive tone, $\hat{a}^{\dagger}_{\mathrm{sb}}\hat{a}_{\mathrm{sb}}$. The optomechanical coupling can be extracted from these amplitudes as

$$g_0^2 = \frac{A}{\hat{a}^{\dagger}_{\mathrm{sb}}\hat{a}_{\mathrm{sb}}} \frac{|1 - \kappa_{\mathrm{e}}\chi(\omega_{\mathrm{c}} - \omega_{\mathrm{m}})|^2 |\chi(\omega_{\mathrm{c}} - \omega_{\mathrm{m}})|^2}{|\chi\omega_{\mathrm{c}}|^2 n_{\mathrm{m}}}, \tag{S12}$$

which contains the ratio of the peak amplitude, as well as the cavity susceptibilities at the red sideband and cavity center (assuming zero detuning),

$$\chi(\omega_c - \omega_m) = \frac{1}{\kappa/2 + i\omega_m}$$
$$\chi(\omega_c) = \frac{1}{\kappa/2}. \tag{S13}$$

The thermal mechanical occupation can be calculated as

$$n_m = \frac{k_B T}{\hbar\omega_m}. \tag{S14}$$

With these expressions, we fit $g_0 = 2\pi \times 150 \pm 9$ Hz.

4. *Effective linewidth*

We account for optical damping (sideband cooling) by using an effective linewidth, γ_{eff} that relates to the intrinsic (low-power) mechanical linewidth γ_m via

$$\gamma_{\text{eff}} = \gamma_m + \frac{4g_0^2|\alpha|^2}{\kappa}P = \gamma_m + \eta P. \tag{S15}$$

Here, $|\alpha|^2$ is the number of photons in the cavity at the red sideband frequency, η is some coefficient which we are trying to fit and P is the power sent out from our microwave source at the red sideband frequency. The exact value of η depends not only on optomechanical parameters g_0 and κ, but also on the attenuation in the microwave lines between source and sample. However, as long as the latter are constant between measurements, we can use η and do not need to know the exact attenuation from our lines.

To fit the intrinsic linewidth, mechanical frequency and η, we vary the power sent in on the red sideband.

5. *Scale and phonon number calibration*

We do not know a priori the exact scaling between the spectral power that we measure and the expected spectral power of a single photon or phonon. Thus we need to derive an expression for the spectral power in terms of system parameters that can be measured, to use it as a fit function to our measurements.

We start from the equations of motion for the cavity field $\hat{a}$ and mechanical motion $\hat{b}$. In the sideband-resolved limit, with a drive ω_m lower than the cavity frequency (at the red sideband), with $\hat{a}$ separated into a steady state amplitude and some fluctuations $\hat{a} = \alpha + \delta\hat{a}$, the equations of motion can be written in the frequency domain as

$$\hat{a}[\omega] = \chi_c[\omega+\Delta]\left(-ig_0\alpha\left(\hat{b}[\omega] + \hat{b}^\dagger[\omega+2\omega_m]\right) + \sqrt{\kappa_i}\hat{a}_{in}[\omega]\right),$$
$$\hat{b}[\omega] = \chi_m[\omega]\left(-ig_0\left(\alpha^*\hat{a}[\omega] + \alpha\hat{a}^\dagger[\omega+2\omega_m]\right) + \sqrt{\gamma_m}\hat{b}_{in}[\omega]\right). \tag{S16}$$

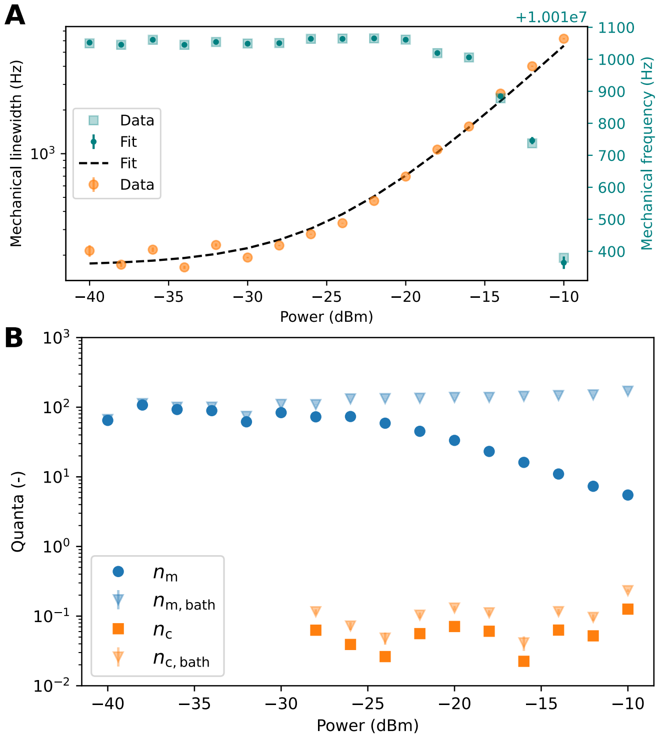

Fig. S14 | Power calibration. **A**: Mechanical linewidths (orange) and frequencies (teal) for various driving powers on the red sideband. **B**: Extracted mechanical occupation n_m and cavity photon number n_c, as well as the equivalent quanta in the respective thermal baths.

Here, the cavity susceptibility $\chi_c[\omega] = \frac{1}{\kappa/2 - i\omega}$ and the mechanical susceptibility $\chi_m[\omega] = \frac{1}{\gamma_m/2 - i\omega}$ are used as shorthands, and the input fields are $\hat{a}_{in}[\omega]$ and $\hat{b}_{in}[\omega]$.

In the good cavity limit, we can neglect the terms at $\omega \pm 2\omega_m$ and Δ. We can replace $\hat{b}[\omega]$ in our expression for $\hat{a}[\omega]$ and compute the spectrum S_{out} of the output field $\hat{a}_{out}[\omega] = \hat{a}_{in}[\omega] - \sqrt{\kappa_e}\hat{a}[\omega]$. We get

$$S_{out} = \frac{1}{2} + \kappa_e\kappa_i\left|\tilde{\chi}_c[\omega]\right|^2 n_{cav} + g_0^2|\alpha|^2\gamma_m\kappa_e\left|\tilde{\chi}_c[\omega]\chi_m[\omega]\right|^2 n_{th}. \tag{S17}$$

The three terms come from the external port of the cavity (vacuum), environmental noise at the cavity frequency (n_{cav}) and mechanical noise (thermal, n_m). The shorthand $\tilde{\chi}_c[\omega] = \frac{\chi_c[\omega]}{1+g_0^2|\alpha|^2\chi_c[\omega]\chi_m[\omega]}$ denotes the cavity susceptibility that is modified due to the optomechanical interaction. In the fitting procedure, we subtract the constant offset, so the factor $1/2$ in Eq. (S17) disappears. Our final fit has the form $S_{fit} = S_c \times (S_{out}[\omega] - 1/2)$, and requires knowing $\kappa_e, \kappa_i, \gamma_m, g_0, \alpha, n_{cav}$, and n_{th} to extract our fit paramater, scale S_c. In favor of knowing α directly, we can use $g_0^2|\alpha|^2 = \frac{\kappa\eta P}{4}$ using the parameter η defined in Eq. (S15).

The fit procedure is as follows: We assume that at sufficiently low red-detuned drive power, the mechanical occupation is unperturbed by the drive. For the points at the lowest powers shown in Fig. S14A, below −32 dB, n_m is known from the reference temperature obtained from the thermalization step. Then we use the power-dependence parameter η

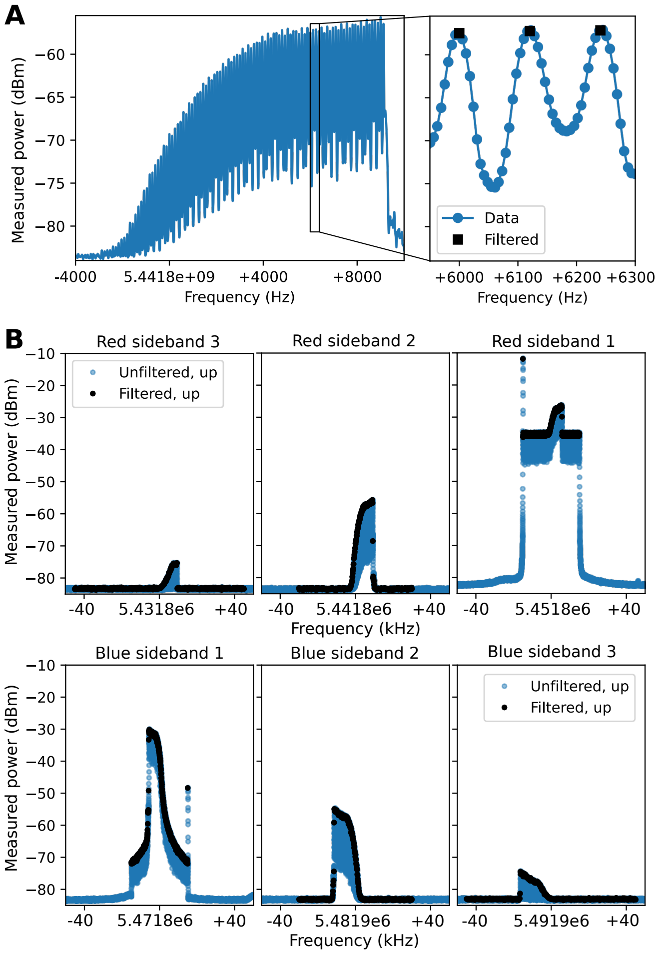

Fig. S15 | Data filtering. **A**: The measured power on the spectrum analyzer shows periodic peaks at the sideband drive frequency steps. We filter out the peaks located at these frequencies (black squares). **B**: All sidebands as recorded on the spectrum analyzer (blue) and filtered (black). Clearly visible is the noise pedestal due to the drive at the first red sideband. The sharp peak at the edge of the pedestal is from the vector network analyzer start/stop frequency.

obtained from the effective linewidth step, and fit the data at all powers to obtain n_m and n_c at each power. The effective linewidth is shown in Fig. S14**A**, with intrinsic mechanical linewidth $\gamma_\mathrm{m} = 168.9 \pm 9.5$ Hz and power factor $\eta = 5.37 \cdot 10^4$ Hz mW^{-1} completing the fit.

With our initial guess of the occupation numbers, we subsequently refine the fits of our scale parameter and η (now using the whole dataset). Using the updated values, we re-fit n_m and n_c at all powers, and the final result is shown in Fig. S14**B**. In the plots, we have used the final $\eta = 5.37 \cdot 10^4$ Hz mW^{-1}, and scale $S_c = 2.04 \cdot 10^{-15}\ \frac{\mathrm{W}/\sqrt{\mathrm{Hz}}}{n_\mathrm{c}}$.

D. Data filtering

Due to limitations of our vector network analyzer, we drive our system at a series of discrete frequencies instead of a continuous sweep. This way, we can control the step size and direction, which allows us to do a bidirectional measurement where the drive frequency first increases and then decreases. We record the response of our system on a separate spectrum analyzer (SA), which integrates for the full duration of the increasing/decreasing segments separately. The response measured at the second red sideband ($\omega_\mathrm{c} - 2\omega_\mathrm{m}$) during the upwards frequency sweep is shown in Fig. S15**A**.

Our SA records the spectrum using a much finer set of points than the frequencies at which the vector network analyzer outputs its drive. This condition creates a periodic pattern of peaks in the SA-recorded spectrum, which obscures the true shape of the curve. We are only interested in the tops of the peaks, since there is no sideband drive at the frequencies between the peaks. We filter the SA points in a small bandwidth around each of the vector network analyzer output frequencies, and integrate the power over that bandwidth. The filtered signal is a much shorter set of points that traces out the tops of the peaks. We have plotted the unfiltered data and the filtered signals as blue dots and black squares respectivel in Fig. S15**A**.

E. Exclusion of other sources of nonlinearity

1. *Electrostatic nonlinearity: Average potential offset*

The top and bottom plates of our drum form a capacitance separated by a vacuum gap at equilibrium of $d' \simeq 15$ nm. Any static average potential difference between the plates exerts an attractive force between the plates, which has been used in a similar system to tune the vacuum gap[30]. In our system, the top and bottom plates are connected directly through the superconducting cavity, thus they are two sides of the same superconductor. In the absence of a large thermal gradient across our device, we expect the average potential difference between the plates to be negligibly small. Nonetheless, if there were a 1 V static average potential difference, this would correspond to a pressure of $P_\mathrm{elec} \simeq 150$ Pa for $d' = 15$ nm (based on a COMSOL simulation, as shown in Fig. S16). This pressure is negligible compared to the Casimir pressure, which at this distance is $P_\mathrm{c} = 12.0 \pm 0.6$ kPa.

Our experiment is not directly sensitive to the absolute value of the (Casimir) pressure, and neither are we directly sensitive to any absolute pressure from the electrostatic force. We are sensitive to the *nonlinearity* that originates from these effects: The electrostatic force contributes a softening nonlinearity that scales with $P_\mathrm{elec} \propto d^{-2}$. This scaling is much weaker than the Casimir force scaling, $P_\mathrm{c} \propto d^{-3.2}$. Since the magnitude of the electrostatic force is much less and the nonlinearity scales much weaker than the Casimir force, the effect from the average potential difference is negligible.

2. *Electrostatic nonlinearity: Potential patches*

It is well known that crystal grain orientations can cause local differences in the electrostatic potential[62], also known

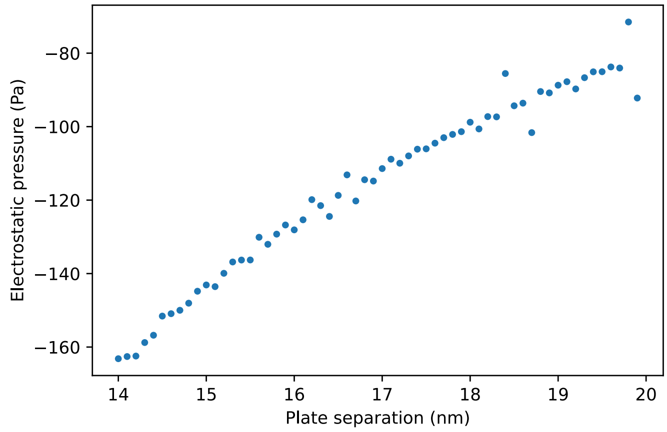

Fig. S16 | Electrostatic effects. Electrostatic pressure due to a 1 V static potential offset between the drum plates, as a function of their separation distance *d*. Due to the small energies involved and the geometry of the simulation, it is sensitive to mesh-related inaccuracies.

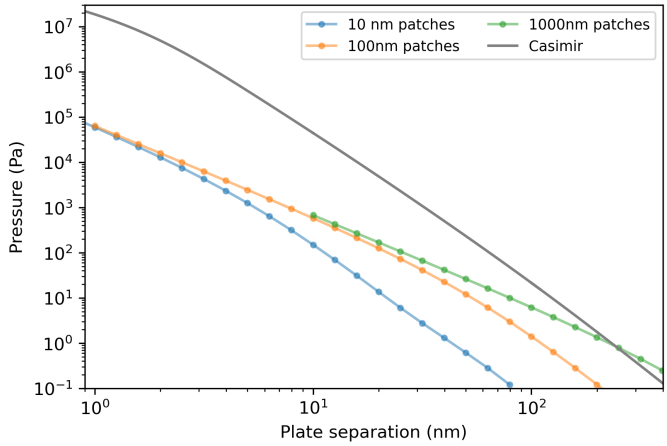

Fig. S17 | Patch pressure. Calculated Casimir pressure and patch potential pressure for patches normally distributed with a standard deviation of 100 mV, for various patch sizes.

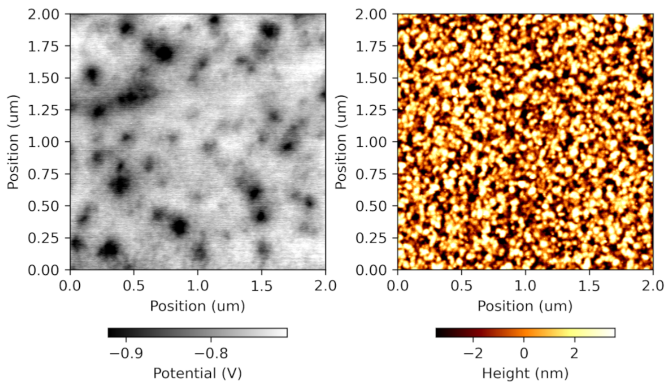

Fig. S18 | Potential patches. Measured surface potential (left) and height (right) of a 2×2 μm^2 aluminium film from the same fabrication batch as the sample studied in the main text.

as potential patches[63]. This means that although two closely spaced conductors may have the same *average* potential, there may still be a non-zero attractive electrostatic force between the conductors. Numerical simulations of randomized patch geometries can be used to estimate the force contributed by these potential patches[50,63,64]. Such numerical simulations rely on accurate information about the (lateral) sizes of these patches, as well as their voltage distribution[65,66].

We experimentally measure the patches in our aluminium to have a characteristic size of $\ell = 158$ nm and a potential intensity that falls well within a normal distribution width $\sigma = 100$ mV. With these numbers, we overestimate the pressure exerted by potential patches by about a factor 10. Nonetheless, we find that the patch pressure is several orders of magnitude smaller than the Casimir pressure at our equilibrium position $d' = 15.1$ nm, as shown in Fig. S17. We exclude that potential patches are responsible for the nonlinearity that we observe in our mechanical resonator. We describe the experimental details in the next paragraphs.

KPFM measurement of patches
We use Kelvin Probe Force Microscopy (KPFM) to locally measure the potential on our sample, which is a well-established technique based on a conductive atomic force microscope cantilever[67,68]. We use a sample that was fabricated in the same batch as the sample reported in the main paper. The KPFM measurement results are plotted in Fig. S18, where we see characteristic aluminium spots where the potential is $\simeq 100{-}200$ mV below the mean. This corresponds to the work function difference between the different crystalline orientations of aluminium: The work function of aluminium in the $\langle 100 \rangle$-direction is 4.20 eV, in the $\langle 110 \rangle$-direction it is 4.06 eV and in the $\langle 111 \rangle$-direction it is 4.26 eV[69]. There is no correlation between the potential and height, which are measured simultaneously.

Patch intensity
We expect a Gaussian distribution of the potentials, since the crystalline orientations should be random. But when we bin the measurement points of the potential, the Gaussian fit shown in Fig. S19 is not a good fit. There is a distinct tail towards lower potentials, which represents the spots seen in Fig. S18. The Gaussian fit is centered around a mean value -768 mV with a standard deviation σ of 30.4 mV. The mean potential seen in Fig. S18 is due to being measured center conductor of the cavity, which is not directly connected to ground. Our KPFM tip touches down before the measurement and this transfers some charge to the sample. Any excess charge leaks out over time (timescale of approximately 30 minutes in air), so our measurement shows some offset potential.

Patch size
Besides the intensities of the potential patches, their spatial extent (average patch feature size ℓ) strongly affects the distance scaling of the electrostatic force they exert[50,64]. Recent simulations show that the lateral resolution of the KPFM probe can lead to an overestimation of the patch size and an underestimation of the patch intensity[70]. We use ASYELEC02 probes in our AFM, which have a nominal tip ra-

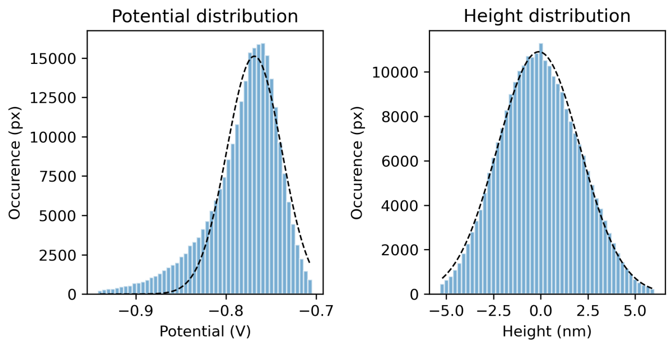

Fig. S19 | Potential patch statistics. Distribution of the measured potentials and heights for the area shown in Fig. S18, and Gaussian fits (dashed black lines).

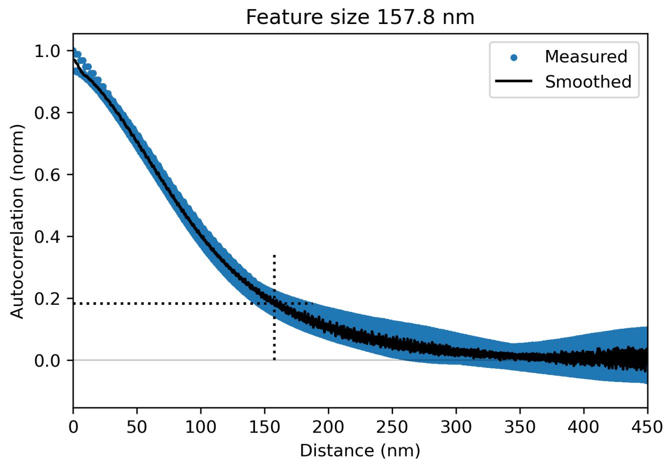

Fig. S20 | Potential patch size. Autocorrelation of the potential shown in Fig. S18. The average patch size ℓ_p is the distance at which the normalized autocorrelation drops to $1/2e \simeq 0.184$ (dotted lines), which is 157.8 nm for our aluminium film.

dius of 25 nm, and operate in tapping mode with an amplitude 10 nm. With these numbers, we can estimate the lateral resolution of our KPFM measurement using[71] $\ell_{\min} = \sqrt{RH} \simeq 16$ nm where R is the tip radius and H is the minimal tip-sample distance. We determine the average size of the experimentally measured patches using the `correlate2d` function from Scipy, which is plotted in Fig. S20. We find the average patch size ℓ_p is 158 nm, which is well above our minimal lateral resolution, $\ell_p \gg \ell_{\min}$. Thus there is no reason to assume we significantly overestimate the characteristic patch size ℓ or underestimate the patch intensity distribution width σ. Our KPFM measurement also measures the height variation in our sample. The height is well-described by a Gaussian fit centered around −0.1 nm with a σ_h of 2.19 nm and a characteristic feature size $\ell_{\text{height}} = 32$ nm, as shown in Fig. S19.

Patch textures reproducibility

Our patch characterization was performed on a sample that was processed identically (i.e., in the same batch) as the sample in which we measured the Casimir force. We have measured the patch statistics on 8 separate areas on the aluminium parts of the sample, and obtained similar patch intensities and patch sizes. The average patch intensity distribution width from all 8 areas $\sigma_{\text{mean}} = 36$ mV, and the average patch size is $\ell_{\text{mean}} = 160$ nm, with both parameters varying minimally between different measurement areas.

While some processing steps greatly affect the size and intensity of potential patches[72], we have performed KPFM measurements on multiple samples (from different batches) and found our processing does not significantly affect the potential patches. The patch intensity does not appear affected by our release etch step, as we have measured $\sigma_{\text{mean}} = 41$ mV before release ($\sigma_{\text{mean}} = 36$ mV after). The heat treatment step has the largest effect on the patch intensity, $\sigma_{\text{mean}} = 63$ mV before any heat treatment, $\sigma_{\text{mean}} = 55$ mV after 15 minutes of 200 °C, $\sigma_{\text{mean}} = 47$ mV after 15 minutes of 240 °C, $\sigma_{\text{mean}} = 42$ mV after 15 minutes of 260 °C, and $\sigma_{\text{mean}} = 41$ mV after 15 minutes of 280 °C. These findings appear consistent with potential patches that originate solely from the crystalline structure of the material. Our patch measurements were performed on a sample that has been processed simultaneously and identically to the experimentally reported sample, so we consider them to be representative of the patches present in the drum we tested.

Estimate of patch forces

We calculate the effect of patches for our drum geometry using the simulation framework we developed in an earlier work[50]. We generate Voronoi patterns based on randomized patches of various sizes, with normally distributed potentials with a $\sigma = 100$ mV. Our patterns consist of 400 patches, and we compute the electrostatic energy. From the variation of energy with plate separation, we extract the pressure from the patch potentials for various plate separations as shown in Fig. S17. We find the well-known limit behaviors with the patch size[63]: When $\ell \gg d$, $P_{\text{patch}} \propto d^{-2}$, while when $\ell \ll d$, $P_{\text{patch}} \propto d^{-4}$. The regime where $\ell \gg d$ leads to the greatest patch pressure in absolute sense, yet this is still several orders of magnitude smaller than the Casimir pressure for our plate separation $d = 15$ nm. We find $P_{\text{patch}} = 230$ Pa at a vacuum gap of 15 nm, much smaller than the Casimir pressure $P_c = 12000 \pm 600$ Pa, as shown in Fig. S17. We note that in Casimir experiments at larger distances ($d \gtrsim 200$ nm), the Casimir pressure can be comparable in amplitude to the patch pressure.

3. *Mechanical nonlinearity: Geometric origin*

There is a significant body of literature on the mechanical nonlinearities with a purely geometric origin. In our experimental platform of superconducting Aluminium drum resonators, Ref.[73] provides an excellent theoretical background that is experimentally tested in Ref.[74]. The nonlinearity due to geometry is a *hardening* nonlinearity in these drum resonators, both on theoretical grounds and experimental evidence[73,74]. The Casimir force contributes a *softening* nonlinearity, which is exactly what is described in the main text, and thus we exclude the geometric nonlinearity on qualitative grounds.

Furthermore, we can exclude the geometric mechanical nonlinearity on quantitative grounds. We follow the method of Ref.[73], which is based on Kirchoff-Love theory for circular membranes. The first assumption in this method is that the resonator is essentially a 2D circular membrane with coordinates (r, θ), which has modes purely moving in the out-of-plane z direction. From COMSOL simulations, we verify that the mode shown in Fig. **8B** consists for $> 99\%$ of motion in the z-direction. Thus we separate the variables of the function $f_{n,m}$ describing the motion of our structure for the (n, m) mode,

$$f_{n,m}(r, \theta, t) = z_{n,m}(t)\psi_{n,m}(r, \theta). \tag{S18}$$

The part $z_{n,m}(t)$ describes the oscillating motion, and $\psi_{n,m}(r, \theta)$ is the normalized mode shape. The mass and stiffness parameters of the fundamental mode (which is the one we study) are given as[73]

$$\begin{aligned}
\mathcal{M}_{0,0} &= \rho h \int_0^{2\pi} \int_0^{R_\mathrm{d}} (\psi_{0,0}(r, \theta))^2\, r dr d\theta, \\
\mathcal{K}_{0,0} &= \frac{1}{12} \frac{E h^3}{1 - \nu_\mathrm{r}^2} \int_0^{2\pi} \int_0^{R_\mathrm{d}} \left(\psi_{0,0}(r, \theta) \Delta^2 \psi_{0,0}(r, \theta)\right) r dr d\theta \\
&\quad + h\sigma_0 \int_0^{2\pi} \int_0^{R_\mathrm{d}} (\psi_{0,0}(r, \theta) \Delta \psi_{0,0}(r, \theta))\, r dr d\theta.
\end{aligned} \tag{S19}$$

We denote the material parameters: ρ is the density of the drum material, E is the Young's modulus, ν_r the Poisson's ratio, and σ_0 the stress (negative for tensile stress). The drum geometry is taken into account via the drum radius R_d and thickness h. Finally,

$$\Delta ... = \frac{1}{r} \frac{\partial ...}{\partial r} \left(r \frac{\partial ...}{\partial r} \right) + \frac{1}{r^2} \frac{\partial^2 ...}{\partial \theta^2} \tag{S20}$$

is the Laplacian operator in polar coordinates. From Eq. (S19), we can calculate the mode frequency $\omega_{0,0} = \sqrt{\mathcal{K}_{0,0}/\mathcal{M}_{0,0}}$.

In the COMSOL model shown in Fig. **8**, we use material parameters $\rho = 2700\ \mathrm{kg\,m^{-3}}$, $E = 76.6$ GPa, $\nu_\mathrm{r} = 0.32$, and the average value of the von Mises stress over the drum domain, $\sigma_0 = -270$ MPa (following the convention of Ref.[73], tensile stress is negative in the analytical description, while in the COMSOL plots tensile stress is positive). Combined with the drum diameter $2R_\mathrm{d} = 11.3\ \mu$m and the thickness of the evaporated Al $h = 120$ nm, we can evaluate Eq. (S19). We find $\mathcal{M}_{0,0} = 1.38 \times 10^{-13}\ \mathrm{kg\,m^2}$ and $\mathcal{K}_{0,0} = 1467$ N m. The resulting frequency $\omega_{0,0} = 2\pi \times 16.4$ MHz is close to our bare resonator frequency $\omega_\mathrm{r} = 2\pi \times 16.3$ MHz.

The geometric nonlinearity can be captured in a cubic term ($\propto x^3$), and its coefficient for the fundamental mode can be found from the expression[73]

$$\tilde{\mathcal{K}}_{0,0} = -\frac{Eh}{R_\mathrm{d}^2} \frac{C_{0,0}^{(1)}}{1 - \nu_\mathrm{r}} \int_0^{2\pi} \int_0^{R_\mathrm{d}} (\psi_{0,0}(r, \theta) \Delta \psi_{0,0}(r, \theta))\, r dr d\theta \tag{S21}$$

where $C_{0,0}^{(1)} = 0.389664$ as tabulated in Table IV of Ref.[73]. From our COMSOL simulations, we obtain $\tilde{\mathcal{K}}_{0,0} = 3.55 \times 10^{15}\ \mathrm{N\,m^{-1}}$. We then relate this to the coefficient α_D of the Duffing term,

$$\ddot{x} + \gamma_\mathrm{r}\dot{x} + \omega_\mathrm{r} x + \alpha_\mathrm{D} x^3 = \frac{F_\mathrm{d}}{m_\mathrm{eff}}, \tag{S22}$$

where $\alpha_\mathrm{D} = \tilde{\mathcal{K}}_{0,0}/\mathcal{M}_{0,0} = +2.57 \times 10^{28}\ \mathrm{m^{-2}\,s^{-2}}$. This value is close to the experimental fit of Refs.[73,74], which is $\alpha_\mathrm{D} = +7\times10^{27}\ \mathrm{m^{-2}\,s^{-2}}$ in a drum resonator that is of nearly identical design to the one in this work.

From the coefficient α_D, we can estimate that a +1 Hz frequency shift should occur if the motional amplitude is $x \simeq 0.6$ nm. At those amplitudes, we see a multiple-kHz *negative* frequency shift corresponding to the Casimir force. Thus we can exclude the geometrical mechanical nonlinearity based on the magnitude and sign of the frequency shift.

4. Nonlinear optomechanical coupling

The optomechanical cavity is formed by a plate capacitor where one of the plates is mechanically compliant. The coupling strength g_0 is related to the shift in cavity frequency and to the capacitance C as[48,74]

$$\begin{aligned}
g_0 &= -G x_\mathrm{zpf} \\
G &= \frac{\partial \omega_\mathrm{c}}{\partial x} = \frac{\partial \omega_\mathrm{c}}{\partial C} \frac{\partial C}{\partial x}.
\end{aligned} \tag{S23}$$

The capacitance between two plates is not a linear function of their separation distance d, and g_0 is typically based only on the first-order Taylor series of the capacitance in x/d. To estimate the 'higher order' optomechanical couplings that stem from the nonlinearity of the capacitance expansion, we follow the method of[74]. The cavity frequency and couplings up to third order in x are

$$\begin{aligned}
\omega_\mathrm{c}(x) &= \omega_\mathrm{c}(0) - \left[g_0 \frac{x}{x_\mathrm{zpf}} + \frac{g_1}{2} \left(\frac{x}{x_\mathrm{zpf}} \right)^2 + \frac{g_2}{2} \left(\frac{x}{x_\mathrm{zpf}} \right)^3 \right] \\
g_1 &= g_0 \left[2 \frac{x_\mathrm{zpf}}{d} - 3 \frac{g_0}{\omega_\mathrm{c}(0)} \right] \\
g_2 &= g_0 \left[2 \left(\frac{x_\mathrm{zpf}}{d} \right)^2 - 6 \frac{x_\mathrm{zpf}}{d} \frac{g_0}{\omega_\mathrm{c}(0)} + 5 \left(\frac{g_0}{\omega_\mathrm{c}(0)} \right)^2 \right]
\end{aligned} \tag{S24}$$

For the parameters of our system, we evaluate $g_0 = 2\pi \times 150$ Hz, $g_1 = 2\pi\times6.4\times10^{-5}$ Hz and $g_2 = 2\pi\times1.4\times10^{-11}$ Hz. For a motion amplitude of $x = 1$ nm, which is much larger than anything we observe, the linear frequency shift (only g_0) is $\Delta\omega_\mathrm{c} = -32.58$ MHz, the quadratic shift (both g_0 and g_1) would be $\Delta\omega_\mathrm{c} = -34.10$ MHz and the cubic shift (g_0, g_1, and g_2) would be $\Delta\omega_\mathrm{c} = -34.17$ MHz. These higher-order capacitance contributions are only a relevant contribution to the frequency shift for extremely large displacements ($\simeq$ nm). At these displacements, the frequency shift is much larger than the cavity linewidth, $\Delta\omega_\mathrm{c} \gg \kappa$, so the drive efficiency that we describe in the main text is the most important optomechanical effect to take into account. We emphasize that the nonlinearity from the plate capacitor expansion only affects the *cavity* frequency shift and not the mechanical frequency shift from the Casimir force.

Quantity	Symbol	Value
Unperturbed frequency	ω_r	$2\pi \times 16.710$ MHz
Mechanical frequency	ω_m	$2\pi \times 13.688$ MHz
Mechanical linewidth	$\gamma_r \simeq \gamma_m$	$2\pi \times 231 \pm 4$ Hz
Cavity frequency	ω_c	$2\pi \times 7.589718$ GHz
External linewidth	κ_e	$2\pi \times 304.7 \pm 2.8$ kHz
Internal linewidth	κ_i	$2\pi \times 608.7 \pm 6.2$ kHz
Optomechanical coupling	g_0	$2\pi \times 67 \pm 3$ Hz
Effective mass	m_{eff}	3.96×10^{-14} kg
Rest separation without Cas. f.	d	19.1 ± 0.5 nm
Rest separation	d'	17.3 ± 0.5 nm
Bottom plate diameter	$2r$	11.3 µm
Casimir amplitude	P	$(1275 \pm 7) \cdot 10^{-24}$ Pa m^n
Casimir force scaling exponent	n	3.193

Table 2 | Parameters of the second device.

F. Measurements on a second device

We have repeated the experiments of the main text in a second device, fabricated using an identical design but in a different fabrication run. The parameters of the device were characterized using the same method as for the device in the main text, and they are reported in Table **2**. In the absence of the Casimir force, the devices have a similar mechanical resonance frequency. However, this second device has a slightly different separation of the plates at mechanical zero (d), the final mechanical frequency is rather different due to the non-linear nature of the Casimir force. Due to the lower optomechanical coupling rate, and higher cavity linewidth, it requires more drive power to reach larger displacement amplitudes, and we are limited by the maximum power that our measurement chain can handle. These measurements were performed in a different dilution refrigerator to the experiments in the main text, with a separate set of measurement equipment.

One of the mechanical response curves of the second device is shown in Fig. S21. We have performed the same calibration procedure as in the device of the main text, and extract $d = 19.1 \pm 0.5$ nm (solid black line) from a fit to the data. For completeness, we also show the theory curves for $d = 19.6$ nm (dotted black line) and $d = 18.6$ nm (dashed black line).

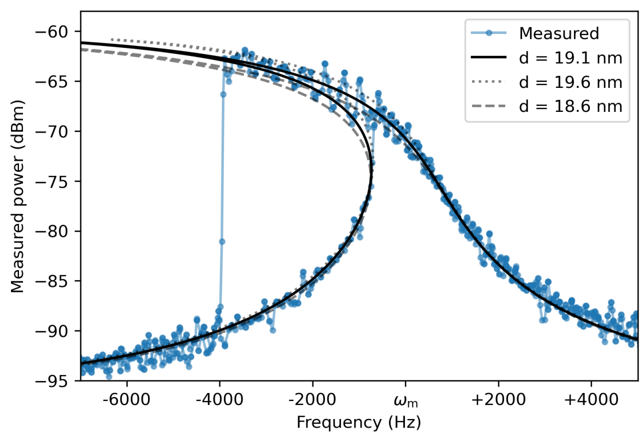

Fig. S21 | Measurement of the Casimir nonlinearity in a second device. The measured Casimir curve (blue) for 10 dBm cavity drive power and 0 dBm red sideband drive power. The theory curves based on the Casimir force for a separation of mechanical zero of $d = 19.1$ nm (solid black line), $d = 19.6$ nm (dotted black line) and $d = 18.6$ nm (dashed black line) are overlaid on the measured data. The $d = 19.1$ nm curve is closest to the center of the measured data.

[1] H. B. G. Casimir, On the attraction between two perfectly conducting plates, Proc. Kon. Ned. Akad. v. Wet. **51**, 793 (1948).

[2] E. M. Lifshitz, The theory of molecular attractive forces between solids, Journal of Experimental and Theoretical Physics **2**, 73 (1956).

[3] S. K. Lamoreaux, Demonstration of the Casimir force in the 0.6 to 6 μm range, Physical Review Letters **78**, 5 (1997).

[4] U. Mohideen and A. Roy, Precision measurement of the Casimir force from 0.1 to 0.9 μm, Physical Review Letters **81**, 4549 (1998).

[5] A. W. Rodriguez, F. Capasso, and S. G. Johnson, The Casimir effect in microstructured geometries, Nature Photonics **5**, 211 (2011).

[6] L. M. Woods, D. A. R. Dalvit, A. Tkatchenko, P. Rodriguez-Lopez, A. W. Rodriguez, and R. Podgornik, Materials perspective on Casimir and van der Waals interactions, Reviews of Modern Physics **88**, 045003 (2016).

[7] T. Gong, M. R. Corrado, A. R. Mahbub, C. Shelden, and J. N. Munday, Recent progress in engineering the Casimir effect - applications to nanophotonics, nanomechanics and chemistry, Nanophotonics **10**, 523 (2021).

[8] F. M. Serry, D. Walliser, and G. J. Maclay, The role of the Casimir effect in the static deflection and stiction of membrane strips in microelectromechanical systems (MEMS), Journal of Applied Physics **84**, 2501 (1998).

[9] H. B. Chan, V. A. Aksyuk, R. N. Kleiman, D. J. Bishop, and F. Capasso, Nonlinear micromechanical Casimir oscillator, Physical Review Letters **87**, 211801 (2001).

[10] W. Broer, G. Palasantzas, J. Knoester, and V. B. Svetovoy, Significance of the Casimir force and surface roughness for actuation dynamics of MEMS, Physical Review B **87**, 125413 (2013).

[11] L. Tang, M. Wang, C. Y. Ng, M. Nikolic, C. T. Chan, A. W. Rodriguez, and H. B. Chan, Measurement of non-monotonic Casimir forces between silicon nanostructures, Nature Photonics **11**, 97 (2017).

[12] A. Stange, M. Imboden, J. Javor, L. K. Barrett, and D. J. Bishop, Building a Casimir metrology platform with a commercial MEMS sensor, Microsystems and Nanoengineering **5**, 14 (2019).

[13] J. M. Pate, M. Goryachev, R. Y. Chiao, J. E. Sharping, and M. E. Tobar, Casimir spring and dilution in macroscopic cavity optomechanics, Nature Physics **16**, 1117 (2020).

[14] K. Y. Fong, H.-K. Li, R. Zhao, S. Yang, Y. Wang, and X. Zhang, Phonon heat transfer across a vacuum through quantum fluctuations, Nature **576**, 243 (2019).

[15] Z. Xu, X. Gao, J. Bang, Z. Jacob, and T. Li, Non-reciprocal energy transfer through the Casimir effect, Nature Nanotech-

nology **17**, 148 (2022).
[16] V. B. Bezerra, G. L. Klimchitskaya, V. M. Mostepanenko, and C. Romero, Violation of the Nernst heat theorem in the theory of the thermal Casimir force between Drude metals, Physical Review A **69**, 022119 (2004).
[17] J. S. Høye, I. Brevik, S. A. Ellingsen, and J. B. Aarseth, Analytical and numerical verification of the Nernst theorem for metals, Physical Review E **75**, 051127 (2007).
[18] A. O. Sushkov, W. J. Kim, D. A. R. Dalvit, and S. K. Lamoreaux, Observation of the thermal Casimir force, Nature Physics **7**, 230 (2011).
[19] V. M. Mostepanenko, Casimir puzzle and Casimir conundrum: Discovery and search for resolution, Universe **7**, 84 (2021).
[20] R. S. Decca, E. Fischbach, G. L. Klimchitskaya, D. E. Krause, D. López, and V. M. Mostepanenko, Improved tests of extra-dimensional physics and thermal quantum field theory from new Casimir force measurements, Physical Review D **68**, 116003 (2003).
[21] G. L. Klimchitskaya, U. Mohideen, and V. M. Mostepanenko, Constraints on non-Newtonian gravity and light elementary particles from measurements of the Casimir force by means of a dynamic atomic force microscope, Physical Review D **86**, 065025 (2012).
[22] U. Leonhardt, Liftshitz theory of the cosmological constant, Annals of Physics **411**, 167973 (2019).
[23] G. Bimonte, E. Calloni, G. Esposito, and L. Rosa, Variations of Casimir energy from a superconducting transition, Nuclear Physics B **726**, 441 (2005).
[24] D. Pérez-Morelo, A. Stange, R. W. Lally, L. K. Barrett, M. Imboden, A. Som, D. K. Campbell, V. A. Aksyuk, and D. J. Bishop, A system for probing Casimir energy corrections to the condensation energy, Microsystems and Nanoengineering **6**, 115 (2020).
[25] G. Bimonte, H. Haakh, C. Henkel, and F. Intravala, Optical BCS conductivity at imaginary frequencies and dispersion energies of superconductors, Journal of Physics A: Mathematical and Theoretical **43**, 145304 (2010).
[26] R. A. Norte, M. Forsch, A. Wallucks, I. Marinković, and S. Gröblacher, Platform for measurements of the Casimir force between two superconductors, Physical Review Letters **121**, 030405 (2018).
[27] J. R. Rodrigues, A. Gusso, F. S. S. Rosa, and V. R. Almeida, Rigorous analysis of Casimir and van der Waals forces on a silicon nano-optomechanical device actuated by optical forces, Nanoscale **10**, 3945 (2018).
[28] G. Bimonte, Casimir effect between superconductors, Physical Review A **99**, 052507 (2019).
[29] R. S. Decca, D. López, E. Fischbach, G. L. Klimchitskaya, D. E. Krause, and V. M. Mostepanenko, Tests of new physics from precise measurements of the Casimir pressure between two gold-coated plates, Physical Review D **75**, 077101 (2007).
[30] R. W. Andrews, A. P. Reed, K. Cicak, J. D. Teufel, and K. W. Lehnert, Quantum-enabled temporal and spectral mode conversion of microwave signals, Nature Communications **6**, 10021 (2015).
[31] F. M. Serry, D. Walliser, and G. J. Maclay, The anharmonic Casimir oscillator (ACO) - The Casimir effect in a model microelectromechanical system, Journal of Microelectromechanical Systems **4**, 193 (1995).
[32] H. B. Chan, V. A. Aksyuk, R. N. Kleiman, D. J. Bishop, and F. Capasso, Quantum mechanical actuation of microelectromechanical systems by the Casimir force, Science **291**, 1941 (2001).
[33] J. D. Teufel, T. Donner, D. Li, J. W. Harlow, M. S. Allman, K. Cicak, A. J. Sirois, J. D. Whittaker, K. W. Lehnert, and R. W. Simmonds, Sideband cooling of micromechanical motion to the quantum ground state, Nature **475**, 359 (2011).
[34] E. E. Wollmann, C. U. Lei, A. J. Weinstein, J. Suh, A. Kronwald, F. Marquardt, A. A. Clerk, and K. C. Schwab, Quantum squeezing of motion in a mechanical resonator, Science **349**, 952 (2015).
[35] J.-M. Pirkkalainen, E. Damskägg, M. Brandt, F. Massel, and M. A. Sillanpää, Squeezing of quantum noise of motion in a micromechanical resonator, Physical Review Letters **115**, 243601 (2015).
[36] F. Lecocq, J. B. Clark, R. W. Simmonds, J. Aumentado, and J. D. Teufel, Quantum nondemolition measurement of a nonclassical state of a massive object, Physical Review X **5**, 041037 (2015).
[37] C. F. Ockeloen-Korppi, E. Damskägg, J.-M. Pirkkalainen, M. Asjad, A. A. Clerk, F. Massel, M. J. Woolley, and M. A. Sillanpää, Stabilized entanglement of massive mechanical oscillators, Nature **556**, 478 (2018).
[38] S. Kotler, G. A. Peterson, E. Shojaee, F. Lecocq, K. Cicak, A. Kwiatkowski, S. Geller, S. Glancy, E. Knill, R. W. Simmonds, J. Aumentado, and J. D. Teufel, Direct observation of deterministic macroscopic entanglement, Science **372**, 622 (2021).
[39] L. Mercier de Lépinay, C. F. Ockeloen-Korppi, M. J. Woolley, and M. A. Sillanpää, Quantummechanics-free subsystem with mechanical oscillators, Science **372**, 625 (2021).
[40] R. Riedinger, S. Hong, R. A. Norte, J. A. Slater, J. Shang, A. G. Krause, V. Anant, M. Aspelmeyer, and S. Gröblacher, Nonclassical correlations between single photons and phonons from a mechanical oscillator, Nature **530**, 313 (2016).
[41] I. Galinskiy, G. Enzian, M. Parniak, and E. S. Polzik, Nonclassical correlations between photons and phonons of center-of-mass motion of a mechanical oscillator, Physical Review Letters **133**, 173605 (2024).
[42] A. D. O'Connell, M. Hofheinz, M. Ansmann, R. C. Bialczak, M. Lenander, E. Lucero, M. Neeley, D. Sank, H. Wang, M. Weides, J. Wenner, J. M. Martinis, and A. N. Cleland, Quantum ground state and single-phonon control of a mechanical resonator, Nature **464**, 697 (2010).
[43] Y. Chu, P. Kharel, T. Yoon, L. Frunzio, P. T. Rakich, and R. J. Schoelkopf, Creation and control of multi-phonon Fock states in a bulk acoustic-wave resonator, Nature **563**, 666 (2018).
[44] S. Marti, U. von Lüpke, O. Joshi, Y. Yang, M. Bild, A. Omahen, Y. Chu, and M. Fadel, Quantum squeezing in a nonlinear mechanical oscillator, Nature Physics **20**, 1448 (2024).
[45] Y. Yang, I. Kladarić, M. Drimmer, U. von Lüpke, D. Lenterman, J. Bus, S. Marti, M. Fadel, and Y. Chu, A mechanical qubit, Science **386**, 783 (2024).
[46] C. Samanta, S. L. De Bonis, C. B. Møller, R. Tormo-Queralt, W. Yang, C. Urgell, B. Stamenic, B. Thibeault, Y. Jin, D. A. Czaplewski, F. Pistolei, and A. Bachtold, Nonlinear nanomechanical resonators approaching the quantum ground state, Nature Physics **19**, 1340 (2023).
[47] H. J. Eerkens, *Investigations of radiation pressure: Optical side-band cooling of a trampoline resonator and the effect of superconductivity on the Casimir force*, phdthesis, Universiteit Leiden (2017), iSBN: 9789085933243, https://hdl.handle.net/1887/59506.
[48] M. Aspelmeyer, T. J. Kippenberg, and F. Marquardt, Cavity optomechanics, Reviews of Modern Physics **86**, 1391 (2014).
[49] T. J. Kippenberg and K. J. Vahala, Cavity opto-mechanics, Optics Express **15**, 17172 (2007).
[50] M. H. J. de Jong and L. Mercier de Lépinay, Simulating the

electrostatic patch force in sphere-plate and plate-plate geometries, https://arxiv.org/abs/2408.16323 (2024), arxiv preprint.
[51] M. A. Sillanpää, R. Khan, T. T. Heikkilä, and P. J. Hakonen, Macroscopic quantum tunneling in nanoelectomechanical systems, Physical Review B **84**, 195433 (2011).
[52] F. Pistolesi, A. N. Cleland, and A. Bachtold, Proposal for nanomechanical qubit, Physical Review X **11**, 031027 (2021).
[53] M. Tinkham, *Introduction to superconductivity* (McGraw-Hill, Inc., 1996).
[54] E. D. Palik, ed., *Handbook of optical constants of solids*, Vol. 1 (Academic, New York, 1997).
[55] T. H. K. Barron, J. F. Collins, T. W. Smith, and G. K. White, Thermal expansion, Grüneisen functions and static lattice properties of quartz, Journal of Physics C: Solid State Physics **15**, 4311 (1982).
[56] M. Pinard, Y. Hadjar, and A. Heidmann, Effective mass in quantum effects of radiation pressure, European Physical Journal D **7**, 107 (1999).
[57] A. Dhooge, W. Govaerts, and Y. A. Kuznetsov, MATCONT: a MATLAB package for numerical bifurcation analysis of ODEs, ACM Transactions on Mathematical Software **29**, 141 (2003).
[58] A. Dhooge, W. Govaerts, Y. A. Kuznetsov, H. G. E. Meijer, and B. Sautois, New features of the software MATCONT for bifurcation analysis of dynamical systems, Mathematical and Computer Modelling of Dynamical Systems **14**, 79 (2008).
[59] M. Xu, R. J. G. Elbertse, A. Keşkekler, G. Bimonte, J. Lee, S. Otte, and R. A. Norte, Measuring Casimir force across a superconducting transition, https://arxiv.org/abs/2504.10579 (2025), arxiv preprint.
[60] B. He, Q. Lin, M. Orszag, and M. Xiao, Mechanical oscillations frozen on discrete levels by two optical driving fields, Physical Review A **102**, 011503 (2020).
[61] P. Virtanen, R. Gommers, T. E. Oliphant, M. Haberland, T. Reddy, D. Cournapeau, E. Burovski, P. Peterson, W. Weckesser, J. Bright, S. J. van der Walt, M. Brett, J. Wilson, K. Jarrod Millman, N. Mayorov, A. R. J. Nelson, E. Jones, R. Kern, E. Larson, C. J. Carey, I. Polat, Y. Feng, E. W. Moore, J. VanderPlas, D. Laxalde, J. Perktold, R. Cimrman, I. Henriksen, E. A. Quintero, C. R. Harris, A. M. Archibald, A. H. Ribeiro, F. Pedregosa, P. van Mulbregt, and Scipy 1.0 Contributors, Scipy 1.0: fundamental algorithms for scientific computing in Python, Nature Methods **17**, 261 (2020).
[62] J. B. Camp, T. W. Darling, and R. E. Brown, Macroscopic variations of surface potentials of conductors, Journal of Applied Physics **69**, 7126 (1991).
[63] C. C. Speake and C. Trenkel, Forces between superconducting surfaces due to spatial variations of surface potential, Physical Review Letters **90**, 160403 (2003).
[64] J. Ke, W.-C. Dong, S.-H. Huang, Y.-J. Tan, W.-H. Tan, S.-Q. Yang, C.-G. Shao, and J. Luo, Electrostatic effect due to patch potentials between closely spaced surfaces, Physical Review D **107**, 065009 (2023).
[65] R. O. Behunin, F. Intravaia, D. A. R. Dalvit, P. A. Maia Neto, and S. Reynaud, Modeling electrostatic patch effects in Casimir force measurements, Physical Review A **85**, 012504 (2012).
[66] R. O. Behunin, Y. Zeng, D. A. R. Dalvit, and S. Reynaud, Electrostatic patch effects in Casimir-force experiments performed in sphere-plane geometry, Physical Review A **86**, 052509 (2012).
[67] R. O. Behunin, D. A. R. Dalvit, R. S. Decca, and C. C. Speake, Limits on the accuracy of force sensing at short separations due to patch potentials, Physical Review D **89**, 051301 (2014).
[68] J. L. Garrett, D. Somers, and J. N. Munday, The effect of patch potentials in Casimir force measurements determined by heterodyne Kelvin probe force microscopy, Journal of Physics: Condensed Matter **27**, 214012 (2015).
[69] W. M. Haynes, ed., *CRC Handbook of Chemistry and Physics*, 96th ed. (CRC Press, Roca Baton, 2015).
[70] K. Shi, P. Luo, J. Liu, H. Yin, and Z. Zhou, Dependence of electrostatic patch force evaluation on the lateral resolution of Kelvin probe force microscopy, https://arxiv.org/abs/2411.01733 (2024), arxiv preprint.
[71] G. Lévêque, P. Cadet, and A. Arinero, Sensitivity and resolution in noncontact electrostatic force microscopy in the case of a constant potential, Physical Review B **71**, 205419 (2005).
[72] J. L. Garrett, J. Kim, and J. N. Munday, Measuring the effect of electrostatic patch potentials in Casimir force experiments, Physical Review Research **2**, 023355 (2020).
[73] D. Cattiaux, S. Kumar, X. Zhou, A. Fefferman, and E. Collin, Geometrical nonlinearity of circular plates and membranes: An alternative method, Journal of Applied Physics **128**, 104501 (2020).
[74] D. Cattiaux, X. Zhou, S. Kumar, I. Golokolenov, R. R. Gazizulin, A. Luck, L. Mercier de Lépinay, M. Sillanpää, A. D. Armour, A. Fefferman, and E. Collin, Beyond linear coupling in microwave optomechanics, Physical Review Research **2**, 033480 (2020).

Dear editor,

We would like to thank the reviewer and you for reviewing our paper. We have copied comments below (in black) and added our response (in blue). The modifications brought to the paper are indicated in red in the revised version.

On behalf of the authors,
Laure Mercier de Lépinay

Comment from the editor:

Of particular interest was your response to Reviewer 3's request to soften the claim of "unambiguous observation of Casimir forces" into "power law attractive forces consistent with Casimir". We do appreciate that you have expanded the discussion ruling out patch potentials etc. However, given the available input from the reviewers (strong initial statements by Reviewer 3 and weak support for your response from Reviewer 1), we find a softening of claims to be prudent. We therefore request that you soften your claim according to the spirit of the initial request by Reviewer 3.

We understand this comment from reviewers and the editor. We apologize that our steps in this direction were not sufficient in the previous resubmitted version of our work. We have now taken all steps to present the association between the expected Casimir force and the measured dynamics as a working hypothesis. We have detailed a list of changes to this effect in our answer to the reviewer (below).

Comments from Reviewer 1:

The authors have in detail addressed all the points I raised with great care and adapted their manuscript accordingly. I also very much appreciate that the authors included new data for a second device with a similar gap size that corroborates the findings of the work.

There is one important point, however, which I realized after having read the revised version of the manuscript. I kindly ask the authors to address this point as it regards the validity of their model for the optomechanical equations of motion. Equation (1) of the main text describes the dynamics of the mechanical system including the Casimir nonlinear force. Equations (2) of the main text describe the coupled optomechanical equations of motion, which include the coupling of the mechanical resonator to the optical intracavity field. However, the mechanical evolution in Equation (2) is harmonic and the nonlinear Casimir force term is neglected. This modelling is inconsistent with the assumption of Eqn. (1) and also with the measurements the authors perform as they drive the mechanical resonator to a regime, where clear nonlinear effects of the mechanics are observed (e.g., Fig 1c,d). Even if the authors use the 'perturbed' mechanical frequency ω_m in these equations, the underlying dynamics of the mechanics must be assumed to be nonlinear, in particular, when driven strongly, as the authors do. Hence, currently there appears to be an inconsistency in the theoretical modeling of the system, which should be alleviated before the manuscript can be recommended for publication.

The reviewer is right about equation 2: it cannot reproduce nonlinear mechanical responses since it does not include a nonlinear force term. However, the "mechanical" equations (first two lines) of this system are only used in small-displacement situations throughout the paper. Precisely, equation 2 has been used:

- For the calibration of measured responses into displacements, which comes down to a calibration of the actual drive powers at the device with respect to the drive powers issued by generators. In this calibration, data and results of simulations using Eq. (2) (that is, the full system, including mechanical equations) were compared for all drive powers, but the matching of data and simulation was only required for small powers, as can be seen in Fig. S3, or for off-resonant and therefore small displacement, as in Fig. S4. As can be seen in Fig. S3, the values resulting from the calibration allow to match at least all data and simulations for which both drive powers were in the range $[-40\,\mathrm{dB}, -30\,\mathrm{dB}]$, which is the range for which mechanical responses were approximately Lorentzian and therefore reasonably well described by Eq. (2). We realized that this point was not clear in the description of the calibration in the paper: we have extensively rephrased it in the paper and in the Supplementary Materials.

- For the correction of the drive efficiency, that is, to calculate the effect of the back-action of the mechanical displacement on the cavity in order to ascribe a value to F_0 in Eq. (1) when fitting mechanical responses. However, only the last line of Eq. (2) describing the evolution of the cavity field amplitude was solved with a fixed mechanical amplitude x to obtain a corrective factor to F_0. The first two equations (evolution of the mechanical oscillator) are not solved here and the calculation of the drive efficiency is agnostic to the type of displacement (e.g. linear or nonlinear oscillator) that x represents in the 3rd line of Eq. (2).

- As the origin of the expansion into higher scattering orders (Eq. (3)). However, again, this expansion comes entirely from the third line of Eq. (2), with very little requirement on x. We have precised this point as well as the requirements on x in the corresponding section of the Supplementary Materials ("Relative sideband powers"): "This expansion is valid regardless of the spectrum of x_{amp}: it simply requires that it is peaked close to 0 frequency and sufficiently narrow so that the sidebands are well-separated."

Since the first two lines of Eq. (2) are only used in the calibration, we removed them from the main text and left them only in Eq. (S1) in the section of the Supplementary Materials where the calibration procedure is detailed. Furthermore, we decided to perform the following modifications in order to simplify these equations:

- we have removed the noise terms in Eq. (2) and Eq. (S1) since their impact is absolutely negligible in this paper

- we have written these equations in classical formalism since the degrees of freedom considered here are very far form the quantum regime. In practice, mostly, we removed the hats on operators to consider them as scalars. We have introduced a displacement $\tilde{x}$, to replace $\hat{x}$ to represent a small displacement in the minimum of potential (x is centered around $\sim -2.9\,\mathrm{nm}$ so that symbol could not be used to replace $\hat{x}$).

Further, as a minor remark, I would encourage the authors to clarify the use of the term 'optomechanical' nonlinearity, which is ambiguous as there are different types of 'optomechanical' nonlinearities acting: (i) the intrinsic non-linearized optomechanical Hamiltonian is nonlinear (ie, radiation-pressure interaction), (ii) the coupling strength is assumed to be linear in displacement, but higher order expansions are nonlinear in displacement (see Eq. (S24)), (iii) the cavity frequency spectral response is nonlinear (see, e.g., https://doi.org/10.1103/PhysRevLett.131.053601). Could the authors explain more clearly to which effect(s) they refer to?

Here, in spite of very strong actuations, the estimated displacement remains two orders of magnitude smaller than the vacuum gap of the drum resonator at the very highest displacement amplitudes explored in the paper. Therefore, we do not expect that effects from higher-order optomechanical couplings (ii) are very significant. The cavity has also been found to respond linearly to signals up to the largest amplitudes at which it was driven in this experiment (iii). The "optomechanical nonlinearity" to which we ascribe the presence of multiple sidebands in the signal reflected on the cavity corresponds to (i) the intrinsic nonlinearity of the optomechanical Hamiltonian: the mechanical displacement mediates a coupling between the component of the cavity field a at frequency ω and at frequency $\omega \pm \omega_m$, etc. This model accurately captures the multiple measured sidebands.

In the paper, to avoid the ambiguity

- we renamed the paragraph entitled "The optomechanical nonlinearity" into "Higher-order sidebands scattering"
- we replaced the comment "The optomechanical interaction is nonlinear." introducing that paragraph by "The optomechanical interaction is intrinsically nonlinear and it is here driven by large cavity fields and mechanical amplitudes." and followed it by an explanation: "As a result, scattering between sidebands assisted by the mechanical displacement yields multiple equally-spaced peaks in the observed response."
- we removed the conclusion of that paragraph "This shows that although the higher-order peaks arise from a nonlinear optomechanical effect, [...]" because the expression "the higher-order peaks arise from a nonlinear optomechanical effect" was too vague.

Furthermore, while reviewing the aspects of the paper linked to the optomechanical nonlinearity, we have realized that the estimates of the higher-order optomechanical couplings in the SI where made using the hypothetical $d = 18\,\mathrm{nm}$ vacuum gap rather than the physically realized gap $d' = 15\,\mathrm{nm}$ and have corrected the values given in the corresponding section.

I have read through the criticism of reviewers 2 and 3 and the author's reply to that criticism. In case of Reviewer 2, the authors have addressed all the comments in a sufficient manner - to the best of my knowledge. Also, Reviewer 2 was in general very positive to the work.

The authors have also replied to the comments of Reviewer 3.

In that case, I would, however, like to recommend that the authors make an additional change to their manuscript concerning the point of the discussion on "van der Waals and Casimir forces are generally defined as limit cases of the dispersion force". Though this point is discussed in the reply to the reviewer, the discussion is missing in the revised manuscript. However, I believe that this discussion would be necessary to show to the reader.

We have included an explanation of the reference to the force as the Casimir force in connection to the introduction of the power law, that is, in the paragraph after Eq. (1), since the Lifshitz formalism predicts both this power law and the crossover between regimes. We have added a section in the Supplementary materials which is identical to our discussion with Reviewer 3 on this point.

Finally, Reviewer 3 asks the authors to soften their claim from "unambiguous observation of Casimir forces" into "power law attractive forces consistent with Casimir". This request has not been adhered to. Instead, the authors argue that they took all possible other effects into consideration and concluded that the experimental data is only consistent with the Casimir force. This being said could, of course, not rule out an yet unknown other effect.

We have softened the claim as asked with the following changes:

- In the abstract: "Here, we observe the Casimir force between superconducting objects [...]" was replaced by "Here, we observe a force applied on a superconducting drum resonator [...]. The measured dynamics points to an extremely intense force found to be compatible in magnitude with the Casimir force, and incompatible with estimates of other known sources of nonlinearity." The rest of the abstract was somewhat shortened to match the word count requirement.
- Also in the abstract "The Casimir nonlinearity is intense enough that" was replaced by "This nonlinearity [...]".
- We have renamed the first subsection under the Result section: it was "The Casimir nonlinearity" and it is now "The nonlinear dynamics"
- We have rewritten a substantial part of this first subsection to avoid presenting values inferred from the model of the Casimir force upfront. We have regrouped all mentions of the Casimir force model for the nonlinear potential under a second subsection "A Casimir force model". In this new subsection we present the model, explain how it is used to fit experimental values and give the values of parameters thereby inferred from the model, then we comment on the compatibility of these values and of that of the total force with independent simulations and estimations.
- A new sentence in "A Casimir force model" motivates the Casimir force model: "A reasonable candidate to explain the strong nonlinearity is the Casimir effect [...], which is expected to be intense in these devices given their small vacuum gap values ($15 - 50\,\mathrm{nm}$), relatively large surfaces and high susceptibilities."
- In the same idea (allowing for easy identification of parameters that were inferred from the Casimir force model), we have annotated the parameters in Table 1 with asterisks to identify those that come from the design, those that are calibrated using standard optomechanical procedures and those whose estimation comes from the application of a model on the nonlinear signatures (the Casimir model).
- Caption of Fig. 1: the title "Effects of a Casimir force on a superconducting drum resonator" was changed into "Effects of a strong nonlinear potential on a superconducting drum resonator". Furthermore, in the caption of subfigure a, the blue line formerly identified as "the Casimir potential" is now identified as "The nonlinear potential".

- Caption of Fig. 3c "The drive efficiency leads to a correction in the Casimir curves at large amplitudes" was replaced by "[...] a correction of the simulated response curves [...]"
- In the Discussion section, end of first paragraph, we have softened the claim "To the best of our knowledge, there are no other sources of nonlinearity that could mimic the Casimir force in both amplitude and scaling" into "We have not found another source of nonlinearity that could mimic the effect of the Casimir force in this device and consider it to be a strong candidate to explain the observations."
- In the 2nd paragraph of the Discussion section, we suggest that the electrostatic tuning of the separation allows to tune "the Casimir force", and have now added "or nonlinear potential".
- Last paragraph of the Discussion section: we replaced "In summary, we have shown the effect of a likely Casimir force between superconducting plates, through its nonlinear nature." with "In summary, we have observed strongly nonlinear dynamics of a superconducting membrane compatible with the existence of a Casimir potential between superconducting plates." and we have added "We have shown that this effect does not seem to correspond to other known sources of nonlinearity." To compensate for added text, we have shortened the following paragraph a bit, removing comments already made elsewhere in the paper.
- Further down: "Due to the exceptionally small spacing, a vacuum gap of 15 nm, the Casimir force in this configuration is much larger than in conventional Casimir experiments": we have removed "a vacuum gap of 15 nm" as this is the value predicted assuming the Casimir model (although it is supported by independent simulations). The gaps are exceptionally small in these devices in any case so the sentence remains true without assuming that the potential is a Casimir potential. We have also replaced "is much larger" with "is expected to be much larger" to reflect the fact that the estimation of the force requires to use a model for it.
- Further down: "This makes our system well-suited to accurately probe the remaining uncertainties around the Casimir force" was softened into "This suggests that our system is well-suited [...]"
- Further down: "More fundamentally, the strength of the Casimir effect in our experimental setup gives unique access to an extremely strong nonlinearity" was replaced by "More fundamentally, our experimental setup gives unique access to an extremely strong nonlinearity"
- Further down: "Furthermore, the competition between the Casimir potential and the elastic potential" was replaced by "Furthermore, the competition between the nonlinear potential and the elastic potential"
- The Methods section entitled "The Casimir oscillator" was renamed "Simulations of the dynamics in a Casimir potential" for clarity
- Caption of Fig. S22: "Measurement of the Casimir nonlinearity in a second device" was replaced by "[...] of the nonlinearity", and "The measured Casimir curve" was replaced by "The measured response"

Other typos we discovered

- Equation 10 (phenomenological model for the superconducting gap): the square-root symbol extended all the way to the end of the equation while it was supposed to stop before the parenthesis
- There was an irrelevant sign mistake in Eq. (S1) (it was written $-\sqrt{\kappa_{\mathrm{e}}}s_{\mathrm{in}}(t)$ instead of $+\sqrt{\kappa_{\mathrm{e}}}s_{\mathrm{in}}(t)$ which was inconsistent with previous equations.)
- Another square-root symbol extended too far in an occurrence of $\sqrt{\kappa_e}\hat{a}_{\mathrm{in}}$ above Eq. (S17).
- We have corrected a few grammar/spelling typos in the SI.

Measurement of the Casimir force between superconductors

Matthijs H. J. de Jong,[1] Evren Korkmazgil,[1] Louise Banniard,[1] Mika A. Sillanpää,[1] and Laure Mercier de Lépinay[1, *]

[1]Department of Applied Physics, Aalto University, FI-00076 Aalto, Finland

(Dated: May 6, 2026)

The Casimir force follows from quantum fluctuations of the electromagnetic field and yields a nonlinear attractive force between closely spaced conductive objects. Measuring the Casimir force in superconducting materials on either side of the transition should allow to isolate the specific contribution of low frequencies to the Casimir effect. There is significant interest in this contribution as it is suspected to be involved in an unexplained discrepancy between predictions and measurements of the Casimir force between normal metals. Here, we observe a force acting on a superconducting drum resonator integrated in a microwave optomechanical cavity through the nonlinear dynamics this force imparts to the resonator. The measured dynamics points to an extremely intense force found to be compatible in magnitude with the Casimir force for the range of vacuum separations that can be expected in this device, and incompatible with estimates of other known sources of nonlinearity. This nonlinearity is intense enough that, with a modified design, this device type should operate in the single-phonon nonlinear regime. Accessing this regime has been a long-standing goal that would greatly facilitate quantum operations of mechanical resonators.

INTRODUCTION

A significant body of theoretical and experimental works over the last 20 years has focused on understanding the Casimir force[1–7]. This is motivated in part by the Casimir effect's practical applications in MEMS[8–13], but to a larger extent by its intimate connection to heat and energy transfer[14,15], especially at finite conductivity and temperature[16–19]. Furthermore, Casimir force experiments have also put bounds on Yukawa corrections to short-distance Newtonian gravity[20,21] and the Casimir effect has been proposed as a candidate to account for dark energy in cosmology[22]. Recently, the interplay between the Casimir force and superconductivity has garnered interest, either manifesting as a correction to the superconducting condensation energy[23,24], or as a correction to the electric permittivity of the material[25–28]. Studies of this interplay could shed light on the discrepancy between the calculated and experimentally observed Casimir force between real metals at finite temperature[19,28,29]. While most room-temperature experiments rely on a variation of the distance between objects to observe the expected force-distance scaling[3,4,11,12,30], it is challenging to perform this type of experiment with superconductors due to the difficulty of precise positioning in cryogenic environments. By contrast, the strong nonlinearity imparted by the Casimir potential can be easily shown through the dynamical behavior of an oscillator without relying on precise positioners. Only few works have studied the Casimir force through the nonlinear dynamics[31,32].

Strong nonlinearities in oscillators at cryogenic temperatures are especially interesting in the context of resonators in the quantum regime. Cavity optomechanics, where the motion of an object couples to the electromagnetic field of a cavity, has allowed to engineer Gaussian quantum mechanical states in cryogenic mechanical oscillators. Notably, resonators were cooled to the ground state[33], their uncertainty was squeezed below the magnitude of quantum fluctuations[34–36], entangled states of two oscillators were prepared[37,38], and mechanical states were measured avoiding quantum backaction[39]. However, linear optomechanical systems cannot realize non-Gaussian quantum states such as Fock states, cat states, and entangled combinations thereof, which are desirable for quantum algorithms. To realize these states nonetheless, mechanical oscillators have been addressed with non-Gaussian photonic states[40,41], or coupled to superconducting qubits[42–45] or quantum dots[46] to inherit their nonlinearity. In contrast, the nonlinearity imparted by the Casimir force to a superconducting drum resonator is intrinsic to the construction of the system and does not rely on coupling to another system.

In this work, we have observed a nonlinear potential that we show to be quantitatively compatible with the Casimir potential acting between the plates of a type-I superconducting drum. This force force yields a strong softening nonlinearity, where the resonating frequency decreases with increasing amplitude[9,31,32]. The optomechanical coupling to a microwave cavity allows us to calibrate all properties of the system and compare its response to that obtained within a model of Casimir potential with only a single fit parameter. We qualitatively and quantitatively exclude other (nonlinear) effects that have hindered earlier works[26,30,47]. This system requires no cryogenic positioners, and it shows a strong, tunable mechanical nonlinearity that is fully compatible with a mechanical system where quantum operations have been achieved.

RESULTS

The nonlinear dynamics

Here, we describe the experimental system. The drum resonator consists of two plates made of evaporated aluminium. The top plate is suspended and forms a harmonic oscillator of frequency ω_r: the minimum of the harmonic mechanical potential would correspond to a vacuum gap of d. However, observations detailed below indicate that the oscillator is subject to a very strong nonlinear attractive potential. Such a potential is expected to draw the mechanically compliant top

* laure.mercierdelepinay@aalto.fi

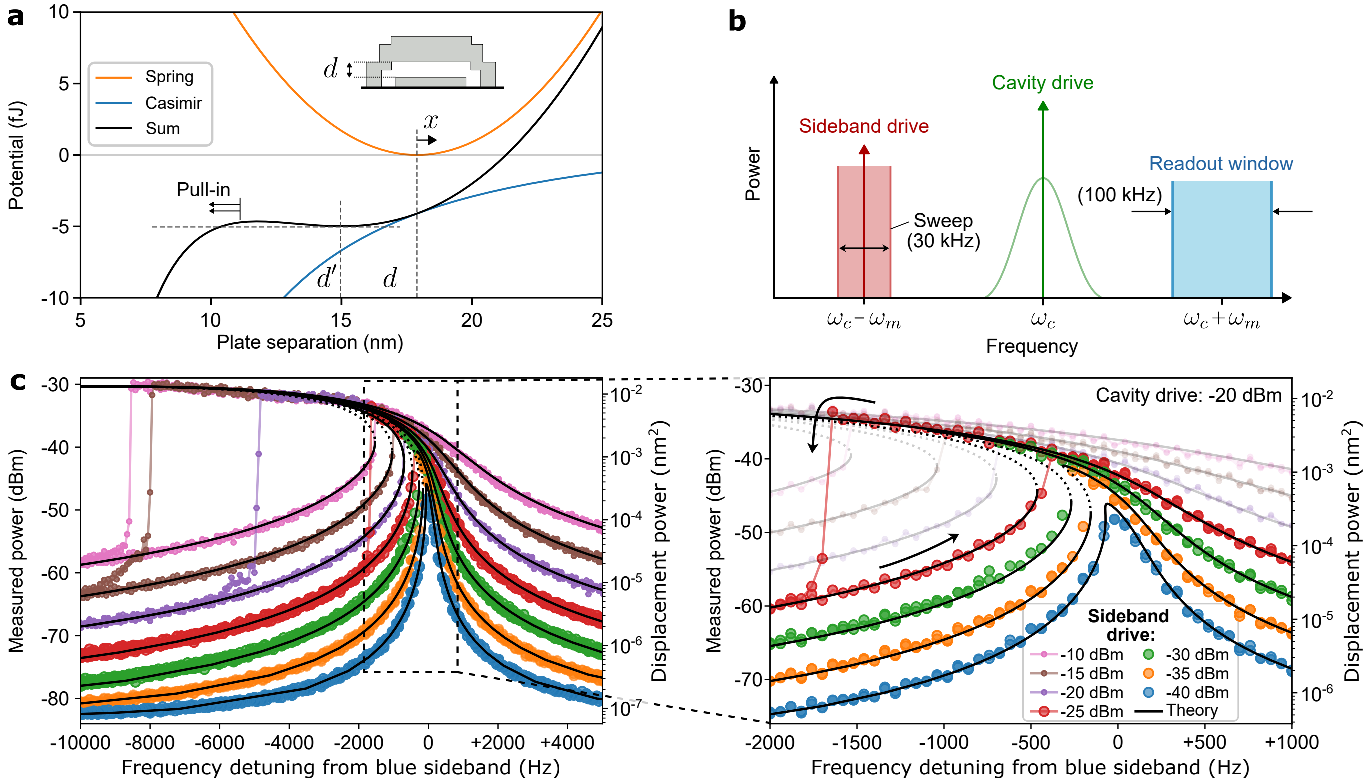

Fig. 1 | Effects of a strong nonlinear potential on a superconducting drum resonator. **a**: Our device consists of two plates separated by a vacuum gap. The top plate is mechanically compliant and experiences a mechanical restoring potential (orange line) which is minimum for a separation d between plates (see inset). The nonlinear potential (blue) adds to this restoring potential, and the sum (black) has a local minimum at separation d' shifted from d. The total potential is not harmonic around d' for large amplitudes which causes nonlinear behavior. **b**: Schematic of the microwave optomechanical measurement scheme. We strongly drive the microwave cavity at its center frequency, with an additional strong drive tone at ω_{sb} which is close to $\omega_{\mathrm{c}} - \omega_{\mathrm{m}}$. The sideband drive is swept in frequency, and we read out the emitted signal in a window around $\omega_{\mathrm{c}} + \omega_{\mathrm{m}}$. **c**: Measured displacement response for various nominal sideband drive powers (labels) at −20 dBm cavity drive, showing the expected Lorentzian behavior at low drive power that transitions to a strong softening nonlinearity at high drive power. The Casimir force model (black line) becomes multi-valued, with two stable branches (solid black) and an unstable solution (dotted black/semitransparent). Our measurements follow the stable solutions, leading to a hysteresis depending on the sweep direction. The theory matches well to all curves using only a single fit parameter, d, common to all curves. The right panel highlights details of the center region indicated by the dashed box, and the hysteresis depending on the sweep direction is indicated by arrows. The data points at the highest powers are made transparent for visual clarity.

plate closer to the bottom plate that is fixed to a rigid substrate, modifying the vacuum gap to a new value d', which we schematically show in Fig. 1a. Furthermore, the frequency of oscillations around this local potential minimum is expected to be lowered by the nonlinear potential: we denote ω_m the value of the softened frequency. Modified gap d' and frequency ω_m are the parameters physically realized by the device since the nonlinear potential exists throughout all experiments, and parameters d and ω_r, that concern a hypothetical situation where the drum would not be subject to a nonlinear potential, are only introduced as convenient modelling intermediates. The oscillator is expected to stably oscillate at ω_m around its local potential minimum with a small amplitude, but at larger amplitudes the frequency is expected to decrease (spring softening) until it reaches the pull-in point, beyond which the top plate would collapse onto the bottom plate[8,27].

The drum resonator is mounted in a dilution cryostat and stabilized at 10 mK (see Methods), so the aluminium is deep in the superconducting regime. The drum forms the variable capacitance of a microwave cavity, which we drive with two strong drives, one at the resonance frequency of the microwave cavity, ω_{c} (cavity drive), and the other at the red sideband $\omega_{\mathrm{c}} - \omega_{\mathrm{m}}$ (sideband drive) as shown schematically in Fig. 1b. This combination of tones generates a driving force on the mechanical resonator such that the mechanical amplitude scales linearly with either drive power (see Supplementary Sec. B). All drive powers are reported as their nominal values at room temperature, they are divided by attenuators before reaching the sample as shown in Methods. The cavity drive power is much larger than the sideband drive, and we sweep the frequency of the weaker sideband drive within a range of 30 kHz both upwards and downwards in frequency. We record the output signal of the cavity with a spectrum analyzer over a window centered around $\omega_{\mathrm{c}} + \omega_{\mathrm{m}}$ (blue sideband).

The signal we observe at the readout sideband is proportional to the displacement of the resonator. At low drive pow-

Quantity	Symbol	Value
Unperturbed mech. frequency**	ω_r	$2\pi \times 16.247$ MHz
Mechanical frequency*	ω_m	$2\pi \times 10.001$ MHz
Mechanical linewidth*	$\gamma_r \simeq \gamma_m$	$2\pi \times 168.9 \pm 9.5$ Hz
Cavity frequency*	ω_c	$2\pi \times 5.461831$ GHz
External linewidth*	κ_e	$2\pi \times 250.8 \pm 2.1$ kHz
Internal linewidth*	κ_i	$2\pi \times 297.2 \pm 2.8$ kHz
Drive frequency	ω_{mw}	$\simeq \omega_c$
Sideband frequency*	ω_{sb}	$\simeq \omega_{mw} - \omega_m$
Detuning $\omega_c - \omega_{mw}$	Δ	$< \lvert 2\pi \times 1 \rvert$ kHz
Optomechanical coupling*	g_0	$2\pi \times 150 \pm 9$ Hz
Effective mass	m_{eff}	3.96×10^{-14} kg
Vacuum gap w/o Cas. force**	d	18.00 ± 0.25 nm
Vacuum gap**	d'	15.10 ± 0.25 nm
Bottom plate diameter	$2r$	11.3 µm
Moving plate diameter	-	14.5 µm
Casimir pressure at rest**	P_c	12.0 ± 0.6 kPa
Casimir force amplitude**	P	$(1275 \pm 7) \cdot 10^{-24}$ Pa m^n
Cas. force scaling exponent**	n	3.193

Table 1 | The parameters of the system either from design, calibrated at small mechanical amplitudes using optomechanical models (*), or estimated within the Casimir force model (**). Intervals represent 95% confidence.

ers, we see a Lorentzian response compatible with a mechanical resonance frequency $\omega_m \simeq 10.0$ MHz, but increasing the cavity drive power in Fig. **1c** shows a strong softening nonlinearity. At high drive powers, this nonlinearity creates two stable solutions to Eq. (1) over a limited range of frequencies (a low-amplitude and a high-amplitude branch) with an unstable solution in between. The sweep direction determines which branch is followed as indicated by arrows in Fig. **1c**. The resonator amplitude jumps up at the end of the low-amplitude branch (bifurcation point), but it jumps down from the high-amplitude branch at a point before the end of the branch. This occurs due to our stepped sweep protocol (see Methods).

A Casimir force model

A reasonable candidate to explain the strong nonlinearity is the Casimir effect[9], which is expected to be intense in these devices given their small vacuum gap values (15 – 50 nm), relatively large surfaces and high susceptibilities. As explained further below, a model for the dynamics of the oscillator in presence of the Casimir force is

$$\ddot{x} + \gamma_r \dot{x} + \omega_r^2 x + \frac{P}{(x+d)^n} \frac{\pi r^2}{m_{eff}} = \frac{F_0}{m_{eff}}, \tag{1}$$

which describes the evolution of a point-like harmonic oscillator in one dimension with displacement coordinate x, resonance frequency ω_r, effective mass m_{eff}, and decay rate γ_r, optomechanically driven by a force F_0. It is additionally subject to a force derived from the Casimir pressure, the last term on the left-hand side, that works on the area of the drum, πr^2. This model reducing the distributed motion of the membrane to a scalar coordinate with an effective mass stays roughly valid in presence of a nonlinear potential. We compute the Casimir pressure for the real material based on the Mattis-Bardeen conductivity for (BCS) superconductors[28], see Methods. From these computations, the Casimir force would have an expression of the form $P_c = \frac{P}{(x+d)^n}$ where $P \simeq 1275 \cdot 10^{-24}$ Pa $\cdot$ m^n and pressure-distance scaling $n = 3.193$. This power law is the one predicted by the Lifshitz formalism in the range of separation gaps of the device. The use of this power law here, as well as the reference to the Casimir force rather than the van der Waals force, is motivated by the fact that the order of magnitude of the plates separation is larger than the threshold separating the Casimir regime from the van der Waals regime where retardation effects are negligible (see Supplementary Sec. A for more details).

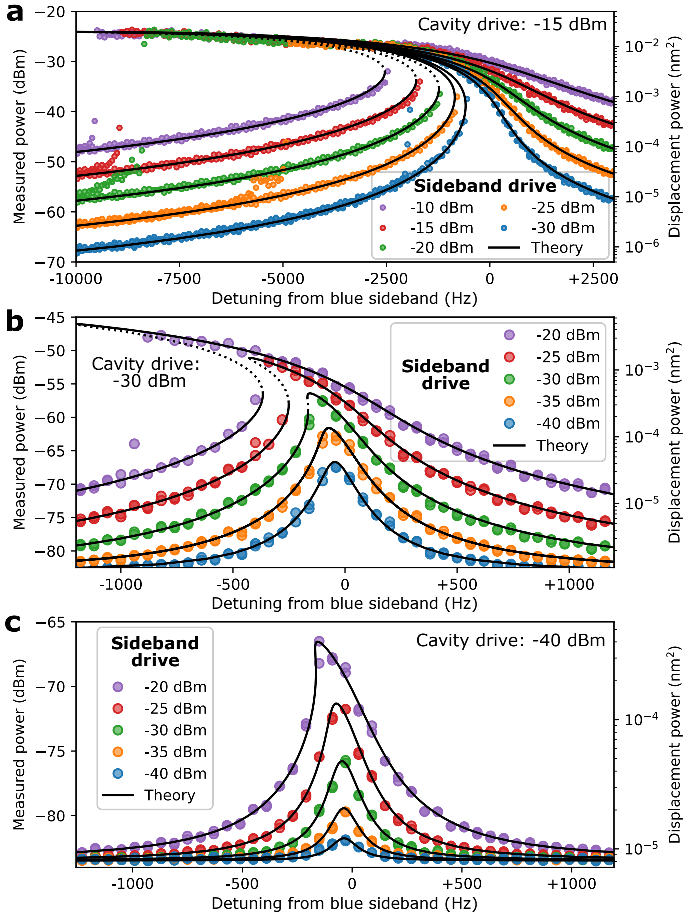

Fig. 2 | Responses measured for all combinations of drive parameters for cavity drive powers (**a**: −15 dBm, **b**: −30 dBm, **c**: −40 dBm) and sideband drive powers (colors). All theory curves (black lines) across all panels share only a single fit parameter d.

We compute the expected displacement of the oscillator of Eq. (1) for a frequency-swept drive (see Methods and Supplementary Information) using the parameters of Table **1**, and adjust a single parameter, d, to collectively fit all measured mechanical responses. The resulting curves are plotted as black lines in Fig. **1c**, with the unstable part of the solution represented as a dotted line. This procedure yields an estimate of the hypothetical unperturbed gap $d = 18$ nm, giving an excellent agreement for all measured data simultaneously. We repeat the experiment and analysis at different combinations of cavity and sideband drive powers, shown in Fig. 2: the same model and fit parameter accurately describe the shape of the signal across more than three orders of magnitude in displacement, up to a maximum measured amplitude of $\simeq 100$ pm.

Within this modelling, the shifted equilibrium position of the oscillator is $d' = 15.10 \pm 0.25$ nm, corresponding to a static pull $x = d' - d \simeq -2.9$ nm under the nonlinear potential. The inferred physical gap d' is of the expected order of magnitude for this device. The value of the unperturbed gap d is furthermore in very good agreement with independent simulations of the shape of the membrane cooled to cryogenic temperature in absence of a nonlinear potential (see Methods). The unperturbed mechanical frequency ω_r is furthermore found to be $\omega_r \simeq 16.2$ MHz within this model, which is also in good agreement with models of the membrane, indicating a nonlinear softening larger than 6 MHz to obtain the physical frequency $\omega_m \simeq 10.0$ MHz. The total pressure exerted on the membrane at rest is estimated to be as high as $P_c \simeq 12.0 \pm 0.6$ kPa, which leads to the considerable static displacement and frequency pull modelled.

Calibration of displacement amplitude

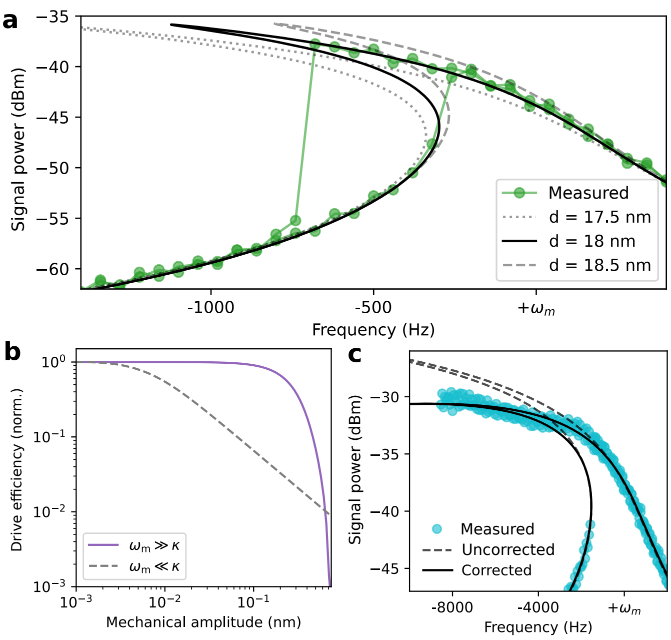

Fig. 3 | Optomechanical calibration. **a**: Theory curves generated with equal maximum mechanical amplitude for various values of d (black & grey lines). For smaller d, the Casimir force is stronger and leads to a larger softening nonlinearity. For $d = 18$ nm there is excellent agreement with the measured data (green). **b**: The drive efficiency decreases sharply from 1 at high amplitude, as most of the time the instantaneous cavity frequency $\omega_c(t)$ is far away from the drive frequency. This effect is stronger, comparatively, in the bad cavity limit ($\omega_m \ll \kappa$), but it is noticeable in our experiments at the largest amplitudes. **c**: The drive efficiency leads to a correction of the simulated response curves at large amplitudes.

To make d (the vacuum gap at the minimum of the harmonic mechanical potential) the only fit parameter, we calibrate all other parameters listed in Table 1 to accurately infer the displacement amplitude of the resonator. The drum resonator is embedded in an optomechanical cavity such that its position couples to the radiation pressure. The equation of evolution for the cavity field is [48]

$$\dot{a}(t) = -(i\Delta + \kappa/2)a + ig_0\tilde{x}a + \sqrt{\kappa_e}\, s_{in}(t). \tag{2}$$

Here, $\tilde{x}$ represents the displacement around the equilibrium position shifted by the nonlinear potential and a is the cavity field amplitude. We work in a frame rotating at the frequency of the cavity drive, which is detuned by Δ from the cavity resonance frequency. The cavity linewidth $\kappa = \kappa_e + \kappa_i$ is the sum of the external and internal decay rates (see Table 1). The optomechanical single-photon coupling is g_0. The input coherent signal is modelled by s_{in}. The mechanical and cavity noise are negligibly small compared to driven amplitudes in this problem and we exclude them from the description.

The equation of motion, Eq. (2), depends on parameters g_0, κ, and Δ. To calibrate the measured signal into a displacement, we complete this equation with the small-displacement motion equations around the equilibrium position (see Supplementary Information), which additionally depend on ω_m and γ_m the mechanical parameters in the local minimum of potential. We first extract cavity parameters κ_e and κ_i from the cavity reflection response, and get the single-photon coupling g_0, the mechanical parameters ω_m, γ_m and the power at our detector from a given displacement power from the measurement of thermal motion of the drum resonator at 10 mK (see separate Supplementary Information section on these preliminary calibrations). Then, using these independently calibrated values, we use a numerical solution of the equations of motion to calibrate the ratios between the powers of the tones at the output of generators and incoming on the device. These powers enter into $s_{in}(t)$ in Eq. (2): they determine the driving force F_0 in model (1) and thereby the driven mechanical amplitude. The numerical solution for the cavity signal at the first two sidebands (red and blue) is matched to the measured signal by adjusting the power ratios, completing the calibration.

Parameters P and n are related to material parameters for aluminium for which we can obtain a high accuracy (see Methods). This makes d the sole fit parameter to compare the solution of Eq. (2) to our experimental observations. In Fig. 3a, we show that $d = 18$ nm generates the best-fitting solution. Also solutions with $d = 17.5$, 18, and 18.5 nm are overlaid on experimental data obtained at −20 dBm cavity drive and −30 dBm sideband drive. The fit procedure is applied to all measured response signals (see Fig. 2). From this collective fit, we estimate the uncertainty of d as the upper bound of the uncertainty propagated from the amplitude calibration and the standard error of the fitted response signal. The uncertainty we find this way is larger than the uncertainty in d we would have found from variations in parameters P and n, which motivates our choice to treat them as fixed values.

Drive efficiency

At the core of Eq. (2) is the notion that the cavity frequency depends on the mechanical position, $\omega_c(x)$. For a large enough displacement amplitude x, the cavity frequency shifts by more than the cavity linewidth κ such that the cavity drive tone is mostly reflected. This reduces the amount of circulating power in the cavity, and it reduces the effectiveness of the drive on the mechanical resonator. We estimate this loss of efficiency and compensate for it in the following way. We define the 'drive efficiency' as the circulating power in the cavity at some mechanical amplitude normalized to the power at low displacement. It is straightforward to calculate by solving Eq. (2) for fixed amplitude of mechanical motion, and the results are plotted in Fig. **3b**. In the experiment $\omega_m \gg \kappa$ so the drive efficiency is close to 1 up to $\sim$ 100 pm and strongly decreases beyond that.

The effect of the drive efficiency is shown in Fig. **3c**. For the frequencies where the mechanical amplitude is small, the uncorrected and corrected curves overlap since the drive efficiency is 1. At large amplitudes the uncorrected prediction overestimates the measured response (-20 dBm cavity drive and -10 dBm sideband drive).

Higher-order sidebands scattering

The optomechanical interaction, Eq. (2), is intrinsically nonlinear and it is here driven by large cavity fields and large mechanical amplitudes. As a result, scattering between sidebands assisted by the mechanical displacement yields multiple equally-spaced peaks in the observed response. We read out six of these sidebands, at $\omega_c \pm n \times \omega_m$ ($n = 1,\ 2,\ 3$), as shown in Fig. **4a**. The higher-order sidebands can be viewed as repeated scattering events. We extend classical scattered mode theory[49] to cover all six sidebands. We write the system of linear coupled equations for the classical field amplitudes a_n at the corresponding frequency components in matrix form,

$$\begin{bmatrix} 1 & d_{+3} & 0 & 0 & 0 & 0 & 0 \\ d_{+2} & 1 & d_{+2} & 0 & 0 & 0 & 0 \\ 0 & d_{+1} & 1 & d_{+1} & 0 & 0 & 0 \\ 0 & 0 & d_0 & 1 & d_0 & 0 & 0 \\ 0 & 0 & 0 & d_{-1} & 1 & d_{-1} & 0 \\ 0 & 0 & 0 & 0 & d_{-2} & 1 & d_{-2} \\ 0 & 0 & 0 & 0 & 0 & d_{-3} & 1 \end{bmatrix} \begin{bmatrix} a_{+3} \\ a_{+2} \\ a_{+1} \\ a_0 \\ a_{-1} \\ a_{-2} \\ a_{-3} \end{bmatrix} = \begin{bmatrix} 0 \\ 0 \\ 0 \\ \frac{a_{\mathrm{mw}}\sqrt{\kappa_e}}{-i\Delta+\kappa/2} \\ 0 \\ 0 \\ 0 \end{bmatrix} \tag{3}$$

with

$$d_{\pm n} = \frac{g_0 x_{\mathrm{amp}}}{2x_{\mathrm{zpf}}} \frac{1}{-i(\Delta \pm n\omega_{\mathrm{m}}) + \kappa/2}. \tag{4}$$

Here a_{mw} is the input power of the microwave drive at the cavity frequency, a_{sb} is the input power of the microwave drive at the red sideband. We cut off the scattering processes above order $|n| = 3$, retaining 7 frequency ranges in Eq. (3). This is a valid approximation when $g_0 \ll \kappa/2$, since each individual photon is much more likely to exit the cavity than to scatter from the mechanical resonator. For more details, see the Supplementary Information. The power in the first-order sidebands ($\pm\omega_m$) scales linearly with the amplitude of mechanical displacement x_{amp}, while the second order sidebands ($\pm 2\omega_m$) scale quadratically and the third order sidebands ($\pm 3\omega_m$) scale cubically. The span of the sweep is doubled and tripled for the second and third mode. When we combine these known behaviors and flip the frequency of the $-1, -2, -3 \times \omega_m$ sidebands, we can overlay all sidebands in the high-amplitude regime (Fig. **4b**).

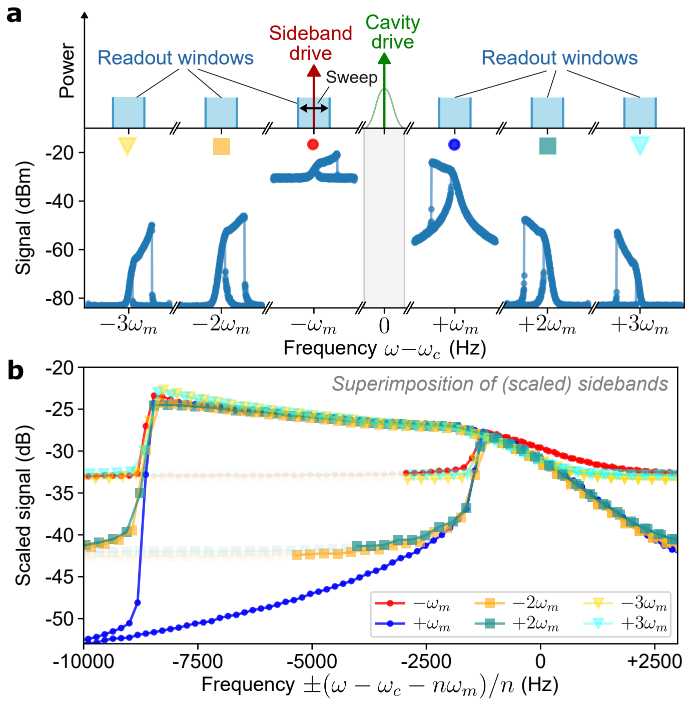

Fig. 4 | Response observed at higher-order sidebands. a: The full optomechanical measurement consists of six sidebands that are read out sequentially. The first red sideband ($-\omega_m$) is at the same frequency as our swept sideband drive, so its signal is superposed on a pedestal from the directly reflected sideband drive signal. **b**: Superimposition of sidebands. All sidebands encode the mechanical displacement with a known proportionality (see main text). The frequency axis of each sideband has been shifted to align the sideband frequencies $\omega_c + n\omega_m$, and the frequency axis of the red sidebands (below the cavity frequency) has been flipped. Furthermore the frequency range has been divided by two for second sidebands and three for third sidebands. The vertical axis of 2nd and 3rd order sidebands has been squared and cubed respectively, as expected from theory.

DISCUSSION

There are many other effects that could result in an apparent nonlinearity, such as the electrostatic force between the drum plates, potential patches in the aluminium, the geometric nonlinearity, the nonlinear optomechanical coupling, and superconducting vortices. We can rule out these effects as an alternative explanation for our observations, as described in detail in the Supplementary Information. Put briefly, we estimate the pressure contributed by e.g., potential patches, based on Kelvin probe force measurements of the electrostatic potential. We simulate the effect of patches in our geometry[50], and find that the patch pressure is several orders of magnitude smaller than the Casimir pressure at our plate separation. Based on this, we rule out the effect of potential patches (and similar for the other effects described in the Supplementary Information). We have not found another source on nonlinearity that could mimic the effect of the Casimir force in this device and consider it to be a strong candidate to explain the observations.

Our future experiments will involve a gate electrode patterned around the drum plate to allow electrostatic tuning of the separation[30] and, by extension, the Casimir force or nonlinear potential. A modest 100 Pa electrostatic pressure is achievable, and sufficient to merge the locally stable solution used in this work with the pull-in point. This should allow for nonlinear mechanics on the single-phonon level, a long-standing goal previously only achieved by coupling to external systems[45,46]. The gate electrode will also allow us to improve the accuracy of the amplitude calibration to improve our bounds on d and P_c, to shed light on the Casimir puzzle[19] of materials with finite conductivity.

In summary, we have observed strongly nonlinear dynamics of a superconducting membrane compatible with the existence of a Casimir potential between superconducting plates. We have shown that this effect does not seem to correspond to other known sources of nonlinearity. Due to the exceptionally small spacing between plates, the Casimir force in this configuration is expected to be much larger than in conventional Casimir experiments, including those at room temperature: for comparison, it is expected to be of the order of magnitude of a tenth of the atmospheric pressure. This suggests that our system is well-suited to accurately probe the remaining uncertainties around the Casimir effect. By adding a gate electrode, we could improve the precision of our nonlinear-dynamics-based measurements beyond the small predicted change at the superconducting transition[28]. More fundamentally, our experimental setup gives a unique access to an extremely strong, tuneable nonlinearity that is intrinsic to the mechanical system. This means that we could obtain well-separated mechanical energy levels without resorting to the nonlinearity of another system, i.e., bring the mechanical resonator into quantum regime without interactions with non-Gaussian photon states or coupling to an external nonlinear system. Furthermore, the competition between the nonlinear potential and the elastic potential can be tuned electrostatically, in situ, to be locally flat, which could be used to probe macroscopic mechanical quantum tunneling[51] or make a mechanical qubit[45,52].

METHODS

Calculation of the Casimir force

To compute the Casimir force between the superconducting plates of our drum, we follow exactly the method of Ref[28]. It is based on the Lifshitz formula[2] for the pressure $P(d,T)$ between two plates as a function of their separation d and temperature T,

$$P(d,T) = \frac{-k_B T}{\pi} \sum_{0}^{\infty} \int_0^{\infty} dk_\perp k_\perp q_\ell \left(\left[\frac{e^{2dq_\ell}}{r_{\mathrm{TE},1}(i\xi_\ell,k_\perp) r_{\mathrm{TE},2}(i\xi_\ell,k_\perp)} - 1 \right]^{-1} + \left[\frac{e^{2dq_\ell}}{r_{\mathrm{TM},1}(i\xi_\ell,k_\perp) r_{\mathrm{TM},2}(i\xi_\ell,k_\perp)} - 1 \right]^{-1} \right), \tag{5}$$

where $k_\perp$ is the in-plane momentum, the $\ell = 0$ term in the sum has a weight of one half, $\xi_\ell = 2\pi \ell k_B T/\hbar$ are the imaginary Matsubara frequencies, $q_\ell = \sqrt{\xi_\ell^2/c^2 + k_\perp^2}$, and TE and TM indicate the two independent polarizations of the electromagnetic field. The Fresnel reflection coefficients for the polarizations (TE,TM) and plates (1,2) are[28]

$$\begin{aligned} r_{\mathrm{TE}}(i\xi_\ell,k_\perp) &= \frac{q_\ell - s_\ell}{q_\ell + s_\ell}, \\ r_{\mathrm{TM}}(i\xi_\ell,k_\perp) &= \frac{\epsilon_\ell q_\ell - s_\ell}{\epsilon_\ell q_\ell + s_\ell}, \end{aligned} \tag{6}$$

where $s_\ell = \sqrt{\epsilon_\ell \xi_\ell^2/c^2 + k_\perp^2}$ and electric permittivity $\epsilon_\ell = \epsilon(i\xi_\ell)$ for the materials of each of the plates 1 and 2. For normal-state materials, we use the Drude model dielectric function $\epsilon_{\mathrm{Drude}}$. For superconductors, the Mattis-Bardeen fomula gives a corrected function ϵ_{BCS}. The analytic continuation of both functions has been derived as[25,28]

$$\begin{aligned} \epsilon_{\mathrm{Drude}}(i\xi) &= \epsilon_0 + \frac{\Omega_p^2}{\xi(\xi + \gamma_{\mathrm{p}})}, \\ \epsilon_{\mathrm{BCS}}(i\xi) &= \epsilon_0 + \frac{\Omega_p^2}{\xi} \left(\frac{1}{\xi + \gamma_{\mathrm{p}}} + \frac{g(\xi,T)}{\xi} \right). \end{aligned} \tag{7}$$

Here, Ω_{p} represents the plasma frequency for intraband transitions, γ_{p} is the relaxation frequency. The contribution from BCS theory is in the form of the factor $g(\xi,T)$, given as[28]

$$g(\xi,T) = \int_{-\infty}^{\infty} \frac{d\epsilon}{E} \tanh\left(\frac{E}{2k_B T}\right) \mathrm{Re}\left[G_+(i\xi,\epsilon)\right]. \tag{8}$$

This expression is valid for temperatures below the superconducting transition temperature, $T < T_c$. The function G_+ is

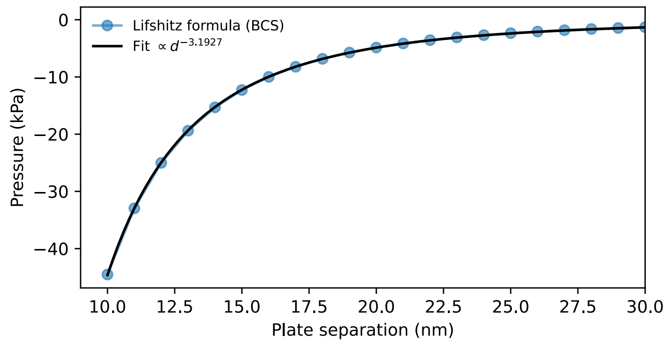

Fig. 5 | The Casimir pressure. The Casimir pressure for various distances as calculated via the Lifshitz formula and the BCS model, and a fit proportional to $d^{-3.193}$.

defined as

$$\begin{aligned} G_+(z,\epsilon) &= \frac{\epsilon^2 Q_+(z,E) + [Q_+(z,E) + i\hbar\gamma]\, A_+(z,E)}{Q_+(z,E)\,(\epsilon^2 - [Q_+(z,E) + i\hbar\gamma])}, \\ E &= \sqrt{\epsilon^2 + \Delta^2}, \\ Q_+(z,E) &= \sqrt{(E+\hbar z)^2 - \Delta^2}, \\ A_+(z,E) &= E(E+\hbar z) + \Delta^2, \end{aligned} \tag{9}$$

and the superconducting gap $\Delta(T)$ is temperature dependent,

$$\Delta = c_1 k_B T_c \sqrt{1 - \frac{T}{T_c}} \left(c_2 + c_3 \frac{T}{T_c} \right), \tag{10}$$

where we take $c_1 = 1.764$, $c_2 = 0.9963$, and $c_3 = 0.7735$ from BCS theory[53].

To evaluate the expression of Eq. (5), we need the material parameters for aluminium, which are tabulated[54]. We use $\Omega_p = 13\ \mathrm{eV}/\hbar$, $\gamma_p = \gamma_0/\mathrm{RRR}$ where $\mathrm{RRR} = 2$ denotes the residual resistance ratio of our thin-film aluminium, and $\gamma_0 = 0.1\ \mathrm{eV}/\hbar$ is a phenomenological relaxation rate (dissipation of current). Finally, setting $\epsilon_0 = 1.03$ as the relative permittivity of aluminium takes into account the core interband transitions[54].

To numerically compute the Casimir pressure in a reasonable amount of time, we take the Matsubara frequencies up to $\ell = 200{,}000$. We determine that this is sufficient by increasing the range of the sum until the final pressure changes by less than 10^{-5} of the value for the previous range. Conversely, to compute the difference between $\epsilon_{\mathrm{Drude}}$ and ϵ_{BCS} it is sufficient to take[28] $\ell \lesssim 600$. Nonetheless, we must also integrate over $k_\perp$. The integrand of Eq. (5) is sharply peaked[25], and heuristic bounds of $\pm 300\sqrt{\xi_\ell \Delta}$ seem to have sufficiently small error.

In Fig. 5, we plot the results of our evaluation of Eq. (5) for our system. While the Casimir pressure scales as $P \propto d^{-4}$ for ideal conductors[1], for real conductors the scaling exponent is different. Using the material parameters for aluminium, the pressure is best described by a fit $P_c = -\frac{1275 \pm 7 \cdot 10^{-24}}{d^{3.193}}$ Pa, with the 95% confidence intervals extracted from the fit to the calculation results. We have plotted the dependence $P \propto d^{-3.193}$ as a black line in Fig. 5.

Drum design and fabrication

The drum fabrication process starts with a 2-inch quartz wafer. For each patterning step, we spin-coat three resist layers (MMA(8.5)MAA EL7 at 4000 RPM (rotations per minute) for 60 s with a 90 s bake at 150 °C, PMMA 950 A3 at 4000 RPM for 60 s with a 90 s bake at 180 °C, and then Espacer 300Z at 4000 RPM for 60 s with a 60 s bake at 90 °C) and pattern the design by electron beam lithography. Our development recipe is a 30 s bath in a 1:3 mixture of MIBK:IPA, followed by a brief bath and rinse in pure IPA. The first pattern step consists of markers for alignment, so we evaporate 5 nm Ti and 40 nm Au. Then we perform lift-off using a hot acetone bath ($\simeq 55$ °C for 20 minutes followed by 2 minutes in a sonicator bath).

The bottom layer pattern consists of the microwave cavity, bonding pads, waveguides and the bottom plate of the drum resonator. We evaporate a 40 nm Al layer in an electron beam evaporator, and realise the liftoff as described before. Then, we grow a 80 nm layer of amorphous silicon (α-Si) by PECVD, which forms the sacrificial layer between the drum plates. This layer is patterned with a single layer of PMMA 950 A9, and etched by reactive ion etching using a mixture of SF_6/O_2.

The top layer consists only of the top drum plate. We evaporate a 120 nm Al layer after patterning. Until now, all steps have been performed on a full 2-inch wafer, but after the final Al evaporation we dice the chips to their final $4 \times 4\ \mathrm{mm}^2$ size. We perform a heat treatment (15 minutes on a hot plate set to between 240 and 280 °C) to redistribute the stress in the top-layer Al and ensure the drums are flat (i.e., not bulging upwards). The final step is the release etch, where we etch the α-Si sacrificial layer away with a reactive ion etch mixture of SF_6/O_2 and get a drum resonator with a suspended top layer.

Measurement setup

Our setup consists of a sample mounted on the base plate of a Bluefors dilution refrigerator, as schematically shown in Fig. 6. To drive our sample, we source the drive a_{mw} at the cavity frequency from a microwave generator, and the drive at the red sideband, a_{sb}, from a vector network analyzer. The drive a_{sb} is attenuated by a directional coupler that merges it to the main drive a_{mw}. Both drives make their way through a suitably attenuated input line to the sample at the base plate of the refrigerator.

The sample is measured in reflection, and the reflected signal is routed through a stack of two circulators and a band-pass filter. A copy of a_{mw} split off from the same source is used to interferometrically cancel the drive component reflected from the sample. This is done to avoid saturating the cryogenic amplifier. The cancellation line has a tunable phase delay and attenuation, which we manually set to maximally cancel the output before starting any measurement. On the output line from the sample, after the directional coupler, there is a low-temperature low-noise amplifier, followed by another amplifier at room temperature. Finally, half of the signal is sent back

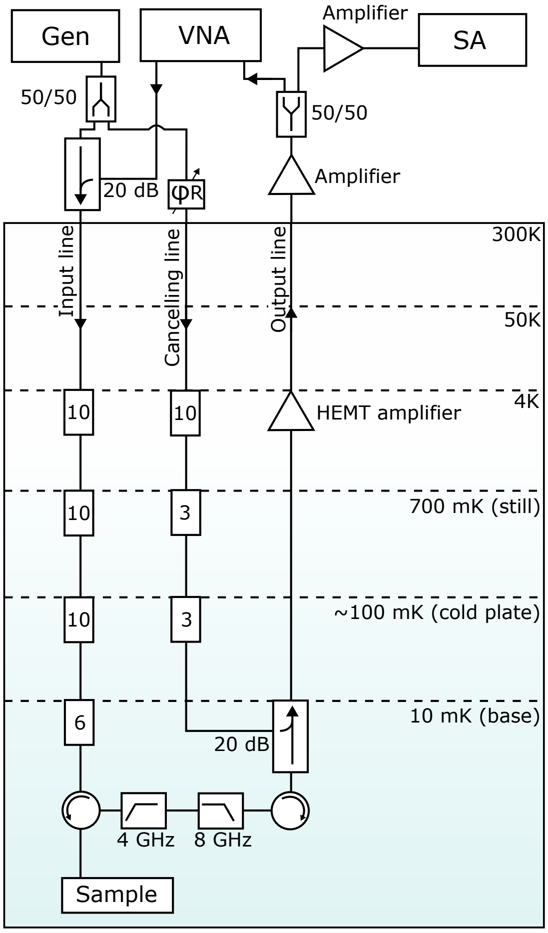

Fig. 6 | Setup. Schematic of the setup used in the experiments. The two drives a_{mw} and a_{sb} are sourced from a microwave generator (Gen) and a vector network analyzer (VNA) respectively. The output signal is split between the vector network analyzer and a spectrum analyzer (SA). The attenuator values are given in dB.

to the network analyzer for measurement, while the other half is routed through a third amplifier to the spectrum analyzer.

Our measurement protocol starts by defining a set of frequencies around the sideband that we will drive. This gives us control over the direction of the frequency sweep. The cavity drive is turned on, then the sideband drive is initialized to the first frequency. We record the signal on the spectrum analyzer while the sideband frequency is swept. We repeat this sequentially for each of the six readout windows, then reverse the frequency sweep direction, and repeat it again for all six readout windows. This stepped protocol means that the sideband drive is briefly turned off to switch to the next frequency, which can cause the oscillator to decay to the low-amplitude branch. The point on the high-amplitude branch at which this happens is not random, it is reproducible between measurements, as evidenced by the overlap of the curves in Fig. **4b**. The stepped drive frequencies do not overlap perfectly with the frequency bins of the spectrum analyzer, and we apply a data filtering scheme detailed in the Supplementary Information.

Drum frequency and effective mass

The released drums are measured in an atomic force microscope (AFM) to estimate the gap at room temperature. The device measured in this work is shown in Fig. **7**. By comparing the heights at various points on the geometry of the drum, we can estimate the layer thicknesses and gap size. The connector to the right in Fig. **7** is deposited in the first evaporation step, so it provides a height reference for the bottom plate of the drum (purple dotted linecut). The top layer shows three distinct heights (along the pink dotted linecut): In the drum center the total thickness is contributed by the thickness of the bottom aluminium plate, the gap and the thickness of the top layer. Closer to the drum edge, the bottom plate stops and only the etched α-Si layer and the top layer thicknesses contribute. At the edge of the drum, the top plate contacts the substrate and accounts for the whole thickness. Finally, beyond the drum we measure only the substrate, although the exposed substrate is etched by ≃120 nm in the drum release step.

We smooth the measurement of the top drum layer and extrapolate it using the known layer thickness to calculate the average gap. The extrapolated gap is shown by dashed black lines in Fig. **7**, and it is approximately 100 nm. "There is a slight concavity in the middle of the drum of 15 nm. This can be explained by a small tensile stress that remains in the aluminium layer due to fabrication. We model the geometry of the drum in COMSOL and show a cut plane through the center of the drum in Fig. **8a**. At room temperature, a 15 MPa tensile stress in the aluminium domain yields a 15 nm concavity that matches the AFM measurement.

When the drum is cooled down, the materials thermally contract, but the contraction of the aluminium is much stronger than that of the quartz. To estimate the relative contractions, we use the temperature dependent material parameters included in COMSOL's basic library, for thin-film aluminium and c-axis quartz (corresponding to our z-cut wafers). We extrapolate the dilation coefficient of quartz below 73 K based on literature values[55]. As a result of the larger relative contraction of the aluminium drum with respect to its substrate, it is subject to an increased tensile stress upon cooling it down to 10 mK. The side walls of the drum unfold and the membrane is brought downwards, which has been previously noted by other groups working with drum resonators[30]. The gap is reduced from 100 nm to 18 nm. Note that this estimate of the drum's separation $d = 18$ nm (unperturbed by the Casimir force) is found from an entirely independent estimation method from the value of the same parameter $d = 18.00 \pm 0.25$ nm found by fitting experimental data. While we consider that this simulation method to estimate d is much less reliable than the fit to experimental data, the fact that these methods independently yield the same value gives confidence in this estimate.

The shape of the fundamental drum mode (Fig. **8b**) is negligibly affected by the thermal contraction, but the frequency of the mode is simulated to vary from 5.4 MHz at room temperature to 16.2 MHz at 10 mK. This frequency is the 'unperturbed' frequency in Table **1** that we use as input for the

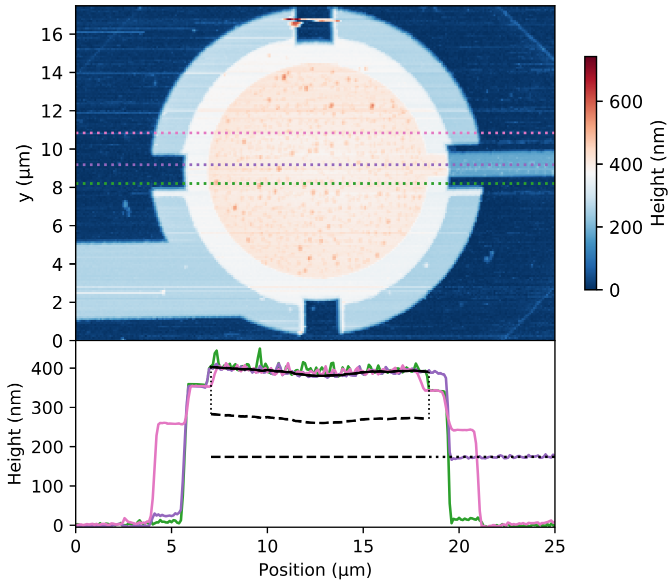

Fig. 7 | AFM measurement of the superconducting drum. The room-temperature gap between the superconducting plates can be estimated from an AFM measurement by comparing the heights along different linecuts (colored dotted lines). The purple line provides a height reference for the bottom plate via the exposed connector on the right side; the green line provides a height reference for the (etched) substrate and the pink line provides a height reference to the thickness of the top layer. We extrapolate the gap (dashed black lines) by subtracting the top layer thickness, 120 nm from the smoothed top linecut. There is a slight concavity of the suspended part, approximately 15 nm on an average gap of 100 nm.

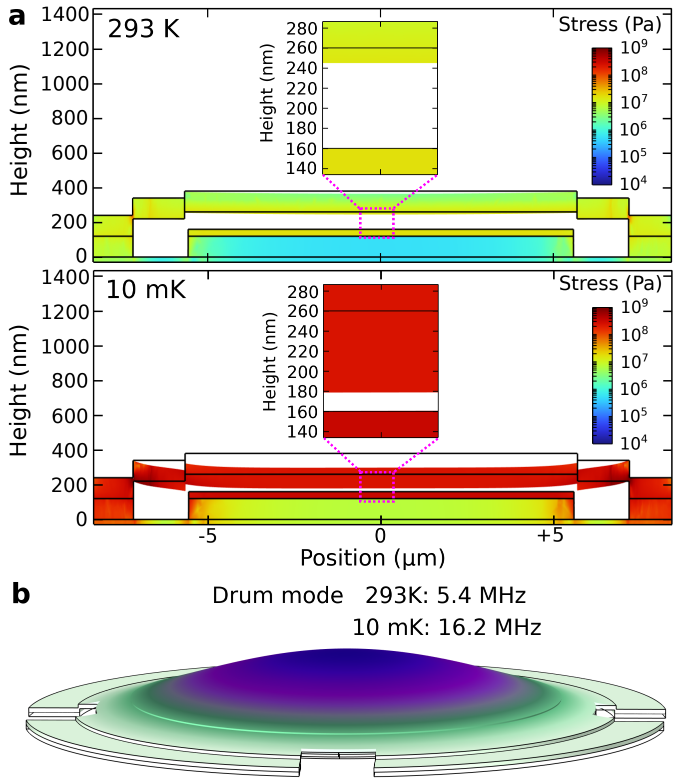

Fig. 8 | Simulated drum mechanics. **a**: A plane cut through the center of the simulated drum geometry shows a 15 nm concavity if a 15 MPa tensile pre-stress is included in the aluminium domain. By cooling down to 10 mK, the aluminium contracts more than the quartz substrate, which greatly increases the tensile stress in the drum. Under this tensile stress, the torque applied on the edges of the drum brings it downwards which reduces the vacuum gap from 100 nm to very low values consistent with the experimentally determined 18 nm according to simulations. **b**: Simulated mode shape and frequencies of the drum. The fundamental drum mode greatly increases in frequency due to the added tensile stress.

Casimir oscillator simulations.

The mechanical mode shape $\mathbf{u}(\mathbf{r})$ computed using COMSOL is shown in Fig. 8b. Here, the displacement detection and actuation profiles coincide and are commonly denoted $\mathbf{w}(\mathbf{r})$. In this case the effective mass is computed as[56]

$$m_{\text{eff}} = m \frac{\int_V \|\mathbf{u}(\mathbf{r})\|^2 \, d^3\mathbf{r}/V}{\left(\int_V \mathbf{w}(\mathbf{r}) \cdot \mathbf{u}(\mathbf{r}) \, d^3\mathbf{r}/V\right)^2}, \tag{11}$$

where m is the physical mass, V is the volume of the oscillator. The amplitude given to $\mathbf{u}(\mathbf{r})$ for the computation is irrelevant. In a good approximation, the actuation/detection profile $\mathbf{w}(\mathbf{r})$ is assumed to be oriented along z-axis, and to be homogeneous across the bottom plate. The physical mass is $m = 5.4 \cdot 10^{-14}$ kg and the effective mass $m_{\text{eff}} = 3.96 \cdot 10^{-14}$ kg.

Simulations of the dynamics in a Casimir potential

In Eq. (1) we have added a strongly nonlinear term to the equation of motion of a harmonic oscillator. It is typical to perform a Taylor expansion of this term for small motions and truncate the resulting series[9,32], but that approximation fails to describe the higher-amplitude motion seen in our measurements. Instead, we use a the MATLAB-based continuation library MatCont[57,58] for our numerical computations, which can handle Eq. (1) without approximations. This toolbox employs different methods for an extensive study of nonlinear dynamics of a system, such as tracking equilibrium points, detecting bifurcations, and continuing branches of periodic solutions. The continuation method involves two steps: iterative prediction of a point on the solution curve and correction of the predicted point through a Newton-like procedure. This procedure is based on linearizing the function at the current guess and finding where the linear approximation intersects with the x-axis, which becomes the next approximation.

For MatCont, the system of equations must be of the first-order and autonomous (no explicit time dependence). The drive term of Eq. (1), $F_0 = F_\text{d} \sin(\omega_\text{d} t)$, is the only term explicitly dependent on time. We can make it autonomous by using the Hopf normal form which allows us to express the dynamics in terms of two real variables in amplitude-phase form. Hopf normal form in Cartesian coordinates reads

$$\dot{u} = (\mu - x^2 - y^2)x - \omega_\mathrm{d} y$$
$$\dot{v} = (\mu - x^2 - y^2)y + \omega_\mathrm{d} x \tag{12}$$

Assuming $\mu = 1$, we choose u to substitute the drive term.

We non-dimensionalize and scale Eq. (1), and split it into two first-order equations. We define,

$$x' = \frac{x}{x_0}, \quad t' = \frac{t}{t_0}, \quad \text{and} \quad y = \dot{x} \tag{13}$$

where $x_0 = 10^{-9}$ m and $t_0 = 2\pi/\omega_\mathrm{r}$.

Substituting all, our system of equations become:

$$\begin{aligned} \dot{x} &= y, \\ \dot{y} &= -Ay - Bx - C(x+d)^n + Du, \\ \dot{u} &= u(1 - u^2 - v^2) - \Omega u, \\ \dot{v} &= v(1 - u^2 - v^2) + \Omega v, \end{aligned} \tag{14}$$

with $A = t_0\gamma_\mathrm{r}$, $B = t_0^2\omega_\mathrm{r}^2$, and

$$C = \frac{t_0^2 P_\mathrm{c} \pi r^2 d^n}{m_\mathrm{eff}(x_0)^{n+1}}, \quad \text{and} \quad D = \frac{t_0^2 F_\mathrm{d}}{m_\mathrm{eff} x_0}. \tag{15}$$

We apply a periodic forcing to the system by arbitrarily choosing $u = 1$, $v = 0$. First, we perform an extended simulation until the system converges to a limit cycle. The last orbit provides the initial conditions for the continuation simulation. By varying certain parameters such as the drive force amplitude F_d, damping coefficient γ_r, separation distance d and the Casimir exponent n, we study how the system's response is affected.

We have become aware of a recent work studying the Casimir force across a superconducting transition[59].

Data and code availability
All data, simulations, measurement and analysis scripts in this work are available at https://doi.org/10.5281/zenodo.14700381.

Acknowledgments
We would like to acknowledge Gongchang Lin for help with the AFM and Eddy Collin for help with the geometric nonlinearity. We acknowledge the facilities and technical support of Otaniemi research infrastructure for Micro and Nanotechnologies (OtaNano), and the Aalto Scientific Computing team for their support. We also acknowledge the financial support of the Finnish Ministry of Education and Culture through the Quantum Doctoral Education Pilot Program (QDOC VN/3137/2024-OKM-4) and the Research Council of Finland through the Finnish Quantum Flagship project (project number 358877, Aalto University). L.M.d.L. acknowledges funding from the Strategic Research Council at the Academy of Finland (Grant No. 338565).

Author contributions
M.d.J., E.K., L.B., and L.M.d.L. designed, developed, and performed the experiments. L.B. developed and fabricated the device, L.M.d.L, M.d.J. and E.K. developed the theoretical and numerical analysis. L.M.d.L. conceptualized the project and L.M.d.L. and M.A.S oversaw it. All authors contributed to writing and editing the manuscript

Competing interest declaration
The authors declare no competing interests.

SUPPLEMENTARY INFORMATION

This part of the document contains the supplementary information.

A. Casimir and van der Waals regimes

Here we justify that the system studied in this work is expected to operate in the force regime commonly referred to as Casimir regime rather than the regime called van der Waals regime. The two regimes are defined for example in Ref.[2], which is a seminal work on the topic of the Casimir force by Lifshitz. In the van der Waals regime, the retardation of the response of one object to charge fluctuations in the other object (or electromagnetic fluctuations at the other object, depending on the point of view adopted to describe the force) is negligible. This regime corresponds to small separations. The Casimir regime corresponds to larger separations where the retardation is important. The Lifshitz model for the estimation of dispersion forces predicts both regimes and allows to define a threshold between the two, as illustrated in Fig. S1. In our equation of motion for the mechanics, we use the fitted strength and scaling of the Casimir force that is shown by the dotted line in Fig. S1. The van der Waals regime appears at separations of $1-3$ nm nanometers, much smaller than separations considered here.

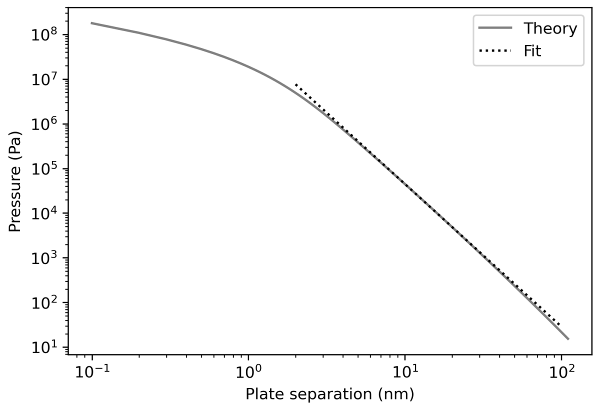

Fig. S1 | Calculation of the pressure across a large range of distances in the Lifshitz formalism. The dotted line shows the Casimir force expression used in the main text, and it is plotted over a large range of separations of the order of magnitude expected in the device $2-100$ nm.

In Ref.[60], it was shown that the effective threshold of distance between realistic surfaces (e.g., with non-negligible roughness) that separate the van der Waals and the Casimir regimes is of the order of 10% of the plasma wavelength. For aluminium, this crossover is then expected around 9.5 nm. Although this is closer to the experimental separation estimated from the model of force employed in the paper, it is still inferior, and the van der Waals regime has to be understood as a limit case (for separations much smaller than the threshold). Therefore, in the experimental situation explored in this paper, we refer to the Casimir force.

B. Optomechanical description

1. Equations of motion

At small amplitude of displacement around the equilibrium position shifted by the nonlinear potential, the optomechanical equations of motion are[48]:

$$\begin{aligned}\dot{\tilde{x}}(t) &= \omega_{\mathrm{m}} p,\\ \dot{p}(t) &= -\omega_{\mathrm{m}}\tilde{x} - \gamma_{\mathrm{m}} p - g_0|a|^2,\\ \dot{a}(t) &= -(i\Delta + \kappa/2)a + ig_0\tilde{x}a + \sqrt{\kappa_{\mathrm{e}}}s_{\mathrm{in}}(t)\end{aligned} \tag{S1}$$

The displacement and momentum are respectively denoted $\tilde{x}$ and p, and a denotes the cavity mode field complex amplitude. The mechanical parameters ω_{m}, γ_{m}, the cavity parameters κ, Δ, and the coupling strength g_0 are the same as in the main text and their values are listed in Table I. Note that we use the mechanical parameters ω_{m} and γ_{m} which are the 'dressed' parameters from the Casimir force rather than the 'unperturbed' parameters ω_{r} and γ_{r}. We operate in a frame rotating at the frequency of the microwave drive. Our system is strongly driven, so we can safely neglect the noise terms in the numerical simulations and use a classical formalism. The input field is a combination of the (strong) drive at the cavity frequency, and a weaker sideband drive. It can be expressed in the rotating frame as

$$s_{\mathrm{in}}(t) = \sqrt{P_{\mathrm{mw}}/\hbar\omega_{\mathrm{c}}} + \sqrt{P_{\mathrm{sb}}/\hbar\omega_{\mathrm{c}}}e^{-i\omega_{\mathrm{m}}t}. \tag{S2}$$

This is enough to solve the system of equations of motion for some initial conditions $\tilde{x}(0)$, $p(0)$, and $a(0)$. We model the detected signal using input-output theory

$$a_{\mathrm{out}} = \sqrt{\kappa_{\mathrm{e}}}a - s_{\mathrm{in}}. \tag{S3}$$

The spectrum of the output field is given by the Fourier transform $\mathcal{F}$,

$$S_{\mathrm{out}}(\omega) = \left|\mathcal{F}\left\{(a_{\mathrm{out}} + a^*_{\mathrm{out}})/2\right\}\right|^2. \tag{S4}$$

This spectrum $S_{\mathrm{out}}(\omega)$ is what we record on the spectrum analyzer.

We can independently calibrate the parameters ω_{m}, γ_{m}, κ, Δ, and g_0 as reported in Sec. D. We also accurately know the powers of the cavity and sideband drive tones we send in, but between the output of the generators and the cavity are attenuators and cable losses (see Methods). To calibrate the amplitudes of our drives at the cavity entrance, we first make a crude estimation based on the relative sideband powers (next section), and then refine it using Eq. S4 (section after that).

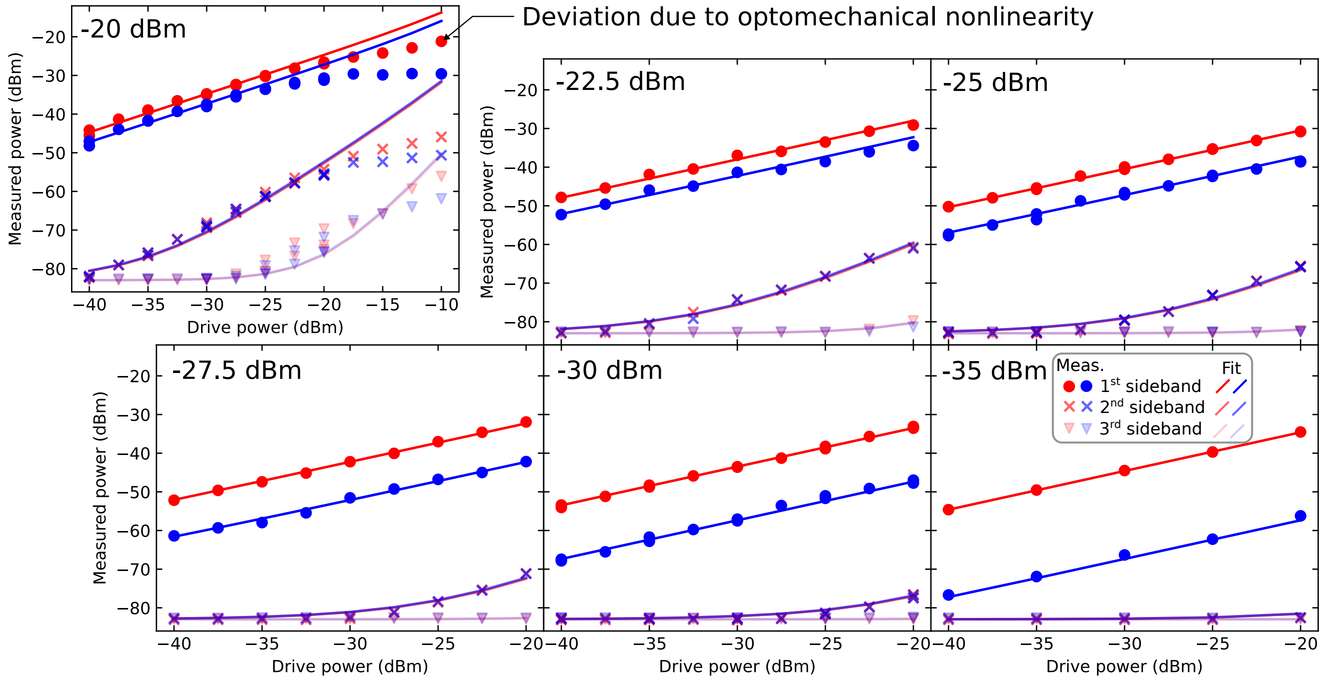

Fig. S2 | Relative sideband powers. Comparison of the maximum powers in all 6 sidebands for different powers of cavity drive a_{mw} (panel labels) and sideband drive a_{sb} (x-axis). The colors indicate whether the sideband is on the red side of the cavity ($a_{-1,-2,-3}$) or on the blue side ($a_{+1,+2,+3}$). The markers are measurements, solid lines are fits to the model of Eq. (S10). Only at the highest powers does our model deviate from the data, which is due to the optomechanical nonlinearity. The asymmetry of the first-order sidebands provides a power reference between the applied drives. The higher order sidebands are symmetric, so they overlap and appear purple in the plot. This symmetry motivates neglecting the scattering processes of a_{sb} which we have done in constructing Eq. (3).

2. *Relative sideband powers*

We have recorded the powers of six sidebands ($\pm\omega_m$, $\pm 2\omega_{\mathrm{m}}$, and $\pm 3\omega_{\mathrm{m}}$) for the measurements reported in the main text. We can compare the relative powers of each of the sidebands, and compare the powers with the sideband drive, to show how our detected signal is proportional to the mechanical displacement. We use the perturbative treatment of the classical coupled mode equations[48,49]. Our starting point is a simplified version of Eqs. (60) and (61) of Ref.[48], where the steady state cavity field amplitude a_0 is defined by the input power of the microwave drive at the cavity frequency, a_{mw}, and cavity parameters κ_e, Δ and κ. We define x_{amp} as a quadrature of the mechanical signal and choose the origin of times such that $\tilde{x} = x_{\mathrm{amp}}(t)\sin(\omega_m t)$.

$$
\begin{aligned}
a_0 &= a_{\mathrm{mw}}\frac{\sqrt{\kappa_e}}{-i\Delta+\kappa/2} \\
a_{+1} &= \frac{g_0 x_{\mathrm{amp}}}{2x_{\mathrm{zpf}}}\frac{a_0}{-i(\Delta+\omega_{\mathrm{m}})+\kappa/2} \\
a_{-1} &= \frac{g_0 x_{\mathrm{amp}}}{2x_{\mathrm{zpf}}}\frac{a_0}{-i(\Delta-\omega_{\mathrm{m}})+\kappa/2}.
\end{aligned}
\tag{S5}
$$

Here, the amplitude of the anti-Stokes- and Stokes-scattered sidebands are denoted with a_{+1} and a_{-1} respectively. These exist in the spectrum at $\pm\omega_{\mathrm{m}}$ away from the frequency of a_0, and they are related to the mechanical amplitude x_{amp}. This expansion is valid regardless of the spectrum of x_{amp}, and simply requires that it is peaked close to 0 frequency and sufficiently narrow so that the sidebands are well-separated.

Our six-sideband treatment is based on repeating the treatment of Eq. (S5), but considering $a_{\pm 1,2,3}$ as the source term instead of a_0. That is, from a_{+1} we recognize two scattering processes, which end up at a_0 and a_{+2} respectively.

$$
\begin{aligned}
a_0 &= +\frac{g_0 x_{\mathrm{amp}}}{2x_{\mathrm{zpf}}}\frac{a_{+1}}{-i\Delta+\kappa/2} \\
a_{+2} &= \frac{g_0 x_{\mathrm{amp}}}{2x_{\mathrm{zpf}}}\frac{a_{+1}}{-i(\Delta+2\omega_{\mathrm{m}})+\kappa/2}
\end{aligned}
\tag{S6}
$$

By repeating this treatment for all orders of sidebands that we measure, we gain a set of linear coupled equations. This resulting system can be written in matrix form as

$$
\begin{bmatrix}
1 & d_{+3} & 0 & 0 & 0 & 0 & 0 \\
d_{+2} & 1 & d_{+2} & 0 & 0 & 0 & 0 \\
0 & d_{+1} & 1 & d_{+1} & 0 & 0 & 0 \\
0 & 0 & d_0 & 1 & d_0 & 0 & 0 \\
0 & 0 & 0 & d_{-1} & 1 & d_{-1} & 0 \\
0 & 0 & 0 & 0 & d_{-2} & 1 & d_{-2} \\
0 & 0 & 0 & 0 & 0 & d_{-3} & 1
\end{bmatrix}
\begin{bmatrix} a_{+3} \\ a_{+2} \\ a_{+1} \\ a_0 \\ a_{-1} \\ a_{-2} \\ a_{-3} \end{bmatrix}
=
\begin{bmatrix} 0 \\ 0 \\ 0 \\ \frac{a_{\mathrm{mw}}\sqrt{\kappa_e}}{-i\Delta+\kappa/2} \\ 0 \\ 0 \\ 0 \end{bmatrix}
\tag{S7}
$$

with

$$
d_{\pm n} = \frac{g_0 x_{\mathrm{amp}}}{2x_{\mathrm{zpf}}}\frac{1}{-i(\Delta\pm n\omega_{\mathrm{m}})+\kappa/2}.
\tag{S8}
$$

We have made the simplifying assumption that repeated interactions ending up at lower-order sideband are negligible in power compared to the (original) lower-order sideband power. This is a valid assumption when $g_0 \ll \kappa/2$, since each individual photon is much more likely to exit the cavity than to scatter from the mechanical resonator.

It is fairly straightforward to numerically solve Eq. (S7) using e.g., Python. This model is valid when the optomechanical interaction is dominated by a single drive tone, which in our case is a_{mw}. However, we have a weaker second drive, a_{sb}, at $-\omega_{\mathrm{m}}$. Since it is much weaker than a_{mw}, we neglect the effect of any scattering interactions from a_{sb} on the sideband amplitudes. The result of this is that there is an asymmetry only between the first-order red (a_{-1}) and blue (a_{+1}) sidebands. If we had included the scattering interactions of the weaker drive, the red and blue sidebands of all orders would have the same asymmetry. However, from the measurements we will see that this is not the case (only the first order sidebands are asymmetric), and therefore we neglect the scattering interactions of a_{sb} in our sideband amplitude calculation. Thus the resulting amplitude(s) due to this drive are

$$\vec{a}_{\mathrm{sb}} = \begin{bmatrix} 0 \\ 0 \\ 0 \\ 0 \\ \frac{a_{\mathrm{sb}}\sqrt{\kappa_{\mathrm{e}}}}{(-i(\Delta-\omega_{\mathrm{m}})+\kappa/2)} \\ 0 \\ 0 \end{bmatrix}. \tag{S9}$$

To fit this model to our data, we solve Eq. (S7) for $\vec{a}$ and compute the output field using the input-output formalism. Here we also add the solution for the weaker drive field a_{sb}. The output field is described by

$$a_{\mathrm{out}} = \sqrt{\kappa_{\mathrm{e}}}(\vec{a} + \vec{a}_{\mathrm{sb}}) - \begin{bmatrix} 0 \\ 0 \\ 0 \\ \frac{a_{\mathrm{mw}}}{-i\Delta+\kappa/2} \\ \frac{a_{\mathrm{sb}}}{-i(\Delta-\omega_{\mathrm{m}})+\kappa/2} \\ 0 \\ 0 \end{bmatrix} \tag{S10}$$

In Fig. S2 we have plotted the maximum observed powers of each of our measured sidebands (markers) for different drive powers, and compared those to our fitted model (solid lines). There is an excellent agreement at all but the highest powers. For the highest powers, the optomechanical nonlinearity reduces the drive efficiency, which reduces the maximum powers seen in the sidebands.

The measurements record the sideband powers, and from our model we extract $|a_{\mathrm{out}}|^2$, but we need two conversion factors to link the theory to our experiments (one for each axis of Fig. S2). There is also attenuation from the room-temperature source to the cavity at 10 mK (see Methods), which gives us an additional conversion factor. The simplifications of the model of Eq. (S7) are not ideal to use it as an accurate calibration tool between mechanical amplitude and measured power, but it serves as a quick estimation of these conversion factors. We use these as an initial guess for the simulation-based calibration method using the optomechanical equations of motion described in the next section.

3. *Absolute amplitude calibration*

Here we describe the calibration of measured signals into displacement. After the calibration of optomechanical parameters described in Sec. D, a remaining unknown is the total attenuation between microwave sources and the cavity entrance. Indeed, input lines include attenuators with known attenuation (see Fig. **6**) but also losses incurred along the cables whose exact value is unknown. To realize this calibration, we compare the measured response of the system at small displacements with numerical predictions.

To model the response, we let Eq. (S1) evolve numerically until it has settled into a steady state, and simulate the steady state for an additional 10 ms. We compute the Fourier transform of the output field, as in Eq. (S4), which gives us the observed power, while we obtain the mechanical oscillation amplitude from the size of the orbit of $\tilde{x}$ of Eq. (S1). To scale the simulated signal in the same way as the measured signal, we multiply the simulation result by the detection scale factor (W/photon) S_{c} found in Sec. D and compensate for the finite simulation time. We then compare the maximum simulated power around the first red and the first blue sideband ($\omega_c \pm \omega_m$) with the maximum measured amplitude. We calibrate the cables attenuation by matching the computed and measured signals simultaneously for these two sidebands' maxima (see S3) as well as for a point on the side of the red sideband detuned by 3 kHz (see Fig. S4). Fig. S3 shows that the calibrated values allow to match data and simulations for all combinations where both powers are in the range [−40 dB, −30 dB]: these powers correspond to those for which the mechanical responses were measured to be approximately Lorentzian and therefore reasonably well described by Eq. (S1). Additionally, S4 shows that the same calibrated values allow to match data and simulations at all powers for the off-resonant point where the displacement is also very small.

From this procedure, we find that the power of the cavity drive P_{mw} at the input of the device is attenuated by 47.4 dB from the power issued by the generator. Out of this attenuation, 36 dB comes from the installed attenuators shown in Fig. **6**, 3 dB comes from a splitter at room temperature, and the rest (about 8 dB) is of the order of magnitude of the total attenuation expected from the cryogenic transmission line itself. Similarly, we find that the sideband tone power P_{sb} at the input of the cavity is attenuated by 69.6 dB from the power issued by the generator. The difference of 22.2 dB between the attenuations of the two tones is mainly due to the 20 dB attenuation of a directional coupler in front of the vector network analyzer generating the sideband drive (see Fig. **6**).

Fig. S3 also shows the maximum amplitude of sidebands computed at larger drives. As shown in the figure, while Eq. (2) cannot reproduce the asymmetric mechanical lineshapes measured at larger drives, its solution still predicts the *maximum amplitude* of measured sidebands rather accurately

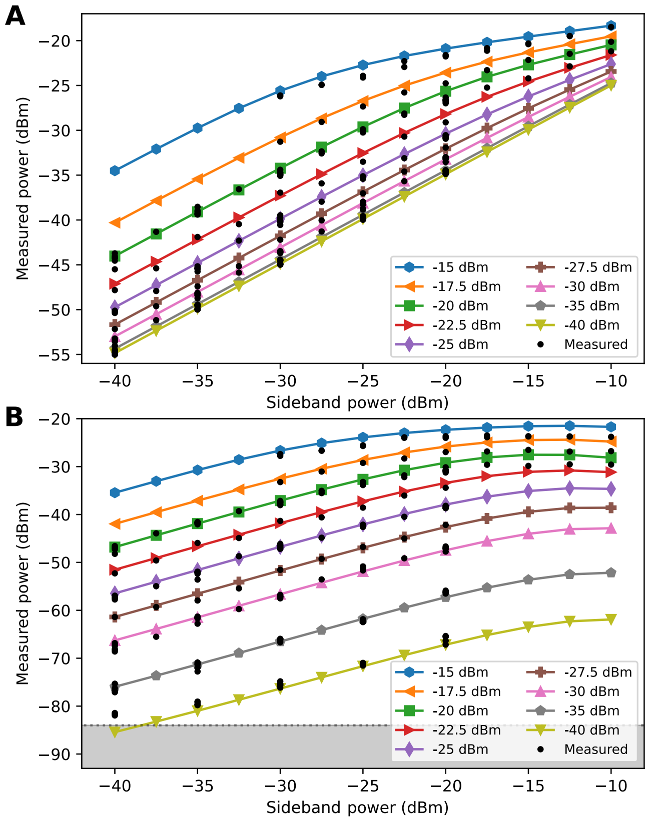

Fig. S3 | Sideband calibration. **A** Simulated powers (colored lines with various markers) and observed peak powers (black dots) for the red sideband. The legend indicates P_{mw}, the x-axis is P_{sb}. The agreement between the simulations and the measurements at low power serves as a calibration for the numerical simulations. **B** Idem, but for the blue sideband. The grey shaded area shows the noise floor for the measurements.

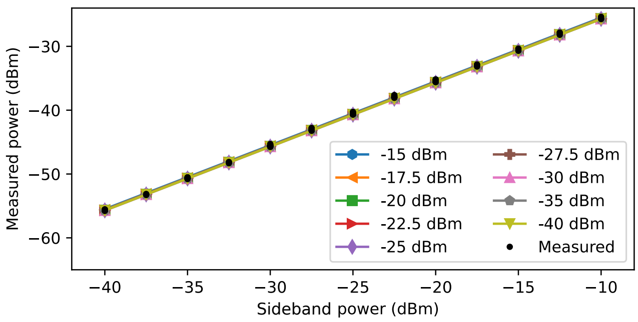

Fig. S4 | Input power calibration. The 3 kHz off-resonant drive simulations show a perfect overlap between all simulated (colored markers) and measured powers (black dots).

up to very large driving forces.

The displacement amplitude simulated for all combinations of cavity and sideband drive powers are shown in Fig. S5. At small amplitudes, the maximum amplitude scales linearly with both cavity and sideband drive powers, but at some point this relation breaks down. This is not due to the nonlinearity of the oscillator since Eq. (2) does not simulate it. Instead, this is due to the loss of drive efficiency due to optomechanical effects.

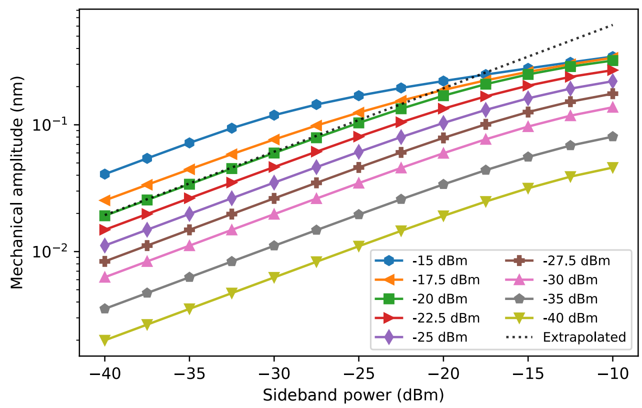

Fig. S5 | Mechanical amplitudes simulated with 2 for different combinations of cavity and sideband drive powers.

4. *Calculation of the drive efficiency*

The tenet of (dispersive) cavity optomechanics is that the cavity frequency ω_c shifts as a result of the displacement $\tilde{x}$[48]. In this work, the amplitude of $\tilde{x}$ is significant, and the cavity frequency shift $\frac{\partial \omega_c}{\partial \tilde{x}}$ causes a mismatch between the cavity frequency and the drive frequencies, $\omega_{\mathrm{mw}} \simeq \omega_c$ and $\omega_{\mathrm{sb}} \simeq \omega_c - \omega_m$. The cavity frequency $\omega_c(t)$ is thus a function of time, it oscillates at ω_m depending on the exact trajectory of the drum.

To put it simply, for larger oscillations of $\tilde{x}$, the frequency mismatch between cavity and drive is greater and the power in the cavity decreases. The oscillation is fast with respect to the cavity linewidth, as we are in the resolved sideband limit $\kappa \ll \omega_m$, which means that the cavity amplitude changes slowly with respect to the oscillation of ω_m. Furthermore, we also have two drives separated in frequency. So while the power resulting from the drive at ω_c is maximal for small amplitudes of $\tilde{x}$, the power resulting from the drive at $\omega_c - \omega_m$ peaks for some specific oscillation amplitude of $\tilde{x}$.

We calculate the drive efficiency by solving Eq. (S1) with a fixed mechanical amplitude x. We let the system simulate only for a brief time, such that the cavity amplitude a has had time to stabilize. From the last 20 mechanical periods, we extract the power in the cavity. This brief simulation is repeated for 101 values of x logarithmically spaced between 1 pm and 1 nm for all different cavity drive powers used in the experiments.

In the regime that is relevant for our experiment, the drive efficiency is 1 for small mechanical amplitudes (< 100 pm), and decreases quickly towards zero beyond that. However, at even larger mechanical amplitudes, beyond what we achieve in this work, the drive efficiency recovers to a non-negligible number in a series of bands that represent stable orbits as described in Ref.[61].

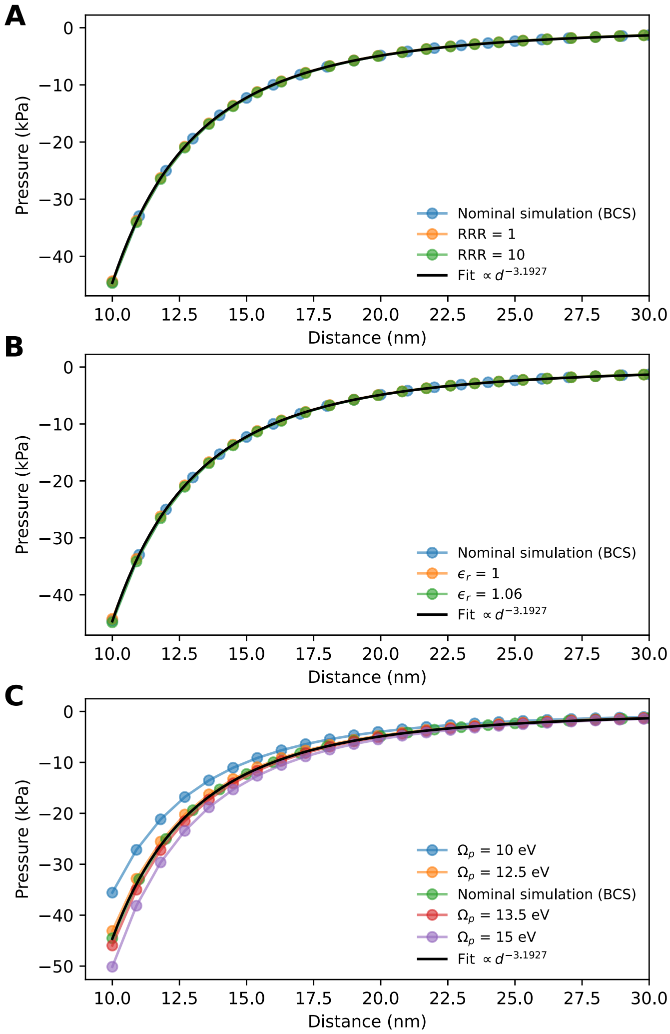

Fig. S6 | Effect of material parameters. A: The residual resistance ratio (RRR) rescales the dissipation rate $\gamma_p = \gamma_0/\mathrm{RRR}$, but varying it from the nominal value RRR = 2 does not significantly affect the Casimir pressure. **B:** Varying the relative permittivity of aluminium from the the nominal value $\epsilon_r = 1.03$ does not significantly affect the Casimir pressure. **C:** Varying the plasma frequency from the nominal value $\Omega_p = 13$ eV affect the Casimir pressure amplitude P more strongly than the Casimir scaling n.

To fit a measured response driven by a given combination of powers, we first estimate the driving force F_0 (unaffected by the loss of drive efficiency) corresponding to that combination using the calibration detailed in the previous section. We simulate the corresponding response using MatCont as described in Methods, then correct it point-by-point to account for the loss of drive efficiency. This procedure is repeated for different values of parameter d appearing in the Casimir force model in order to realize the fit using a standard least-square routine.

C. Simulating the Casimir nonlinearity

1. *Role of Casimir parameters*

We perform the fit of distance d without considering variations in the calculated Casimir pressure, i.e., we consider the Casimir pressure amplitude P and scaling n to be fixed. To motivate this choice, we show that the Casimir pressure does not vary much with the material parameters γ_0 (or RRR), ϵ_0, and Ω_p. We repeat the Casimir pressure calculations for different material parameters, as shown in Fig. S6, and we fit curves of the form $P_c = P/d^n$ to distinguish changes in the amplitude of the Casimir pressure (P) from changes in the Casimir scaling (n).

The residual resistivity ratio RRR can vary depending on the material source and deposition method. We have previously measured similar films to have RRR = 2 using a four-point probe method. Variations in the RRR affect the phenomenological dissipation rate, $\gamma_p = \gamma_0/\mathrm{RRR}$, so Fig. S6**A** shows the effect of varying either RRR or γ_0. From the overlap between the curves, we conclude that RRR and γ_0 affect neither the Casimir pressure amplitude P nor exponent n.

The relative permittivity of aluminium, $\epsilon_r = 1.03$ was experimentally determined and follows from the core-interband transitions of the aluminium atoms[54]. We show in Fig. S6 that variations in this parameter do not lead to significant changes in the Casimir pressure.

We take the plasma frequency of aluminium $\Omega_p = 13$ eV from Ref.[54]. In Fig. S6 we show that varying Ω_p changes the Casimir pressure, but its effect on the Casimir scaling is marginal. A 25% variation in Ω_p corresponds to a 25% variation in P, but less than 1% variation in n.

To further motivate our choice to consider the calculated Casimir parameters as fixed values, we fit our experimental data to the Casimir force calculated with $\Omega_p = 10$ and 15 eV. The results are shown in Fig. S7, where we have taken the optomechanical calibration of mechanical amplitude to be fixed. Taking $\Omega_p = 10$ eV (Fig. S7**A**), the Casimir force is weaker, which means that to experience the same nonlinearity at fixed mechanical amplitude, the plate separation d must be reduced. Vice versa, taking $\Omega_p = 15$ eV (Fig. S7**B**) leads to a better fit at larger d. The variations in Ω_p are significant (25% of the total value), and well beyond the uncertainty of which the plasma frequency is established in aluminium, yet the effect on the fitted parameter d is limited (~1 nm). Thus, we conclude that our choice to take the Casimir pressure amplitude and scaling to be fixed values leads to a smaller error than the optomechanical amplitude calibration does.

2. *Static shift of frequency and position*

As we illustrated in Fig. **1A**, we start with a harmonic oscillator centered at distance d from the other plate with unperturbed resonance frequency ω_r. The Casimir force pulls the top plate closer to the bottom plate, such that it oscillates around some value $d' < d$, and softens the spring so the mechanical frequency is decreased, $\omega_m < \omega_r$. We do not

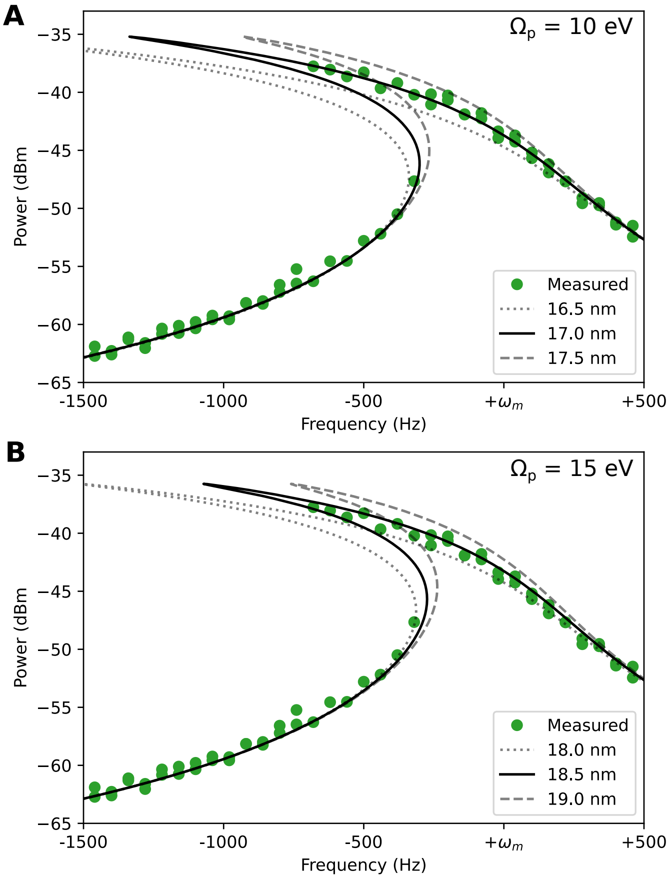

Fig. S7 | Fits for Casimir force variations. A: The Casimir force for a material with plasma frequency ω_p = 10 eV is weaker than the nominal Casimir force used in this work. The Casimir nonlinearity fits to a plate separation of d = 17.00 ± 0.25 nm. **B:** The Casimir force for a material with plasma frequency ω_p = 15 eV fits to a plate separation of d = 18.50 ± 0.25 nm.

know d or ω_r a priori, but we can measure ω_m with great accuracy, leaving us to consider d (or somewhat equivalently the Casimir pressure P_c) as a parameter to be fitted. That means that for every value d, we have to find the value of the unperturbed frequency ω_r such that the perturbed frequency $\omega_m = 2\pi \times 10.001$ MHz. Rather than finding a clever algorithm to compute the correct values of ω_r, we numerically evaluate the problem for a selection of d-values and interpolate. In Fig. S8 we show the frequencies ω_r that result in the correct value of ω_m for different values of d.

The numerical simulations of the Casimir oscillator in MatCont start with the drive frequency far detuned. To start the continuation, we need this step to converge to a solution. However, the total potential sketched in Fig. **1A** has a local minimum (where our resonator is) and a global minimum beyond the pull-in point. We need to feed MatCont the correct initial values such that it converges to the local minimum instead of showing us the pull-in collapse. To find these, we compute the position of the local minimum of the total potential for various values of d, while using the values of ω_r from Fig. S8. The unperturbed frequency ω_r is related to the

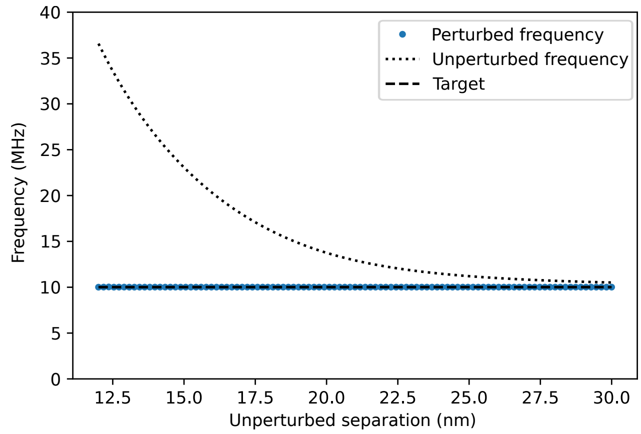

Fig. S8 | Casimir frequency shift. Plot of the unperturbed frequencies ω_r for various values of spacing d that result in the correct value for ω_m when the Casimir force is included.

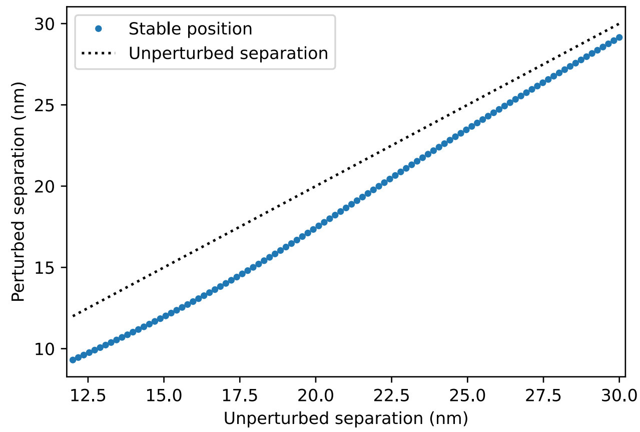

Fig. S9 | Shift of the local potential minimum due to the Casimir force. Distance between the local minimum (stable position) and the bottom plate for various values of the unperturbed separation d. The dotted line indicates where the initial separation would be the stable position. For d = 18.0 nm, the difference between the unperturbed separation and the local minimum is 2.9 nm.

mechanical stiffness needed to compute the potential, not ω_m. We plot the stable position of the local minimum for different values of d in Fig. S9. As with the unperturbed frequencies, we interpolate linearly between the calculated values for the numerical simulations and fits of the main text.

3. *Role of mechanical parameters*

We study the effect of variations of the parameters of the Casimir effect through numerical simulations. We vary the drive force amplitude F_d, damping coefficient γ_r, separation distance d, and the Casimir exponent n. The results are shown in Figure S10.

We show how the system response transforms from linear behavior at small amplitude to nonlinear behavior at large

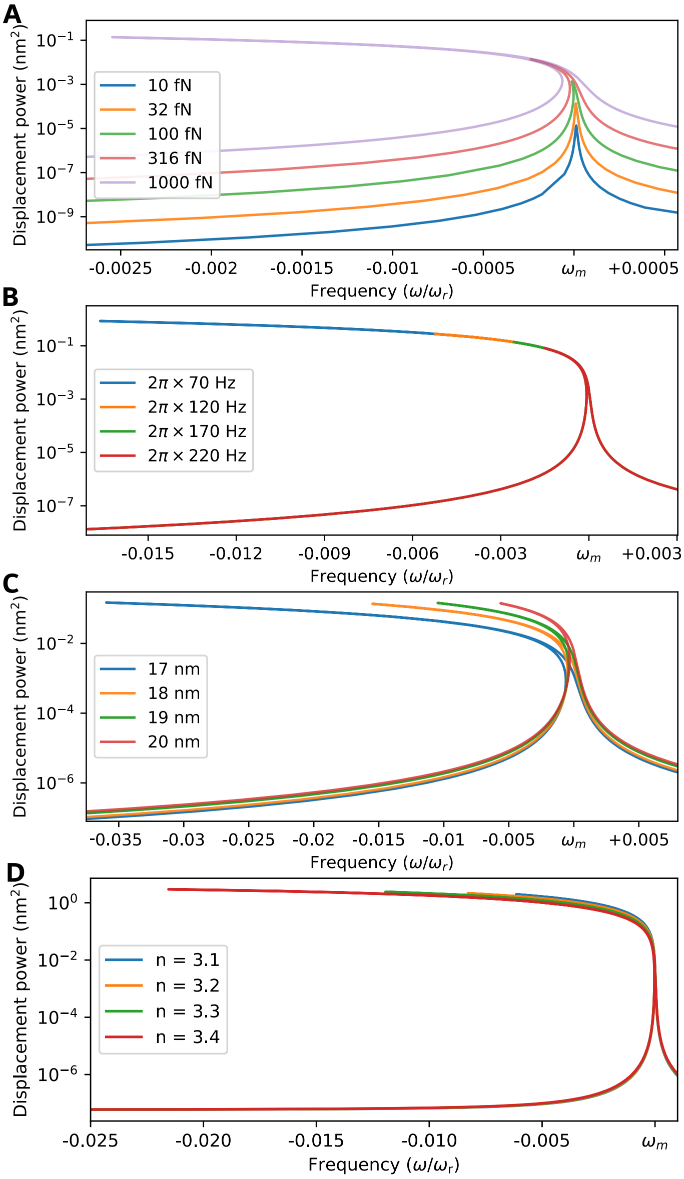

Fig. S10 | Effect of the Casimir force parameters. **A**: Effect of different drive force amplitudes F_d. **B**: Effect of varying the damping coefficient γ_r. **C**: Effect of varying the distance between the plates at mechanical zero. d. The frequencies of the curves have been shifted to align on ω_m. **D**: Effect of varying the Casimir scaling n, where the amplitude of the Casimir pressure has been fixed at the equilibrium position d'.

amplitude in Fig. S10**A**. When the drive force amplitude is small, F_d = 10 fN, the frequency response of the system is Lorentzian, as expected. For larger amplitudes, the resonance peak broadens and becomes asymmetrical, indicative of nonlinear resonance where the response of the system is no longer linearly proportional to the drive force. The resonance frequency decreases with increasing amplitude, which indicates that the Casimir force is a strong softening nonlinearity.

In Fig. S10**B**, we study the effect of the mechanical damping rate γ_r. Lower damping allows for greater energy accumulation within the system at equal drive amplitudes, leading to larger oscillations and a more pronounced nonlinearity. However, all the backbones of the curves for different damping rates align, meaning the damping coefficient does not have a significant effect on the nonlinearity we observe.

The most important parameter for Casimir experiments is the separation distance d, which is the distance between the plates in the absence of the Casimir force. Since the Casimir effect strongly scales with the distance d, the Casimir force between drums spaced d = 17 nm apart (blue curve in Fig. S10**C**) causes a much stronger nonlinear behavior than for drums spaced d = 18 nm apart. The region where there are multiple solutions is much more extended, even if the amplitude of the mechanical oscillations remains the same. All curves were generated using the same drive force, which indicates that the separation distance d does not affect the mechanical amplitude significantly.

Finally, we show the effect of the Casimir force exponent n in Fig. S10**D**. The The Casimir pressure was adjusted for each n such that the value at the equilibrium position (d') was kept constant. While the trend from the change in n somewhat resembles the trend from the change in d, it is noticeable that the peaks curve more sharply with increasing n, while they start curving at lower amplitude for lower d.

D. Characterization of optomechanical system

1. *Calibration of microwave cavity parameters*

Our microwave cavity design was optimized to allow coupling to two separate drum resonators with two cavity modes, as shown in Fig. S11**A**, and described in more detail in the Supplementary of Ref.[39]. In our device, one of the drum resonators inadvertently collapsed and shorted one half of the cavity, though this cannot be seen in the microscope image. Instead, we deduce this by the number of microwave modes we see (one), its frequency ($\omega_\mathrm{c} = 2\pi \times 5.46180$ GHz), and the number of mechanical signals we can observe in a wide-band frequency sweep at high red-sideband drive power (one).

We simulate our cavity using Sonnet, where we have replaced the collapsed drum by a short (Fig. S11**B**. At first, we replace the suspended drum by a numerical capacitance. An initial guess for the capacitance of this drum based on the diameter $2r$ = 11.3 µm and a gap of 15.1 nm is 0.059 pF. To provide an initial estimate of the optomechanical coupling, we vary the spacing of the vacuum layer in our Sonnet model, and re-compute the cavity resonance frequency. We find $\frac{\Delta\omega_\mathrm{c}}{\Delta x} \simeq 2\pi \times 104\ \mathrm{MHz\,nm^{-1}}$. We use the zero point motion $x_\mathrm{zpf} = \sqrt{\frac{\hbar}{2m_\mathrm{eff}\omega_\mathrm{m}}} = 4.6$ fm and estimate the coupling rate $g_0 \simeq x_\mathrm{xpf}\frac{\Delta\omega_\mathrm{c}}{\Delta x} \simeq 2\pi \times 480$ Hz. This is larger than the coupling rate that we find when we calibrate our system by about a factor 3, which we attribute to details not captured by our simulation: microscopic defects or fabrication imperfections, wire bonds, and box resonances. The simulated microwave cavity mode is not qualitatively affected by these limitations, but the we should treat the optomechanical coupling it yields

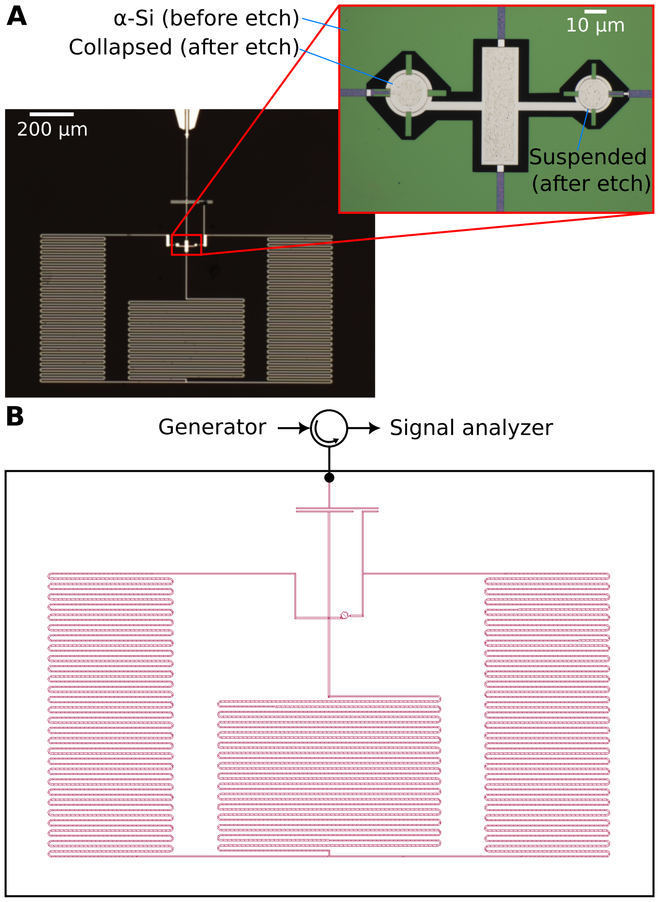

Fig. S11 | Microwave cavity. **A:** Microscope image of our microwave cavity (after the experiment), with the inset showing the drums (during fabrication). The larger (left) drum collapsed before the experiment, while the smaller (right) drum survived. **B:** Sonnet simulation of our cavity, with the collapsed drum replaced by a short.

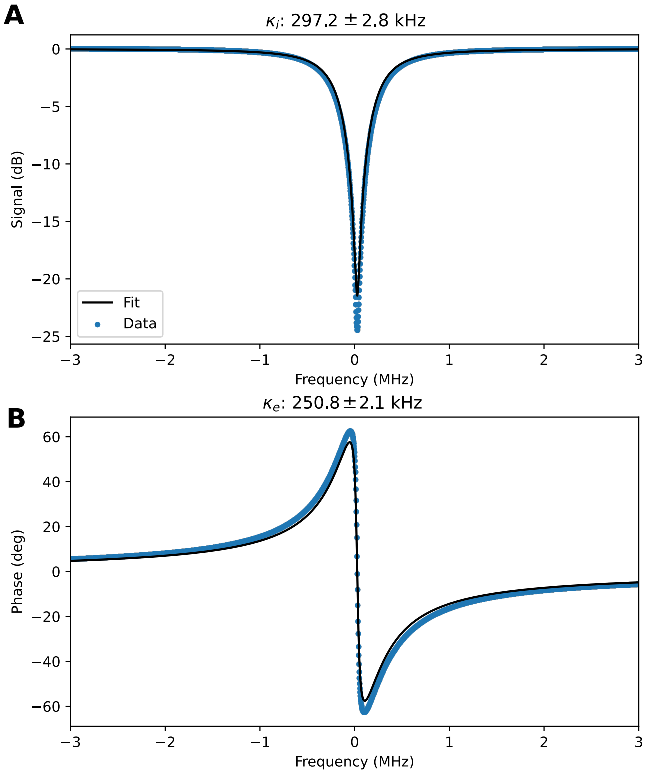

Fig. S12 | Microwave cavity calibration. **A**: Amplitude response of the microwave cavity (blue) and the fitted linewidth (black). **B**: Phase response of the microwave cavity (blue) and the fitted response (black). The internal and external linewidths, $\kappa_i = 297.2 \pm 2.8$ kHz and $\kappa_e = 250.8 \pm 2.1$ kHz respectively, are fitted as described in the text.

as an optimistic estimate.

We characterize our microwave resonator by recording its reflected response (both amplitude and phase) and fitting this with the equation[48]

$$R = \frac{(\kappa_i - \kappa_e)/2 - i(\Delta - \omega_c)}{(\kappa_i + \kappa_e)/2 - i(\Delta - \omega_c)}. \tag{S11}$$

Here, the square of the reflection coefficient, $|R|^2$, describes the probability that a photon reflects off our cavity. Furthermore, the internal and external linewidths, κ_i and κ_e, sum up to the total linewidth $\kappa = \kappa_i + \kappa_e$, and the detuning $\Delta = \omega_d - \omega_c$ describes the difference between the drive frequency ω_d and the cavity center frequency ω_c.

We use a three-step fit process. First, we de-trend the cavity signal by fitting a polynomial of order 2 to the first and last 10% of the amplitude signal, and a polynomial of order 1 to the same parts of the phase signal. This assumes the cavity resonance is approximately at the center of our measurement span, and that the background is reasonably flat within this span. Then we fit an ellipse to the response R on a Smith chart, from which we compute the cavity parameters and use those as initial guesses for the third and final step. By using scipy's `curve_fit` function[62], we fit our data to Eq. (S11). The response, fit and extracted parameters are shown in Fig. S12. We fit the amplitude in logarithmic scale to enhance the accuracy around the cavity center, while the phase is fitted in linear scale.

Our cavity resonance frequency $\omega_c = 2\pi \times 5.46180$ GHz, and the internal and external linewidths are $\kappa_i = 2\pi \times 297.2 \pm 2.8$ kHz and $\kappa_e = 2\pi \times 250.8 \pm 2.1$ kHz respectively.

2. *Thermalization of drum motion*

We calibrate the temperature to which the mode of our mechanical resonator thermalizes by sweeping the temperature of the dilution refrigerator. At each temperature, we measure the mechanical spectrum and fit a Lorentzian to the data. This way, we can extract the frequency ω_m, linewidth γ_m, and the area of the mechanical peak.

The amplitude of the thermal motion peak is shown in Fig. S13. It increases linearly with temperature below 200 mK. At higher temperatures the quasiparticles in the Al superconducting cavity shift and damp the cavity mode which reduce the readout efficiency. The peak amplitude stays pro-

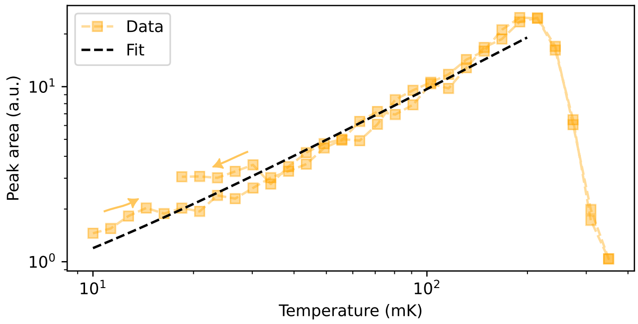

Fig. S13 | Thermalization of the drum mode. Area of the fitted mechanical peaks, indicating the thermal energy of the oscillator mode. The dashed curve is a linear fit offset by only about 3 mK, well below the base temperature of 10 mK, showing the good thermalization of the mode with the cryostat at the base temperature. At higher temperatures, the microwave cavity response disappears, likely due to quasiparticles in the superconductor (Aluminium), which shifts the microwave cavity frequency.

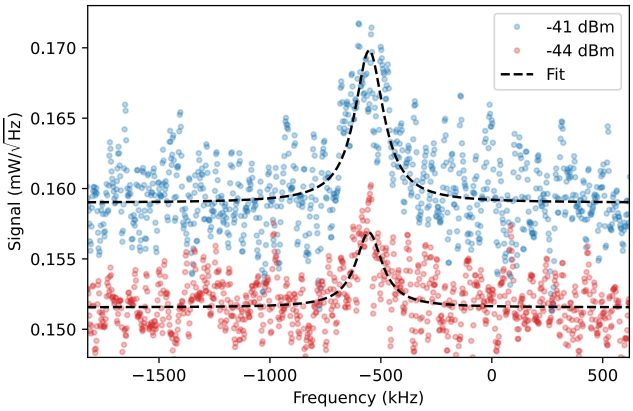

Fig. S14 | Calibration of the optomechanical coupling rate. The amplitude of the scattered peak is compared to a signal of known power (not shown). The area under the peak is calculated from a Lorentzian fit, and the ratio of the fitted peak with the signal of known power yields the optomechanical coupling rate g_0.

portional to the temperature all the way to the base temperature of 10 mK: we conclude that the drum thermalizes down to 10 mK and we use this assumption to extract g_0 in the next section.

3. *Calibration of single-photon coupling*

The optomechanical coupling g_0 is calibrated by sending in a tone at the red sideband, $\omega_c - \omega_m$, and comparing the amplitude of the scattered peak with the amplitude of the drive. The resulting signal is shown in Fig. S14, and we fit a Lorentzian curve to the peak. We extract the area A under the curve, which is proportional to the number of scattered photons, and we compare it to the number of photons in the drive tone, $\hat{a}^\dagger_{sb}\hat{a}_{sb}$. The optomechanical coupling can be extracted from these amplitudes as

$$g_0^2 = \frac{A}{|a_{sb}|^2}\frac{|1-\kappa_e\chi(\omega_c-\omega_m)|^2|\chi(\omega_c-\omega_m)|^2}{|\chi\omega_c|^2 n_m}, \tag{S12}$$

which contains the ratio of the peak amplitude, as well as the cavity susceptibilities at the red sideband and cavity center (assuming zero detuning),

$$\begin{aligned}\chi(\omega_c-\omega_m) &= \frac{1}{\kappa/2 + i\omega_m}\\ \chi(\omega_c) &= \frac{1}{\kappa/2}.\end{aligned} \tag{S13}$$

The thermal mechanical occupation can be calculated as

$$n_m = \frac{k_B T}{\hbar\omega_m}. \tag{S14}$$

With these expressions, we fit $g_0 = 2\pi \times 150 \pm 9$ Hz.

4. *Effective linewidth*

We account for optical damping (sideband cooling) by using an effective linewidth, γ_{eff} that relates to the intrinsic (low-power) mechanical linewidth γ_m via

$$\gamma_{eff} = \gamma_m + \frac{4g_0^2|\alpha|^2}{\kappa}P = \gamma_m + \eta P. \tag{S15}$$

Here, $|\alpha|^2$ is the number of photons in the cavity at the red sideband frequency, η is some coefficient which we are trying to fit and P is the power sent out from our microwave source at the red sideband frequency. The exact value of η depends not only on optomechanical parameters g_0 and κ, but also on the attenuation in the microwave lines between source and sample. However, as long as the latter are constant between measurements, we can use η and do not need to know the exact attenuation from our lines.

To fit the intrinsic linewidth, mechanical frequency and η, we vary the power sent in on the red sideband.

5. *Scale and phonon number calibration*

We do not know a priori the exact scaling between the spectral power that we measure and the expected spectral power of a single photon or phonon. Thus we need to derive an expression for the spectral power in terms of system parameters that can be measured, to use it as a fit function to our measurements.

Here we use operator formalism as the calibration described in this section is performed close to the quantum regime where vacuum fluctuations should be taken into account. We start from the equations of motion for the cavity field $\hat{a}$ and mechanical ladder operator $\hat{b}$ corresponding to $\tilde{x}$: $\tilde{x} = x_{zpf}(\hat{b}+\hat{b}^\dagger)$. In the sideband-resolved limit, with a drive detuned by $-\omega_m$ from the cavity frequency (at the red sideband), with $\hat{a}$ separated into a steady state amplitude and some fluctuations

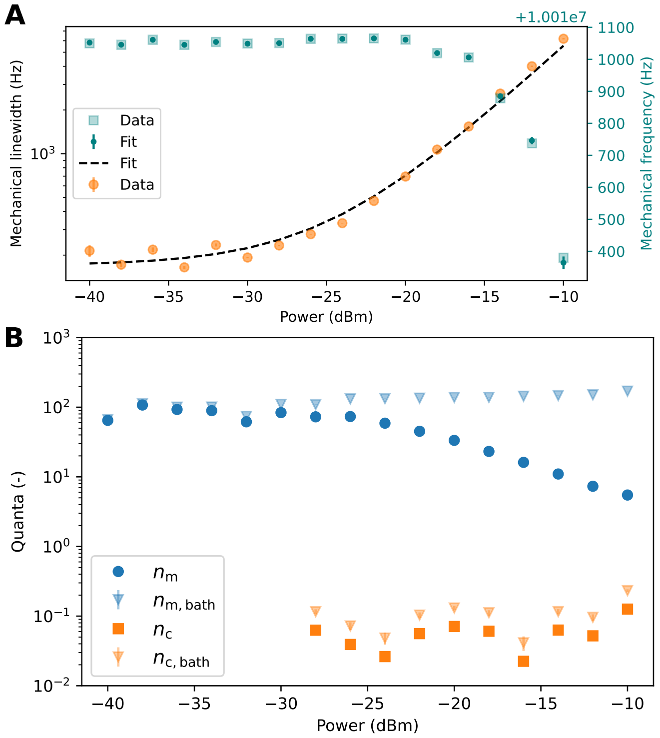

Fig. S15 | Power calibration. **A**: Mechanical linewidths (orange) and frequencies (teal) for various driving powers on the red sideband. **B**: Extracted mechanical occupation n_m and cavity photon number n_c, as well as the equivalent quanta in the respective thermal baths.

$\hat{a} = \alpha + \delta\hat{a}$, the equations of motion can be written in the frequency domain as

$$\hat{a}[\omega] = \chi_c[\omega+\Delta]\left(-ig_0\alpha\left(\hat{b}[\omega]+\hat{b}^\dagger[\omega+2\omega_m]\right)+\sqrt{\kappa_i}\hat{a}_{in}[\omega]\right),$$
$$\hat{b}[\omega] = \chi_m[\omega]\left(-ig_0\left(\alpha^*\hat{a}[\omega]+\alpha\hat{a}^\dagger[\omega+2\omega_m]\right)+\sqrt{\gamma_m}\hat{b}_{in}[\omega]\right). \tag{S16}$$

Here, the cavity susceptibility $\chi_c[\omega] = \frac{1}{\kappa/2-i\omega}$ and the mechanical susceptibility $\chi_m[\omega] = \frac{1}{\gamma_m/2-i\omega}$ are used as shorthands, and the input fields are $\hat{a}_{in}[\omega]$ and $\hat{b}_{in}[\omega]$.

In the good cavity limit, we can neglect the terms at $\omega \pm 2\omega_m$ and Δ. We can replace $\hat{b}[\omega]$ in our expression for $\hat{a}[\omega]$ and compute the spectrum S_{out} of the output field $\hat{a}_{out}[\omega] = \hat{a}_{in}[\omega] - \sqrt{\kappa_e}\hat{a}[\omega]$. We get

$$S_{out} = \frac{1}{2} + \kappa_e\kappa_i\left|\tilde{\chi}_c[\omega]\right|^2 n_{cav} + g_0^2|\alpha|^2\gamma_m\kappa_e\left|\tilde{\chi}_c[\omega]\chi_m[\omega]\right|^2 n_{th}. \tag{S17}$$

The three terms come from the external port of the cavity (vacuum), environmental noise at the cavity frequency (n_{cav}) and mechanical noise (thermal, n_m). The shorthand $\tilde{\chi}_c[\omega] = \frac{\chi_c[\omega]}{1+g_0^2|\alpha|^2\chi_c[\omega]\chi_m[\omega]}$ denotes the cavity susceptibility that is modified due to the optomechanical interaction. In the fitting procedure, we subtract the constant offset, so the factor $1/2$ in Eq. (S17) disappears. Our final fit has the form $S_{fit} = S_c\times(S_{out}[\omega]-1/2)$, and requires knowing $\kappa_e, \kappa_i, \gamma_m, g_0, \alpha, n_{cav}$, and n_{th} to extract our fit paramater, scale S_c. In favor of knowing α directly, we can use $g_0^2|\alpha|^2 = \frac{\kappa\eta P}{4}$ using the parameter η defined in Eq. (S15).

The fit procedure is as follows: We assume that at sufficiently low red-detuned drive power, the mechanical occupation is unperturbed by the drive. For the points at the lowest powers shown in Fig. S15**A**, below −32 dB, n_m is known from the reference temperature obtained from the thermalization step. Then we use the power-dependence parameter η obtained from the effective linewidth step, and fit the data at all powers to obtain n_m and n_c at each power. The effective linewidth is shown in Fig. S15**A**, with intrinsic mechanical linewidth $\gamma_m = 168.9 \pm 9.5$ Hz and power factor $\eta = 5.37\cdot 10^4$ Hz mW^{-1} completing the fit.

With our initial guess of the occupation numbers, we subsequently refine the fits of our scale parameter and η (now using the whole dataset). Using the updated values, we re-fit n_m and n_c at all powers, and the final result is shown in Fig. S15**B**. In the plots, we have used the final $\eta = 5.37\cdot 10^4$ Hz mW^{-1}, and scale $S_c = 2.04\cdot 10^{-15}\,\frac{\mathrm{W}/\sqrt{\mathrm{Hz}}}{n_c}$.

E. Data filtering

Due to limitations of our vector network analyzer, we drive our system at a series of discrete frequencies instead of a continuous sweep. This way, we can control the step size and direction, which allows us to do a bidirectional measurement where the drive frequency first increases and then decreases. We record the response of our system on a separate spectrum analyzer (SA), which integrates for the full duration of the increasing/decreasing segments separately. The response measured at the second red sideband ($\omega_c - 2\omega_m$) during the upwards frequency sweep is shown in Fig. S16**A**.

Our SA records the spectrum using a much finer set of points than the frequencies at which the vector network analyzer outputs its drive. This condition creates a periodic pattern of peaks in the SA-recorded spectrum, which obscures the true shape of the curve. We are only interested in the tops of the peaks, since there is no sideband drive at the frequencies between the peaks. We filter the SA points in a small bandwidth around each of the vector network analyzer output frequencies, and integrate the power over that bandwidth. The filtered signal is a much shorter set of points that traces out the tops of the peaks. We have plotted the unfiltered data and the filtered signals as blue dots and black squares respectivel in Fig. S16**A**.

F. Exclusion of other sources of nonlinearity

1. *Electrostatic nonlinearity: Average potential offset*

The top and bottom plates of our drum form a capacitance separated by a vacuum gap at equilibrium of $d' \simeq 15$ nm. Any static average potential difference between the plates exerts an attractive force between the plates, which has been used in a similar system to tune the vacuum gap[30]. In our system, the top and bottom plates are connected galvanically through the

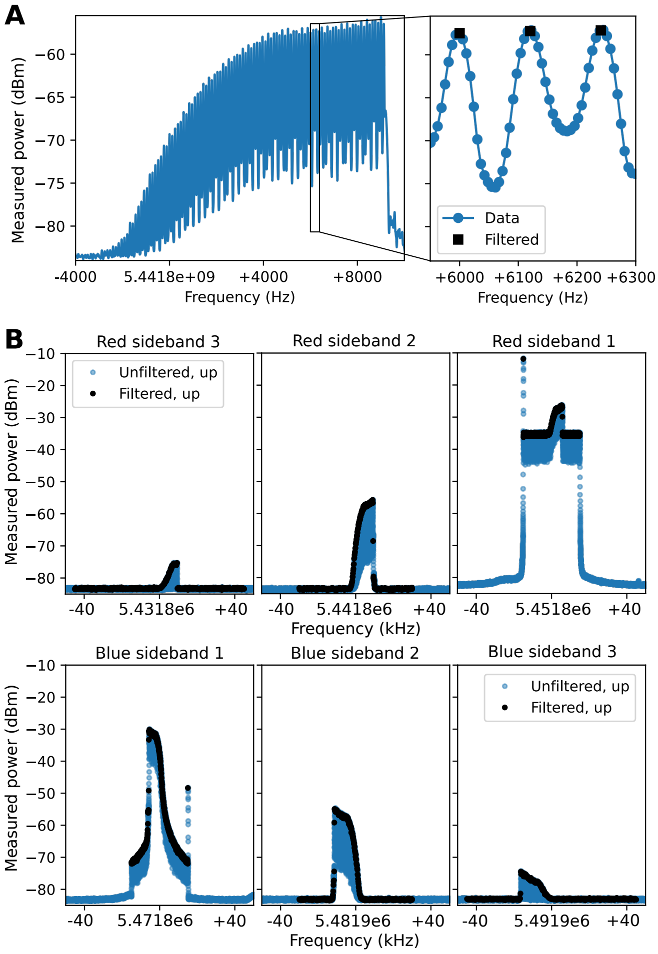

Fig. S16 | Data filtering. **A**: The measured power on the spectrum analyzer shows periodic peaks at the sideband drive frequency steps. We filter out the peaks located at these frequencies (black squares). **B**: All sidebands as recorded on the spectrum analyzer (blue) and filtered (black). Clearly visible is the noise pedestal due to the drive at the first red sideband. The sharp peak at the edge of the pedestal is from the vector network analyzer start/stop frequency.

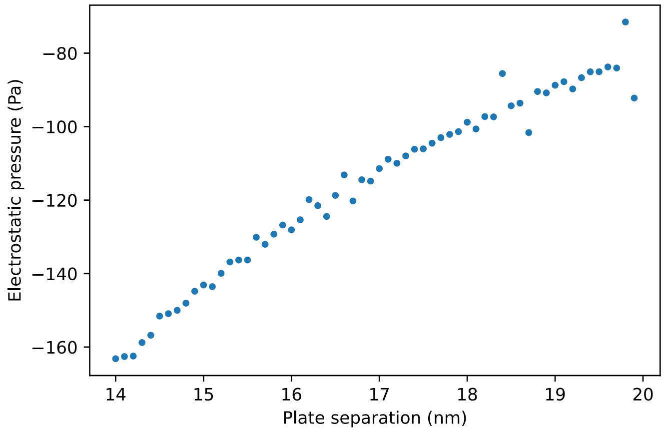

Fig. S17 | Electrostatic effects. Electrostatic pressure due to a 1 V static potential offset between the drum plates, as a function of their separation distance d. Due to the small energies involved and the geometry of the simulation, it is sensitive to mesh-related inaccuracies.

superconducting cavity, thus they are two sides of the same superconductor. In the absence of a large thermal gradient across our device, we expect the average potential difference between the plates to be negligibly small. Nonetheless, if there were a 1 V static average potential difference, this would correspond to a pressure of $P_{\mathrm{elec}} \simeq 150$ Pa for $d' = 15$ nm (based on a COMSOL simulation, as shown in Fig. S17). This pressure is negligible compared to the Casimir pressure, which at this distance is $P_{\mathrm{c}} = 12.0 \pm 0.6$ kPa.

Our experiment is not directly sensitive to the absolute value of the (Casimir) pressure, and neither is it directly sensitive to any absolute pressure from the electrostatic force. It is sensitive to the *nonlinearity* that originates from these effects: The electrostatic force contributes a softening nonlinearity that scales with $P_{\mathrm{elec}} \propto d^{-2}$. This scaling is much weaker than the Casimir force scaling, $P_{\mathrm{c}} \propto d^{-3.2}$. Since the magnitude of the electrostatic force is much less and the nonlinearity scales much weaker than the Casimir force, the effect from the average potential difference is negligible.

2. *Electrostatic nonlinearity: Potential patches*

It is well known that crystal grain orientations can cause local differences in the electrostatic potential[63], also known as potential patches[64]. This means that although two closely spaced conductors may have the same *average* potential, there may still be a non-zero attractive electrostatic force between the conductors. Numerical simulations of randomized patch geometries can be used to estimate the force contributed by these potential patches[50,64,65]. Such numerical simulations rely on accurate information about the (lateral) sizes of these patches, as well as their voltage distribution[66,67].

We experimentally measure the patches in our aluminium to have a characteristic size of $\ell = 158$ nm and a potential intensity that falls well within a normal distribution width $\sigma = 100$ mV. With these numbers, we overestimate the pressure exerted by potential patches by about a factor 10. Nonetheless, we find that the patch pressure is several orders of magnitude smaller than the Casimir pressure at our equilibrium position $d' = 15.1$ nm, as shown in Fig. S18. We exclude that potential patches are responsible for the nonlinearity that we observe in our mechanical resonator. We describe the experimental details in the next paragraphs.

KPFM measurement of patches

We use Kelvin Probe Force Microscopy (KPFM) to locally measure the potential on our sample, which is a well-established technique based on a conductive atomic force microscope cantilever[68,69]. We use a sample that was fabricated in the same batch as the sample reported in the main paper. The KPFM measurement results are plotted in Fig. S19, where we see characteristic aluminium spots where the potential is $\simeq 100$–200 mV below the mean. This corresponds to the work function difference between the different crystalline orientations of aluminium: The work function of aluminium in the

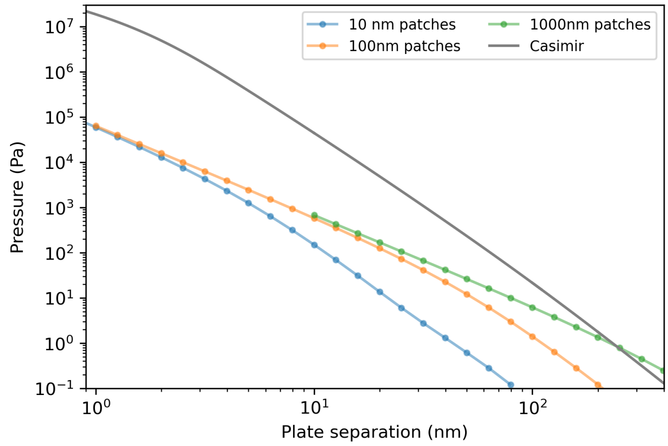

Fig. S18 | Patch pressure. Calculated Casimir pressure and patch potential pressure for patches normally distributed with a standard deviation of 100 mV, for various patch sizes.

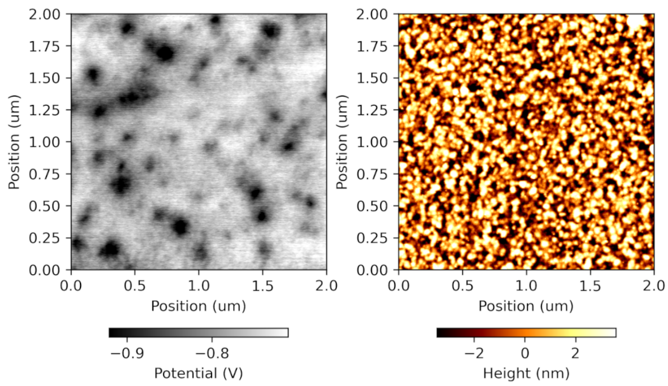

Fig. S19 | Potential patches. Measured surface potential (left) and height (right) of a 2×2 μm^2 aluminium film from the same fabrication batch as the sample studied in the main text.

⟨100⟩-direction is 4.20 eV, in the ⟨110⟩-direction it is 4.06 eV and in the ⟨111⟩-direction it is 4.26 eV[70]. There is no correlation between the potential and height, which are measured simultaneously.

Patch intensity

We expect a Gaussian distribution of the potentials, since the crystalline orientations should be random. But when we bin the measurement points of the potential, the Gaussian fit shown in Fig. S20 is not a good fit. There is a distinct tail towards lower potentials, which represents the spots seen in Fig. S19. The Gaussian fit is centered around a mean value −768 mV with a standard deviation σ of 30.4 mV. The mean potential seen in Fig. S19 is due to the insulating substrate due to which the sampled area is not well galvanically connected to ground: Our KPFM tip touches down before the measurement and this transfers some charge to the sample. Any excess charge leaks out over time (timescale of approximately 30 minutes in air), so our measurement shows some offset potential.

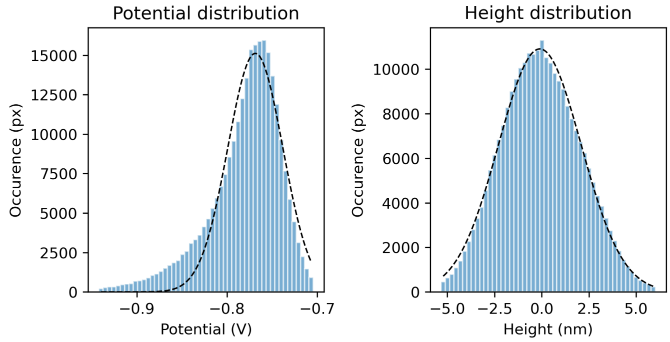

Fig. S20 | Potential patch statistics. Distribution of the measured potentials and heights for the area shown in Fig. S19, and Gaussian fits (dashed black lines).

Patch size

Besides the intensities of the potential patches, their spatial extent (average patch feature size ℓ) strongly affects the distance scaling of the electrostatic force they exert[50,65]. Recent simulations show that the lateral resolution of the KPFM probe can lead to an overestimation of the patch size and an underestimation of the patch intensity[71]. We use ASYELEC02 probes in our AFM, which have a nominal tip radius of 25 nm, and operate in tapping mode with an amplitude 10 nm. With these numbers, we can estimate the lateral resolution of our KPFM measurement using[72] $\ell_{\mathrm{min}} = \sqrt{RH} \simeq$ 16 nm where R is the tip radius and H is the minimal tip-sample distance. We determine the average size of the experimentally measured patches using the `correlate2d` function from Scipy, which is plotted in Fig. S21. We find the average patch size ℓ_{p} is 158 nm, which is well above our minimal lateral resolution, $\ell_{\mathrm{p}} \gg \ell_{\mathrm{min}}$. Thus there is no reason to assume we significantly overestimate the characteristic patch size ℓ or underestimate the patch intensity distribution width σ. Our KPFM measurement also measures the height variation in our sample. The height is well-described by a Gaussian fit centered around −0.1 nm with a σ_{h} of 2.19 nm and a characteristic feature size ℓ_{height} = 32 nm, as shown in Fig. S20.

Patch textures reproducibility

Our patch characterization was performed on a sample that was processed identically (i.e., in the same batch) as the sample in which we measured the Casimir force. We have measured the patch statistics on 8 separate areas on the aluminium parts of the sample, and obtained similar patch intensities and patch sizes. The average patch intensity distribution width from all 8 areas σ_{mean} = 36 mV, and the average patch size is ℓ_{mean} = 160 nm, with both parameters varying minimally between different measurement areas.

While some processing steps greatly affect the size and intensity of potential patches[73], we have performed KPFM measurements on multiple samples (from different batches) and found our processing does not significantly affect the potential patches. The patch intensity does not appear affected by our release etch step, as we have measured σ_{mean} = 41 mV before release (σ_{mean} = 36 mV after). The heat treatment step has the largest effect on the patch intensity, σ_{mean} = 63 mV before

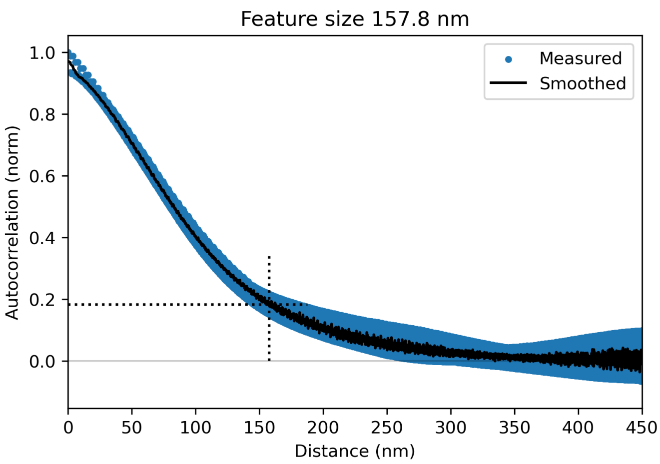

Fig. S21 | Potential patch size. Autocorrelation of the potential shown in Fig. S19. The average patch size ℓ_p is the distance at which the normalized autocorrelation drops to $1/2e \simeq 0.184$ (dotted lines), which is 157.8 nm for our aluminium film.

any heat treatment, $\sigma_{\mathrm{mean}} = 55$ mV after 15 minutes of 200 °C, $\sigma_{\mathrm{mean}} = 47$ mV after 15 minutes of 240 °C, $\sigma_{\mathrm{mean}} = 42$ mV after 15 minutes of 260 °C, and $\sigma_{\mathrm{mean}} = 41$ mV after 15 minutes of 280 °C. These findings appear consistent with potential patches that originate solely from the crystalline structure of the material. Our patch measurements were performed on a sample that has been processed simultaneously and identically to the experimentally reported sample, so we consider them to be representative of the patches present in the drum we tested.

Estimate of patch forces

We calculate the effect of patches for our drum geometry using the simulation framework we developed in an earlier work[50]. We generate Voronoi patterns based on randomized patches of various sizes, with normally distributed potentials with a $\sigma = 100$ mV. Our patterns consist of 400 patches, and we compute the electrostatic energy. From the variation of energy with plate separation, we extract the pressure from the patch potentials for various plate separations as shown in Fig. S18. We find the well-known limit behaviors with the patch size[64]: When $\ell \gg d$, $P_{\mathrm{patch}} \propto d^{-2}$, while when $\ell \ll d$, $P_{\mathrm{patch}} \propto d^{-4}$. The regime where $\ell \gg d$ leads to the greatest patch pressure in absolute sense, yet this is still several orders of magnitude smaller than the Casimir pressure for our plate separation $d =$ 15 nm. We find $P_{\mathrm{patch}} = 230$ Pa at a vacuum gap of 15 nm, much smaller than the Casimir pressure $P_c = 12000 \pm 600$ Pa, as shown in Fig. S18. We note that in Casimir experiments at larger distances ($d \gtrsim 200$ nm), the Casimir pressure can be comparable in amplitude to the patch pressure.

3. *Mechanical nonlinearity: Geometric origin*

There is a significant body of literature on the mechanical nonlinearities with a purely geometric origin. In our experimental platform of superconducting Aluminium drum resonators, Ref.[74] provides an excellent theoretical background that is experimentally tested in Ref.[75]. The nonlinearity due to geometry is a *hardening* nonlinearity in these drum resonators, both on theoretical grounds and experimental evidence[74,75]. The Casimir force contributes a *softening* nonlinearity, which is exactly what is described in the main text, and thus we exclude the geometric nonlinearity on qualitative grounds.

Furthermore, we can exclude the geometric mechanical nonlinearity on quantitative grounds. We follow the method of Ref.[74], which is based on Kirchoff-Love theory for circular membranes. The first assumption in this method is that the resonator is essentially a 2D circular membrane with coordinates (r, θ), which has modes purely moving in the out-of-plane z direction. From COMSOL simulations, we verify that the mode shown in Fig. **8B** consists for $> 99\%$ of motion in the z-direction. Thus we separate the variables of the function $f_{n,m}$ describing the motion of our structure for the (n, m) mode,

$$f_{n,m}(r, \theta, t) = z_{n,m}(t)\psi_{n,m}(r, \theta). \tag{S18}$$

The part $z_{n,m}(t)$ describes the oscillating motion, and $\psi_{n,m}(r, \theta)$ is the normalized mode shape. The mass and stiffness parameters of the fundamental mode (which is the one we study) are given as[74]

$$\begin{aligned}
\mathcal{M}_{0,0} &= \rho h \int_0^{2\pi} \int_0^{R_d} (\psi_{0,0}(r,\theta))^2 \, r dr d\theta, \\
\mathcal{K}_{0,0} &= \frac{1}{12} \frac{Eh^3}{1-\nu_r^2} \int_0^{2\pi} \int_0^{R_d} \left(\psi_{0,0}(r,\theta)\Delta^2\psi_{0,0}(r,\theta)\right) r dr d\theta \\
&\quad + h\sigma_0 \int_0^{2\pi} \int_0^{R_d} (\psi_{0,0}(r,\theta)\Delta\psi_{0,0}(r,\theta)) \, r dr d\theta.
\end{aligned} \tag{S19}$$

We denote the material parameters: ρ is the density of the drum material, E is the Young's modulus, ν_r the Poisson's ratio, and σ_0 the stress (negative for tensile stress). The drum geometry is taken into account via the drum radius R_d and thickness h. Finally,

$$\Delta \ldots = \frac{1}{r}\frac{\partial \ldots}{\partial r}\left(r \frac{\partial \ldots}{\partial r}\right) + \frac{1}{r^2}\frac{\partial^2 \ldots}{\partial \theta^2} \tag{S20}$$

is the Laplacian operator in polar coordinates. From Eq. (S19), we can calculate the mode frequency $\omega_{0,0} = \sqrt{\mathcal{K}_{0,0}/\mathcal{M}_{0,0}}$.

In the COMSOL model shown in Fig. **8**, we use material parameters $\rho = 2700$ kg m^{-3}, $E = 76.6$ GPa, $\nu_r = 0.32$, and the average value of the von Mises stress over the drum domain, $\sigma_0 = -270$ MPa (following the convention of Ref.[74], tensile stress is negative in the analytical description, while in the COMSOL plots tensile stress is positive). Combined with the drum diameter $2R_d = 11.3$ µm and the thickness of the evaporated Al $h = 120$ nm, we can evaluate Eq. (S19). We find $\mathcal{M}_{0,0} = 1.38 \times 10^{-13}$ kg m^2 and $\mathcal{K}_{0,0} = 1467$ N m. The resulting frequency $\omega_{0,0} = 2\pi \times 16.4$ MHz is close to our bare resonator frequency $\omega_r = 2\pi \times 16.3$ MHz.

The geometric nonlinearity can be captured in a cubic term ($\propto x^3$), and its coefficient for the fundamental mode can be found from the expression[74]

$$\tilde{\mathcal{K}}_{0,0} = -\frac{Eh}{R_d^2}\frac{C_{0,0}^{(1)}}{1-\nu_r}\int_0^{2\pi}\int_0^{R_d}\left(\psi_{0,0}(r,\theta)\Delta\psi_{0,0}(r,\theta)\right) r dr d\theta \tag{S21}$$

where $C_{0,0}^{(1)} = 0.389664$ as tabulated in Table IV of Ref.[74]. From our COMSOL simulations, we obtain $\tilde{\mathcal{K}}_{0,0} = 3.55 \times 10^{15}$ N m^{-1}. We then relate this to the coefficient α_D of the Duffing term,

$$\ddot{x} + \gamma_r\dot{x} + \omega_r x + \alpha_D x^3 = \frac{F_d}{m_{\mathrm{eff}}}, \tag{S22}$$

where $\alpha_D = \tilde{\mathcal{K}}_{0,0}/\mathcal{M}_{0,0} = +2.57 \times 10^{28}$ m^{-2} s^{-2}. This value is close to the experimental fit of Refs.[74,75], which is $\alpha_D = +7\times10^{27}$ m^{-2} s^{-2} in a drum resonator that is of nearly identical design to the one in this work.

From the coefficient α_D, we can estimate that a +1 Hz frequency shift should occur if the motional amplitude is $x \simeq 0.6$ nm. At those amplitudes, we see a multiple-kHz *negative* frequency shift corresponding to the Casimir force. Thus we can exclude the geometrical mechanical nonlinearity based on the magnitude and sign of the frequency shift.

4. *Higher-order optomechanical couplings*

The optomechanical cavity is formed by a plate capacitor where one of the plates is mechanically compliant. The capacitance is not a linear function of the separation distance d', and g_0 only represents the first-order Taylor series of the capacitance in x/d'. To estimate the 'higher order' optomechanical couplings that stem from the nonlinearity of the capacitance expansion, we follow the method of[75] derived for the same type of system. The cavity frequency and couplings up to third order in x are

$$\begin{aligned}
\omega_c(x) &= \omega_c(0) - \left[g_0\frac{x}{x_{\mathrm{zpf}}} + \frac{g_1}{2}\left(\frac{x}{x_{\mathrm{zpf}}}\right)^2 + \frac{g_2}{2}\left(\frac{x}{x_{\mathrm{zpf}}}\right)^3\right] \\
g_1 &= g_0\left[2\frac{x_{\mathrm{zpf}}}{d'} - 3\frac{g_0}{\omega_c(0)}\right] \\
g_2 &= g_0\left[2\left(\frac{x_{\mathrm{zpf}}}{d'}\right)^2 - 6\frac{x_{\mathrm{zpf}}}{d'}\frac{g_0}{\omega_c(0)} + 5\left(\frac{g_0}{\omega_c(0)}\right)^2\right]
\end{aligned} \tag{S23}$$

For a motion amplitude of $x = 0.2$ nm, close to the maximum amplitude observed here, the frequency shift from the g_0 term is $\Delta\omega_c \simeq -6.5$ MHz, the additional shift from g_1 would be $\Delta\omega_c = -7.5 \times 10^{-2}$ MHz and the additional shift from g_2 would be $\Delta\omega_c = -8.7 \times 10^{-4}$ MHz. These higher-order contributions are only a relevant contribution to the frequency shift for extremely large displacements ($\simeq$ nm). At these displacements, the frequency shift is much larger than the cavity linewidth, $\Delta\omega_c \gg \kappa$, so the drive efficiency that we describe in the main text is the most important optomechanical effect to take into account. We emphasize that the nonlinearity from the plate capacitor expansion only affects the *cavity* frequency shift and not the mechanical frequency shift from the Casimir force.

G. Measurements on a second device

We have repeated the experiments of the main text in a second device, fabricated using an identical design but in a different fabrication run. The parameters of the device were characterized using the same method as for the device in the main text, and they are reported in Table 2.

Quantity	Symbol	Value
Unperturbed frequency	ω_r	$2\pi \times 16.710$ MHz
Mechanical frequency	ω_m	$2\pi \times 13.688$ MHz
Mechanical linewidth	$\gamma_r \simeq \gamma_m$	$2\pi \times 231 \pm 4$ Hz
Cavity frequency	ω_c	$2\pi \times 7.589718$ GHz
External linewidth	κ_e	$2\pi \times 304.7 \pm 2.8$ kHz
Internal linewidth	κ_i	$2\pi \times 608.7 \pm 6.2$ kHz
Optomechanical coupling	g_0	$2\pi \times 67 \pm 3$ Hz
Effective mass	m_{eff}	3.96×10^{-14} kg
Rest separation without Cas. f.	d	19.1 ± 0.5 nm
Rest separation	d'	17.3 ± 0.5 nm
Bottom plate diameter	$2r$	11.3 µm
Casimir amplitude	P	$(1275 \pm 7) \cdot 10^{-24}$ Pa m^n
Casimir force scaling exponent	n	3.193

Table 2 | Parameters of the second device.

In the absence of the Casimir force, the devices have a similar mechanical resonance frequency. However, this second device has a slightly different separation of the plates at mechanical zero (d), the final mechanical frequency is rather different due to the nonlinear nature of the Casimir force. Due to the lower optomechanical coupling rate, and higher cavity linewidth, it requires more drive power to reach larger displacement amplitudes, and we are limited by the maximum power that our measurement chain can handle. These measurements were performed in a different dilution refrigerator to the experiments in the main text, with a separate set of measurement equipment.

One of the mechanical response curves of the second device is shown in Fig. S22. We have performed the same calibration procedure as in the device of the main text, and extract $d = 19.1 \pm 0.5$ nm (solid black line) from a fit to the data. For completeness, we also show the theory curves for $d = 19.6$ nm (dotted black line) and $d = 18.6$ nm (dashed black line).

[1] H. B. G. Casimir, On the attraction between two perfectly conducting plates, Proc. Kon. Ned. Akad. v. Wet. **51**, 793 (1948).

[2] E. M. Lifshitz, The theory of molecular attractive forces between solids, Journal of Experimental and Theoretical Physics

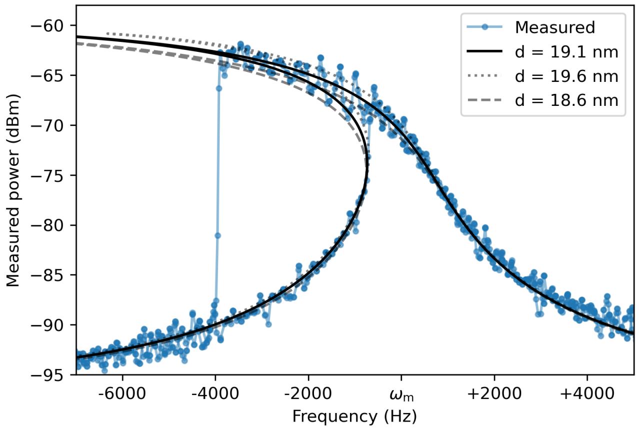

Fig. S22 | Measurement of the nonlinearity in a second device. The measured response (blue) for 10 dBm cavity drive power and 0 dBm red sideband drive power. The theory curves based on the Casimir force for a separation of mechanical zero of d = 19.1 nm (solid black line), d = 19.6 nm (dotted black line) and d = 18.6 nm (dashed black line) are overlaid on the measured data. The d = 19.1 nm curve is closest to the center of the measured data.

2, 73 (1956).

[3] S. K. Lamoreaux, Demonstration of the Casimir force in the 0.6 to 6 μm range, Physical Review Letters **78**, 5 (1997).

[4] U. Mohideen and A. Roy, Precision measurement of the Casimir force from 0.1 to 0.9 μm, Physical Review Letters **81**, 4549 (1998).

[5] A. W. Rodriguez, F. Capasso, and S. G. Johnson, The Casimir effect in microstructured geometries, Nature Photonics **5**, 211 (2011).

[6] L. M. Woods, D. A. R. Dalvit, A. Tkatchenko, P. Rodriguez-Lopez, A. W. Rodriguez, and R. Podgornik, Materials perspective on Casimir and van der Waals interactions, Reviews of Modern Physics **88**, 045003 (2016).

[7] T. Gong, M. R. Corrado, A. R. Mahbub, C. Shelden, and J. N. Munday, Recent progress in engineering the Casimir effect - applications to nanophotonics, nanomechanics and chemistry, Nanophotonics **10**, 523 (2021).

[8] F. M. Serry, D. Walliser, and G. J. Maclay, The role of the Casimir effect in the static deflection and stiction of membrane strips in microelectromechanical systems (MEMS), Journal of Applied Physics **84**, 2501 (1998).

[9] H. B. Chan, V. A. Aksyuk, R. N. Kleiman, D. J. Bishop, and F. Capasso, Nonlinear micromechanical Casimir oscillator, Physical Review Letters **87**, 211801 (2001).

[10] W. Broer, G. Palasantzas, J. Knoester, and V. B. Svetovoy, Significance of the Casimir force and surface roughness for actuation dynamics of MEMS, Physical Review B **87**, 125413 (2013).

[11] L. Tang, M. Wang, C. Y. Ng, M. Nikolic, C. T. Chan, A. W. Rodriguez, and H. B. Chan, Measurement of non-monotonic Casimir forces between silicon nanostructures, Nature Photonics **11**, 97 (2017).

[12] A. Stange, M. Imboden, J. Javor, L. K. Barrett, and D. J. Bishop, Building a Casimir metrology platform with a commercial MEMS sensor, Microsystems and Nanoengineering **5**, 14 (2019).

[13] J. M. Pate, M. Goryachev, R. Y. Chiao, J. E. Sharping, and M. E. Tobar, Casimir spring and dilution in macroscopic cavity optomechanics, Nature Physics **16**, 1117 (2020).

[14] K. Y. Fong, H.-K. Li, R. Zhao, S. Yang, Y. Wang, and X. Zhang, Phonon heat transfer across a vacuum through quantum fluctuations, Nature **576**, 243 (2019).

[15] Z. Xu, X. Gao, J. Bang, Z. Jacob, and T. Li, Non-reciprocal energy transfer through the Casimir effect, Nature Nanotechnology **17**, 148 (2022).

[16] V. B. Bezerra, G. L. Klimchitskaya, V. M. Mostepanenko, and C. Romero, Violation of the Nernst heat theorem in the theory of the thermal Casimir force between Drude metals, Physical Review A **69**, 022119 (2004).

[17] J. S. Høye, I. Brevik, S. A. Ellingsen, and J. B. Aarseth, Analytical and numerical verification of the Nernst theorem for metals, Physical Review E **75**, 051127 (2007).

[18] A. O. Sushkov, W. J. Kim, D. A. R. Dalvit, and S. K. Lamoreaux, Observation of the thermal Casimir force, Nature Physics **7**, 230 (2011).

[19] V. M. Mostepanenko, Casimir puzzle and Casimir conundrum: Discovery and search for resolution, Universe **7**, 84 (2021).

[20] R. S. Decca, E. Fischbach, G. L. Klimchitskaya, D. E. Krause, D. López, and V. M. Mostepanenko, Improved tests of extra-dimensional physics and thermal quantum field theory from new Casimir force measurements, Physical Review D **68**, 116003 (2003).

[21] G. L. Klimchitskaya, U. Mohideen, and V. M. Mostepanenko, Constraints on non-Newtonian gravity and light elementary particles from measurements of the Casimir force by means of a dynamic atomic force microscope, Physical Review D **86**, 065025 (2012).

[22] U. Leonhardt, Liftshitz theory of the cosmological constant, Annals of Physics **411**, 167973 (2019).

[23] G. Bimonte, E. Calloni, G. Esposito, and L. Rosa, Variations of Casimir energy from a superconducting transition, Nuclear Physics B **726**, 441 (2005).

[24] D. Pérez-Morelo, A. Stange, R. W. Lally, L. K. Barrett, M. Imboden, A. Som, D. K. Campbell, V. A. Aksyuk, and D. J. Bishop, A system for probing Casimir energy corrections to the condensation energy, Microsystems and Nanoengineering **6**, 115 (2020).

[25] G. Bimonte, H. Haakh, C. Henkel, and F. Intravala, Optical BCS conductivity at imaginary frequencies and dispersion energies of superconductors, Journal of Physics A: Mathematical and Theoretical **43**, 145304 (2010).

[26] R. A. Norte, M. Forsch, A. Wallucks, I. Marinković, and S. Gröblacher, Platform for measurements of the Casimir force between two superconductors, Physical Review Letters **121**, 030405 (2018).

[27] J. R. Rodrigues, A. Gusso, F. S. S. Rosa, and V. R. Almeida, Rigorous analysis of Casimir and van der Waals forces on a silicon nano-optomechanical device actuated by optical forces, Nanoscale **10**, 3945 (2018).

[28] G. Bimonte, Casimir effect between superconductors, Physical Review A **99**, 052507 (2019).

[29] R. S. Decca, D. López, E. Fischbach, G. L. Klimchitskaya, D. E. Krause, and V. M. Mostepanenko, Tests of new physics from precise measurements of the Casimir pressure between two gold-coated plates, Physical Review D **75**, 077101 (2007).

[30] R. W. Andrews, A. P. Reed, K. Cicak, J. D. Teufel, and K. W. Lehnert, Quantum-enabled temporal and spectral mode conversion of microwave signals, Nature Communications **6**, 10021 (2015).

[31] F. M. Serry, D. Walliser, and G. J. Maclay, The anharmonic Casimir oscillator (ACO) - The Casimir effect in a model microelectromechanical system, Journal of Microelectromechani-

cal Systems **4**, 193 (1995).

[32] H. B. Chan, V. A. Aksyuk, R. N. Kleiman, D. J. Bishop, and F. Capasso, Quantum mechanical actuation of microelectromechanical systems by the Casimir force, Science **291**, 1941 (2001).

[33] J. D. Teufel, T. Donner, D. Li, J. W. Harlow, M. S. Allman, K. Cicak, A. J. Sirois, J. D. Whittaker, K. W. Lehnert, and R. W. Simmonds, Sideband cooling of micromechanical motion to the quantum ground state, Nature **475**, 359 (2011).

[34] E. E. Wollmann, C. U. Lei, A. J. Weinstein, J. Suh, A. Kronwald, F. Marquardt, A. A. Clerk, and K. C. Schwab, Quantum squeezing of motion in a mechanical resonator, Science **349**, 952 (2015).

[35] J.-M. Pirkkalainen, E. Damskägg, M. Brandt, F. Massel, and M. A. Sillanpää, Squeezing of quantum noise of motion in a micromechanical resonator, Physical Review Letters **115**, 243601 (2015).

[36] F. Lecocq, J. B. Clark, R. W. Simmonds, J. Aumentado, and J. D. Teufel, Quantum nondemolition measurement of a nonclassical state of a massive object, Physical Review X **5**, 041037 (2015).

[37] C. F. Ockeloen-Korppi, E. Damskägg, J.-M. Pirkkalainen, M. Asjad, A. A. Clerk, F. Massel, M. J. Woolley, and M. A. Sillanpää, Stabilized entanglement of massive mechanical oscillators, Nature **556**, 478 (2018).

[38] S. Kotler, G. A. Peterson, E. Shojaee, F. Lecocq, K. Cicak, A. Kwiatkowski, S. Geller, S. Glancy, E. Knill, R. W. Simmonds, J. Aumentado, and J. D. Teufel, Direct observation of deterministic macroscopic entanglement, Science **372**, 622 (2021).

[39] L. Mercier de Lépinay, C. F. Ockeloen-Korppi, M. J. Woolley, and M. A. Sillanpää, Quantummechanics-free subsystem with mechanical oscillators, Science **372**, 625 (2021).

[40] R. Riedinger, S. Hong, R. A. Norte, J. A. Slater, J. Shang, A. G. Krause, V. Anant, M. Aspelmeyer, and S. Gröblacher, Non-classical correlations between single photons and phonons from a mechanical oscillator, Nature **530**, 313 (2016).

[41] I. Galinskiy, G. Enzian, M. Parniak, and E. S. Polzik, Nonclassical correlations between photons and phonons of center-of-mass motion of a mechanical oscillator, Physical Review Letters **133**, 173605 (2024).

[42] A. D. O'Connell, M. Hofheinz, M. Ansmann, R. C. Bialczak, M. Lenander, E. Lucero, M. Neeley, D. Sank, H. Wang, M. Weides, J. Wenner, J. M. Martinis, and A. N. Cleland, Quantum ground state and single-phonon control of a mechanical resonator, Nature **464**, 697 (2010).

[43] Y. Chu, P. Kharel, T. Yoon, L. Frunzio, P. T. Rakich, and R. J. Schoelkopf, Creation and control of multi-phonon Fock states in a bulk acoustic-wave resonator, Nature **563**, 666 (2018).

[44] S. Marti, U. von Lüpke, O. Joshi, Y. Yang, M. Bild, A. Omahen, Y. Chu, and M. Fadel, Quantum squeezing in a nonlinear mechanical oscillator, Nature Physics **20**, 1448 (2024).

[45] Y. Yang, I. Kladarić, M. Drimmer, U. von Lüpke, D. Lenterman, J. Bus, S. Marti, M. Fadel, and Y. Chu, A mechanical qubit, Science **386**, 783 (2024).

[46] C. Samanta, S. L. De Bonis, C. B. Møller, R. Tormo-Queralt, W. Yang, C. Urgell, B. Stamenic, B. Thibeault, Y. Jin, D. A. Czaplewski, F. Pistolesi, and A. Bachtold, Nonlinear nanomechanical resonators approaching the quantum ground state, Nature Physics **19**, 1340 (2023).

[47] H. J. Eerkens, *Investigations of radiation pressure: Optical side-band cooling of a trampoline resonator and the effect of superconductivity on the Casimir force*, phdthesis, Universiteit Leiden (2017), iSBN: 9789085933243, https://hdl.handle.net/1887/59506.

[48] M. Aspelmeyer, T. J. Kippenberg, and F. Marquardt, Cavity optomechanics, Reviews of Modern Physics **86**, 1391 (2014).

[49] T. J. Kippenberg and K. J. Vahala, Cavity opto-mechanics, Optics Express **15**, 17172 (2007).

[50] M. H. J. de Jong and L. Mercier de Lépinay, Simulating the electrostatic patch force in sphere-plate and plate-plate geometries, https://arxiv.org/abs/2408.16323 (2024), arxiv preprint.

[51] M. A. Sillanpää, R. Khan, T. T. Heikkilä, and P. J. Hakonen, Macroscopic quantum tunneling in nanoelectomechanical systems, Physical Review B **84**, 195433 (2011).

[52] F. Pistolesi, A. N. Cleland, and A. Bachtold, Proposal for nanomechanical qubit, Physical Review X **11**, 031027 (2021).

[53] M. Tinkham, *Introduction to superconductivity* (McGraw-Hill, Inc., 1996).

[54] E. D. Palik, ed., *Handbook of optical constants of solids*, Vol. 1 (Academic, New York, 1997).

[55] T. H. K. Barron, J. F. Collins, T. W. Smith, and G. K. White, Thermal expansion, Grüneisen functions and static lattice properties of quartz, Journal of Physics C: Solid State Physics **15**, 4311 (1982).

[56] M. Pinard, Y. Hadjar, and A. Heidmann, Effective mass in quantum effects of radiation pressure, European Physical Journal D **7**, 107 (1999).

[57] A. Dhooge, W. Govaerts, and Y. A. Kuznetsov, MATCONT: a MATLAB package for numerical bifurcation analysis of ODEs, ACM Transactions on Mathematical Software **29**, 141 (2003).

[58] A. Dhooge, W. Govaerts, Y. A. Kuznetsov, H. G. E. Meijer, and B. Sautois, New features of the software MATCONT for bifurcation analysis of dynamical systems, Mathematical and Computer Modelling of Dynamical Systems **14**, 79 (2008).

[59] M. Xu, R. J. G. Elbertse, A. Keşkekler, G. Bimonte, J. Lee, S. Otte, and R. A. Norte, Measuring Casimir force across a superconducting transition, https://arxiv.org/abs/2504.10579 (2025), arxiv preprint.

[60] G. Palasantzas, P. J. van Zwol, and J. T. M. de Hosson, Transition from casimir to van der waals force betweenmacroscopic bodies, Applied Physics Letters **93**, 121912 (2008).

[61] B. He, Q. Lin, M. Orszag, and M. Xiao, Mechanical oscillations frozen on discrete levels by two optical driving fields, Physical Review A **102**, 011503 (2020).

[62] P. Virtanen, R. Gommers, T. E. Oliphant, M. Haberland, T. Reddy, D. Cournapeau, E. Burovski, P. Peterson, W. Weckesser, J. Bright, S. J. van der Walt, M. Brett, J. Wilson, K. Jarrod Millman, N. Mayorov, A. R. J. Nelson, E. Jones, R. Kern, E. Larson, C. J. Carey, I. Polat, Y. Feng, E. W. Moore, J. VanderPlas, D. Laxalde, J. Perktold, R. Cimrman, I. Henriksen, E. A. Quintero, C. R. Harris, A. M. Archibald, A. H. Ribeiro, F. Pedregosa, P. van Mulbregt, and Scipy 1.0 Contributors, Scipy 1.0: fundamental algorithms for scientific computing in Python, Nature Methods **17**, 261 (2020).

[63] J. B. Camp, T. W. Darling, and R. E. Brown, Macroscopic variations of surface potentials of conductors, Journal of Applied Physics **69**, 7126 (1991).

[64] C. C. Speake and C. Trenkel, Forces between superconducting surfaces due to spatial variations of surface potential, Physical Review Letters **90**, 160403 (2003).

[65] J. Ke, W.-C. Dong, S.-H. Huang, Y.-J. Tan, W.-H. Tan, S.-Q. Yang, C.-G. Shao, and J. Luo, Electrostatic effect due to patch potentials between closely spaced surfaces, Physical Review D **107**, 065009 (2023).

[66] R. O. Behunin, F. Intravaia, D. A. R. Dalvit, P. A. Maia Neto, and S. Reynaud, Modeling electrostatic patch effects in Casimir force measurements, Physical Review A **85**, 012504 (2012).

[67] R. O. Behunin, Y. Zeng, D. A. R. Dalvit, and S. Reynaud, Electrostatic patch effects in Casimir-force experiments performed in sphere-plane geometry, Physical Review A **86**, 052509 (2012).

[68] R. O. Behunin, D. A. R. Dalvit, R. S. Decca, and C. C. Speake, Limits on the accuracy of force sensing at short separations due to patch potentials, Physical Review D **89**, 051301 (2014).

[69] J. L. Garrett, D. Somers, and J. N. Munday, The effect of patch potentials in Casimir force measurements determined by heterodyne Kelvin probe force microscopy, Journal of Physics: Condensed Matter **27**, 214012 (2015).

[70] W. M. Haynes, ed., *CRC Handbook of Chemistry and Physics*, 96th ed. (CRC Press, Roca Baton, 2015).

[71] K. Shi, P. Luo, J. Liu, H. Yin, and Z. Zhou, Dependence of electrostatic patch force evaluation on the lateral resolution of Kelvin probe force microscopy, https://arxiv.org/abs/2411.01733 (2024), arxiv preprint.

[72] G. Lévêque, P. Cadet, and A. Arinero, Sensitivity and resolution in noncontact electrostatic force microscopy in the case of a constant potential, Physical Review B **71**, 205419 (2005).

[73] J. L. Garrett, J. Kim, and J. N. Munday, Measuring the effect of electrostatic patch potentials in Casimir force experiments, Physical Review Research **2**, 023355 (2020).

[74] D. Cattiaux, S. Kumar, X. Zhou, A. Fefferman, and E. Collin, Geometrical nonlinearity of circular plates and membranes: An alternative method, Journal of Applied Physics **128**, 104501 (2020).

[75] D. Cattiaux, X. Zhou, S. Kumar, I. Golokolenov, R. R. Gazizulin, A. Luck, L. Mercier de Lépinay, M. Sillanpää, A. D. Armour, A. Fefferman, and E. Collin, Beyond linear coupling in microwave optomechanics, Physical Review Research **2**, 033480 (2020).

We thank the reviewers and editors for the review process which we think improved the paper.